Dzyaloshinskii-Moriya Interaction and Local Exchange Variation in Rare-Earth Transition-Metal Ferrimagnets

By

Daniel Hiroshi Suzuki

B.S. Materials Science and NanoEngineering
Rice University, 2018

Submitted to the Department of Materials Science and Engineering
in Partial Fulfillment of the Requirements for the Degree of

Doctor of Philosophy in Materials Science and Engineering

at the

Massachusetts Institute of Technology

May 2023

Authored by: Daniel Hiroshi Suzuki

                 Department of Materials Science and Engineering

                 May 1, 2023

Certified by: Geoffrey S.D. Beach

                 Professor, Department of Materials Science and Engineering

                 Co-director, Materials Research Laboratory at MIT

                 Thesis Supervisor

Accepted by: Robert J. Macfarlane

                 Chair, Departmental Committee on Graduate Studies

Dzyaloshinskii-Moriya Interaction and Local Exchange Variation in Rare-Earth Transition-Metal Ferrimagnets

By

Daniel Hiroshi Suzuki

Submitted to the Department of Materials Science and Engineering
in Partial Fulfillment of the Requirements for the Degree of

Doctor of Philosophy in Materials Science and Engineering

Abstract

Spintronics utilizes the spin of electrons in addition to its charge to manipulate magnetism in thin films. Research in spintronics has the potential to usher in a new wave of technologies, particularly in next-generation racetrack memory storage. These technologies rely on the motion of chiral spin textures such as domain walls or skyrmions in order to read and write data. Rare-earth (RE) transition-metal (TM) ferrimagnetic heterostructures are especially promising candidates due to their minimal stray fields and vanishing angular momentum near compensation, and have already exhibited high-speed current-induced domain wall motion and ultra-small skyrmion stability at room temperature.

The stability of the chiral spin textures necessary for racetrack and skyrmionic memory is governed by an antisymmetric magnetic exchange interaction known as the Dzyaloshinskii-Moriya Interaction (DMI). Unlike the symmetric Heisenberg interaction that favors collinear spin alignment and gives rise to ferromagnetism and antiferromagnetism, the DMI favors canting of spins perpendicular to its neighbors. While DMI has been extensively studied in ferromagnetic systems, little work has been done to quantify its strength in ferrimagnetic systems. In this thesis the compositional dependence of a number of static and dynamic magnetic properties of RE-TM amorphous ferrimagnets necessary for the design of chiral spin texture-based technologies is investigated. We develop a simple method for determining magneto-optical Kerr angles that informs efficient design of magneto-optical Kerr effect microscopes. Additionally, we observe a significant variation in both RE and TM average atomic moment as a function of composition well described by a local environment model as well as substantial variation in magnetization as a function of RE-TM film thickness. Finally, current-induced domain wall motion is used to characterize the spin-transport properties and DMI of RE-TM films.

Thesis Supervisor:	Geoffrey S.D. Beach
Title:	Professor, Materials Science and Engineering
	Co-director, Materials Research Laboratory at MIT

Acknowledgements

This thesis would not have been possible without the support of a number of people over the past few years. I would first like to thank my thesis advisor, Prof. Geoff Beach, for guiding me through my Ph.D. I don't think I've ever met a purer scientist than Geoff. His insatiable curiosity and innate optimism helped keep me motivated and positive even in the face of mounting experimental failures (as was the case more often than not).

I would also like to thank David Bono, our resident electronics guru, for always being willing and available to help me build a new setup or repair an old one. Working with you taught me about electronics, machining, and even plumbing.

I was lucky enough to be part of a great research group filled with smart and good people. Thank you to the entire Beach group who made it a joy to go to the office every day. I would like to especially thank Lucas Caretta, who showed me the ropes when I first joined the group, and Mantao Huang, who continued to happily answer my questions even after he left the group.

Finally, I would like to thank my friends and family for supporting me throughout graduate school, from listening to my latest struggle to helping me relax after a tough week. I am especially grateful for my wonderful partner, Dr. Serena Brandler (beat me by a few months), who was with me for the whole ride and kept me grounded throughout.

1 Table of Contents

List of Figures

List of Tables

2 Introduction

As computational power has risen and access to the internet has become ubiquitous, the amount of information processed on a daily basis has risen exponentially. Many of the world's most valuable companies deal in information acquisition and processing, necessitating the need for dense and cheap memory storage technologies. Magnetism provides a natural method for encoding bits of '0' or '1' through the direction of a magnetic moment in an 'up' or 'down' state. Conveniently, these states persist so long as the material is kept below its critical magnetic ordering temperature, making magnetic storage an inherently non-volatile memory technology that can preserves data for decades [1]. Some of the earliest schemes for large-scale memory storage employed magnetic materials at their foundation. To this day, data centers around the world store petabytes of cloud-based information on reels of magnetic tape. In personal computers, hard disk drives (HDDs) utilize magnetic thin films to store bits that mechanically rotates under a head to read or write data. The main limitation of HDDs is random access read time, limited by the rotation speed of the platter, progress in which has stalled since the 1990s [2]. This has led to the dominance of non-magnetic flash technologies in the market today.

The motivation for the work in this thesis was born out of a desire to contribute to the development of next-generation memory storage technologies. In 2008, Parkin proposed a scheme to utilize new spintronic discoveries to create a new form of magnetic storage he called racetrack memory [3], in which magnetic domains encoding information bits in 1D magnetic wires would be moved by electric current instead of by mechanical rotation, eliminating the key limitation of HDDs. Recent breakthroughs in ferrimagnetic materials realized domain wall speeds > 1 km/s, theoretically making racetrack memory technologies competitive with existing RAM technologies

a possibility [4–6]. At the same time, novel exotic spin textures called skyrmions were beginning to be observed at room temperature and manipulated with small current densities [7–12]. Both of these developments relied upon a curious interfacial magnetic exchange interaction known as the Dzyaloshinskii-Moriya interaction (DMI), an interaction extensively studied in ferromagnetic systems, but not in the ferrimagnetic systems exhibiting high-speed domain walls and stable skyrmions.

In this thesis we focus on the determination of DMI in RE-TM thin films. Chapter 3 provides fundamental background knowledge on DMI and chiral spin textures. In Chapter 4, we discuss a few of the most important experimental methods used in thesis, including a discussion on how to maximize signal in wide-field magneto-optical Kerr effect microscopes. In Chapter 5, a novel method for magneto-optical Kerr angle determination is developed and demonstrated in GdCo films. In Chapter 6, we conduct a thorough investigation of the magnetic properties of RE-TM films as a function of composition and thickness. The measurement of domain wall motion in magnetic racetrack devices by magneto-optical Kerr effect microscopy is discussed in Chapter 7. Additionally, the results of the previous Chapter are combined to determine the DMI in GdCo thin films. Finally, Chapter 8 summarizes the work done in this thesis and presents ongoing work for consideration.

3 Background

3.1 Heisenberg Exchange

Magnetic ordering results from the symmetric exchange interaction between spins of adjacent atoms, known as the Heisenberg exchange interaction. This interaction has an energy,

$$E_H = \sum_{i,j} -J_{ij} \boldsymbol{S_i} \cdot \boldsymbol{S_j} \tag{3.1}$$

where $\boldsymbol{S}_{i,j}$ are adjacent spins and J_{ij} is the exchange constant between the spins. The Heisenberg interaction favors collinear alignment of spins that either result in ferromagnetic ($J_{ij} > 0$) or antiferromagnetic ($J_{ij} < 0$) order based on the sign of the exchange constant. When two different types of atoms with distinct atomic moments and spins are antiferromagnetically coupled, ferrimagnetism, a third type of magnetic order emerges.

3.2 Dzyaloshinskii-Moriya Interaction

In the late 1950s, in response to observations of weak ferromagnetism in otherwise purely antiferromagnetic materials with particular crystal structures such as α-Fe_2O_3 and $CoCO_3$, a new type of antisymmetric exchange interaction was proposed, later named the Dzyaloshinskii-Moriya interaction (DMI) [13–15]. This interaction was found to only occur in structures lacking inversion symmetry and to be relatively weak compared to Heisenberg exchange [16] .

In contrast to the Heisenberg interaction, DMI favors adjacent spins oriented perpendicular to each other through the relation:

$$E_{DMI} = \sum_{i,j} -\boldsymbol{D}_{ij} \cdot (\boldsymbol{S}_i \times \boldsymbol{S}_j) \qquad (3.2)$$

Here, $\boldsymbol{D}_{ij}$ is the Dzyaloshinskii vector whose direction depends on the symmetry of the system. The cross product in this interaction energy induces rotations of spins over space. With a strong Heisenberg interaction, the macroscopic effect of DMI is to favor the creation of twisting and swirling magnetic textures thereby introducing chirality into magnetic systems. Although initially DMI was thought to only occur in low symmetry crystals (lacking inversion symmetry), in the 1990s it was predicted to occur near magnetic surfaces and interfaces due to symmetry breaking at interfaces locally analogous to bulk crystals lacking inversion symmetry. [17] At interfaces, the DMI vector is given by $\boldsymbol{D}_{ij} = D_{ij}\boldsymbol{n} \times \boldsymbol{e}_{ij}$, where $\boldsymbol{n}$ is the surface normal unit vector and $\boldsymbol{e}_{ij}$ is a unit vector pointing from atom i to j. Thus, the DMI vector always lies in the plane of the interface with a sign determined by the DMI constant. However, merely breaking inversion symmetry is not sufficient to induce a significant DMI. Unlike the Heisenberg interaction which occurs directly between adjacent spins, DMI is an indirect interaction mediated by a third atom with high spin-orbit coupling.

Spin-orbit coupling refers to the interaction between the spin and orbital angular momentum of an atom. Its Hamiltonian is of the form:

$$\hat{H} = \xi \boldsymbol{L} \cdot \boldsymbol{S} \qquad (3.3)$$

where $\boldsymbol{L}$ is the orbital angular momentum of an atom and ξ is the coupling energy. In the electron's rest-frame, the motion of the positively charged nucleus around the electron induces a magnetic moment that interacts with the electron's inherent spin magnetic moment to favor parallel or anti-parallel alignment of the moments [18,19]. The coupling energy is proportional to Z^4 (Z the atomic number) using the Bohr model [20]. This interaction favors parallel or antiparallel alignment of the spin and orbital angular momentum depending on the orbital in question.

Intuitively, this is evident from the semi-classical picture of a nucleus revolving around an electron. The larger atomic number, and consequently larger charge induces a larger electric current. Classically, the current is directly proportional to the generated magnetic moment and results in larger spin-orbit coupling.

In practice, the spin-orbit strength difference between transition metals is less than Z^4 due to radial nodes in the d-orbitals close to the nucleus where charge is nominally highest and spin-orbit effects should be greatest [19]. In addition to its effects in enabling DMI, spin-orbit coupling can give rise to anisotropy in magnetic materials. Orbital hybridization fixes the orbital moments of atoms relative to certain crystallographic planes and subsequently forces the spin in a collinear direction. This results in magnetic anisotropy and the creation of easy and hard magnetization axes corresponding to low and high energy configurations of the magnetic moment. Spin-orbit coupling has been used to create films displaying perpendicular magnetic anisotropy (PMA), in which the magnetization is normal to the surface, by layering magnetic materials (typically Co) on top of high spin-orbit coupled materials (heavy metals) such as Au, Pt, or Pd. [21] PMA materials are of primary importance in memory applications.

3.3 Domain Walls

Due to the cross product in its Hamiltonian, DMI induces spin textures in crystals lacking inversion symmetry or near interfaces between magnetic materials and non-magnetic heavy metals exhibiting high spin-orbit coupling. However, although not as complex as DMI-induced textures, magnetic materials can naturally have texture through the formation of magnetic domains, regions in of homogenous magnetization within the bulk material. Domains arise naturally in most

magnetic materials (with the exception of soft and small magnets) to reduce the energy associated with stray fields emitted from the surface of the material. Domain walls separate domains and facilitate the rotation of magnetic moments from one domain to another. Within their finite thickness, the magnetization continuously rotates from one direction (for example the $+z$ direction) to the opposite direction ($-z$). There are two types of domain walls describing how this rotation occurs. Bloch domain walls rotate out of plane with respect to the plane formed by the magnetization in adjacent domains. Néel domain walls rotate within the plane defined by its adjacent domain magnetizations. In films with PMA, in which one domain is pointing up out of the plane of the surface (parallel to the surface normal) and the other domain is pointing down (antiparallel to the surface normal), the two types of domain walls can quickly be distinguished by the direction of the magnetic moment at the wall midpoint. In these types of samples, both domain wall types have moments perpendicular to the surface normal. Specifically, Bloch walls have a midpoint moment parallel to the domain wall normal while Néel wall midpoint moments are perpendicular to the domain wall normal.
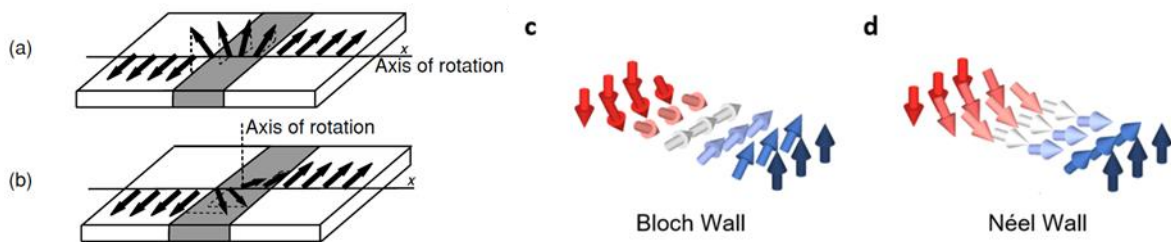
Fig. 3.1: Schematic of (a) a Bloch wall and (b) a Néel wall for sample without PMA. The shaded region is the domain wall [20]. (c,d) Bloch and Néel walls for a sample with PMA.

Domains walls have a finite thickness governed by the energetic competition between Heisenberg exchange, favoring collinear spin alignment of adjacent atoms, and magnetic anisotropy which favors spin alignment along a particular easy axis dependent on the both the crystal structure and geometry magnetic sample in addition to any effects arising from interfacial spin-orbit coupling. This results in a domain wall width $\mathit{\Delta}$ described by the material's anisotropy, K, and exchange stiffness, A [20]

$$\mathit{\Delta} = \sqrt{\frac{A}{K}} \tag{3.4}$$

Domains have historically been used to store information in both magnetic tape in cassettes and in hard disc drives in computers. They have garnered renewed interest recently due to their potential applications in next generation memory coined "racetrack" memory [3]. In racetrack memory, domains are moved (or equivalently domain walls are moved) along a magnetic track in order to read or write data (Fig. 3.2) similar to the scheme used in hard disk drives (HDDs). The key distinction that separates racetrack memory from HDD storage is that in racetrack memory, only the magnetic state is moved along track; no physical motion occurs. Attempts to realize this concept have resulted in current induced domain wall motion. [21–24] This is achieved by interfacing a ferromagnet with a metal layer that exhibits the spin Hall effect such as Pt or Ta. The spin Hall effect (SHE) is the creation of a spin current transverse to an applied charge current. It results in a type of spin-orbit torque that acts on domain walls in response to an applied current, enabling domain wall motion by electric current.
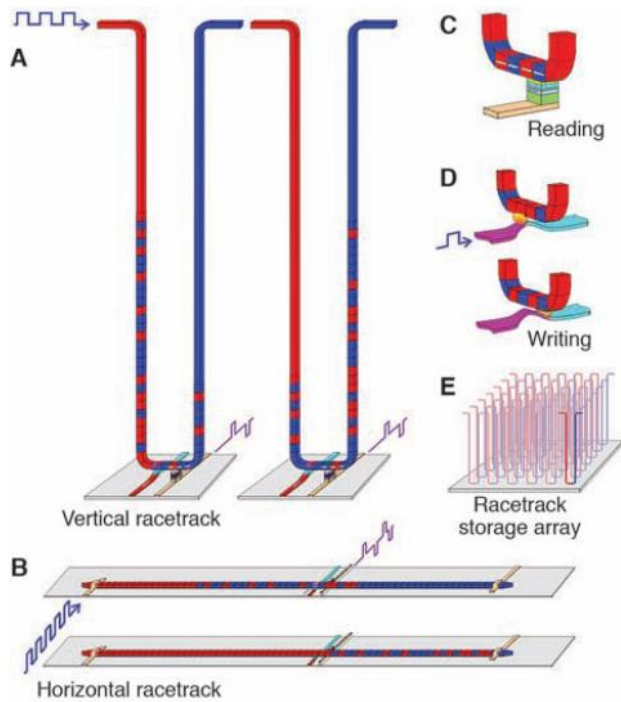
Fig. 3.2: Racetrack memory. The vertical magnetic racetracks allow for high density memory storage [3].

3.4 Chiral Spin Textures

As mentioned in the previously, DMI in concert with a strong Heisenberg interaction can induce complex spin textures in materials. This had been observed for some time in bulk DMI materials (crystal structures with broken inversion symmetry) but not in thin films. Following the prediction of DMI caused by broken surfaces and interfaces (termed interfacial DMI), the first observation of this effect in thin films was made in monolayer Mn on W(110). DMI on nominally antiferromagnetic Mn with a well-defined easy axis and hard axis resulted in a cycloidal spin spiral texture along one axis [25]. A cycloidal spin spiral is a texture in which a single sub-lattice (with the second sub-lattice antiparallel to the first) of the antiferromagnet rotates from a positive out-of-plane (OOP) direction to a negative OOP direction as the surface is traversed, similar to a one-dimensional Néel wall. Since this initial discovery, DMI has been used to create many other complex spin textures.

3.4.1 Skyrmions

Perhaps the most unusual of these spin textures is the magnetic skyrmion. A skyrmion is a type of topology characterized by a winding number equal to ±1. The winding number refers to the 1:1 mapping of moments in the skyrmions to a unit sphere. Skyrmions can be visualized by imagining a domain wall wrapped into a circle. There are two types of skyrmions analogous to the two types of domain walls discussed earlier. Bloch skyrmions resemble whirlpools with a single moment in the center pointing up (or down) with concentric circles of spins canted slightly off vertical in a ring. Moving radially away from the center the canting increases until eventually the moments are perfectly in plane at the midpoint radius of the skyrmion. At its edge, the canting

continues until a ring of moments pointing down (or up) is reached. The Bloch character is evident along radial directions of the skyrmion. Néel skyrmions resemble hedgehogs with relative out of plane moment components increasing radially moving outward. Again, along any radial direction the moments rotate about an axis normal to a surface formed by the radial direction and sample surface normal, consistent with a standard Néel domain wall.

Magnetic skyrmions had previously been observed in insulators exhibiting bulk DMI due to broken inversion symmetry of the B20 crystal structure [19,26,27], but with the discovery of interface induced DMI researchers began focusing on generating skyrmions in thin films. Due to the influence of the DMI, Néel skyrmions are found in thin films. Skyrmions in thin films have significant practical applications in information storage technologies. Skyrmions are topologically protected structures, meaning no continuous transformation can destroy a skyrmion. In real materials however, moments are not continuous but localized at atomic lattice sites, thus this strict topological treatment is only partially applicable. The result is that skyrmions are not immutable, but are stabilized against other topological states by some finite energy barrier [12]. While in a stable state skyrmions act as solitons, moving as a quasiparticle in response to applied forces [27,28]. Additionally, skyrmions can be extraordinarily small, down to a handful of nanometers. Finally, Néel skyrmions require relatively small currents to induce motion and are less influenced by surface defects in the sample than domain walls [29]. All of these characteristics make skyrmions a promising candidate for next-generation memory storage technology, particularly in racetrack memory. In this scheme, each skyrmion acts as a single bit with either chirality or the presence/absence of a skyrmion determining the bit value (1 or 0).
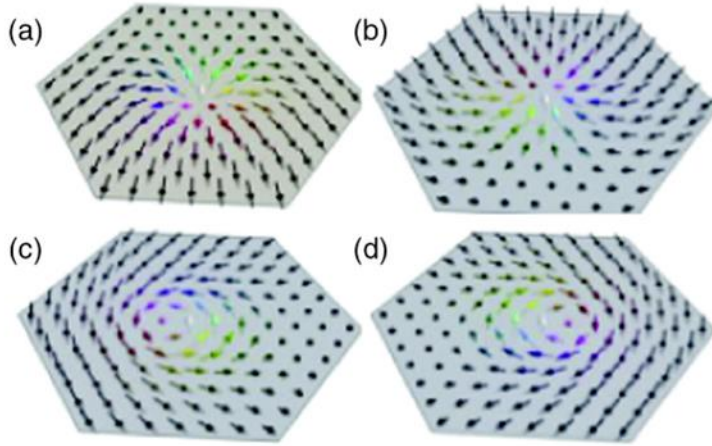
Fig. 3.3: Examples of different types of magnetic skyrmions. (a), (b) Néel type skyrmions (right-handed and left-handed). (c), (d) Bloch skyrmions (left-handed and right-handed chirality) [19].

The primary challenge in skyrmion research is to create small, stable skyrmions at room temperature in order to be technologically relevant. As might be expected from the complex spin texture, skyrmion formation requires a high DMI to occur [28,30]. Competition between the DMI and the Heisenberg exchange interaction often results in spin spirals at the surface of the material at zero external magnetic field [12]. The first demonstrations of skyrmions used monolayer Fe pseudomorphically grown on Ir(111) to generate high DMI and induce nanometer scale skyrmions [30]. While this initial experiment demonstrated small skyrmions under no applied field, these skyrmions proved difficult to manipulate. Subsequent work grew Fe/Pd bilayers on Ir(111) multilayers to create "writeable" skyrmions through the transformation of surface spin spirals (mentioned earlier in this section) to 2D skyrmions under application of high fields (>1 T) and very low temperatures (<10 K) [12]. Skyrmions have been nucleated using applied field pulses, spin-orbit torque current pulses, and spin current injection in some scanning tunneling microscopy experiments [28]. Room temperature skyrmions as small as 30nm have been observed in repeated Pt/Co/Ir stacks used to enhance DMI to almost 2 mJ m^{-2} and larger, micron-sized room temperature

skyrmions are seen in Ta/CoFeB [27]. Skyrmions can also be selectively nucleated at particular points by inducing an anisotropy change in the sample surface. Thus, by patterning a magnetic track with a constriction, one can nucleate skyrmions exclusively at the constriction by applying a current pulse across it [31].

3.4.2 Homochiral Domain Walls

Intermediate DMI strength can also affect domain walls, stabilizing Néel walls in thin films with PMA. In current-induced domain wall motion, micromagnetic calculations show that the DMI creates an effective magnetic field parallel to the current direction [24,32]. As a result, externally applied longitudinal magnetic fields can serve to further stabilize or destabilize the Néel wall resulting in significant changes in domain wall velocity for a given applied current. In addition, with sufficient DMI, the domain walls adopt a single chirality, i.e. all of the domain wall moments rotate in the same direction along the direction of the domain wall midpoint moment. These homochiral domain walls have advantageous dynamics allowing for high-speed current induced motion [24]. The DMI strength additionally acts as a "speed limit" for current-induced domain wall motion with ferromagnets [6,33]. The terminal velocity of domain walls is dependent upon the gyromagnetic ratio and saturation magnetization, and directly proportional to the Dzyaloshinskii constant:

$$v_{max} = \frac{\gamma}{M_S}\frac{\pi}{2}D \qquad (3.5)$$

Thus, the DMI is a critical factor in improving the speed of ferromagnetic racetrack memory devices.

3.5 Previous Work on DMI in Thin Films

DMI is important in controlling the spin textures of magnetic materials such as skyrmions and cycloids, or, in the absence of such a complex texture, for the introduction of magnetic chirality to domain walls. In films with PMA, strong DMI stabilizes homochiral Néel domain walls and allows for fast, efficient current-induced domain wall motion. In these systems, DMI acts as a speed limit on current-induced domain wall motion [6]. As a result, controlling the strength and sign of DMI (to toggle chirality) is of considerable interest.

3.5.1 Ferromagnetic Systems

DMI in thin films is an interfacial effect that relies on the interaction of two magnetic atoms in conjunction with a non-magnetic atom with high spin-orbit coupling. Thus, to induce DMI in thin films typically a ferromagnetic layer is deposited above or below a heavy metal layer. When the ferromagnetic layer is deposited on top of certain heavy metals, PMA can be induced as well [19]. Interfacial DMI has been observed for a variety of heavy metal/ferromagnetic interfaces through domain wall motion experiments, Brillouin light scattering (BLS), and through computational modeling techniques. These interfaces include Co, Ni, Fe, CoFe and CoFeB on Pt, Pd, Ta, Au, W, or Ir [19,28,34–36]. Pt, in addition to its high spin-orbit coupling induces PMA when interfaced with a ferromagnet and exhibits the spin Hall effect (SHE) [37]. Consequently, Pt is a staple of multilayers for such purposes. Analysis of these materials has shown the Pt/Co and Ir/Co DMI to be the strongest at room temperature while Au exhibits weak DMI with the other metals taking up intermediate values [34,38]. Of additional note, different heavy metals, such as Pt and Ir, have different signs of the Dzyaloshinskii vector, resulting in opposite chirality spin

textures, notable right versus left-handed domain walls. By combining interfaces of positive and negative DMI, the total DMI in the multilayer stack can be enhanced or reduced, depending on the layer ordering. For example, Pt/Ir/[Ni/Co]$_n$ multilayers display lower net DMI than identical multilayers without Ir due to Pt and Ir having opposite signs of DMI [39]. However, by swapping the placement of the Ir layer to the top of the stack the net DMI is enhanced as the two opposite DMI interfaces now act in the same direction when one interface in flipped [36].
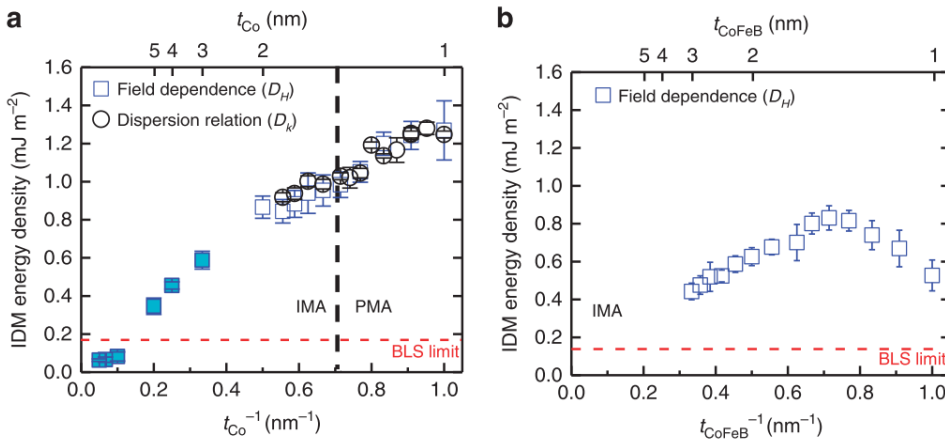
Fig. 3.4: Plot of DMI (here IDM) energy as a function of inverse ferromagnetic layer thickness demonstrating a clear inverse proportionality between ferromagnetic layer thickness and DMI strength in (a) Pt/Co/AlOx and (b) Pt/CoFeB/AlOx. The deviation from proportionality below 1.5 nm of t$_{CoFeB}$ in expected DMI in (b) is likely due to poor interfacial coverage. Adapted from [40].

While the sign of the DMI remains consistent for heavy metals interfaced with a variety of different ferromagnets, the magnitude of the interaction is affected by the ferromagnet and thus, of the specific interface. As a result of the interfacial nature of the interaction, the total DMI in films is inversely proportional to the thickness of the magnetic layer of the film [40]. This inverse proportionality results in a severe reduction in DMI strength in films just a few nm thick. The

thickness of the heavy metal layer has also been shown to weakly impact DMI strength, albeit not nearly on the same magnitude as the ferromagnetic layer thickness. In $Co_{40}Fe_{40}B_{20}$/Pt/Cu the DMI strength begins to taper off as the Pt thickness drops below 3 nm, losing about 0.5 mJ m^{-2} of strength (in comparison to a maximum value of 0.45 mJ m^{-2} above 3 nm Pt) and precipitously drops off below 1.5 nm [35]. This result suggests that the DMI does not solely involve the ferromagnetic and non-magnetic monolayers immediately comprising the interface but is also impacted by a few atomic layers on either side of the interface. Computational modeling of Pt/Co interfaces confirms the small influence of additional layers of Pt to increase DMI while additional layers of Co have opposite chirality interactions which lead to an overall decrease in DMI strength [28,34]. Other work has found the DMI and Heisenberg exchange to be proportional, suggesting that the DMI variation with thickness is due to the Heisenberg exchange strength variation with thickness, however, the reason for this thickness dependence is unclear [41].

Although certain literature has suggested that DMI may be enhanced by proximity-induced moments in the heavy metal layer when interfaced with the ferromagnet [42], modelling has shown that the opposite occurs and that only the spin-orbit coupling the heavy metal layer affects DMI [34]. As might be expected, because the DMI is primarily facilitated through the two monolayers adjacent to the interface, the quality of the interface may dictate the DMI strength as well. Interfacial mixing of 25% has been predicted to reduce DMI by a factor of two [34]. Low interfacial quality (intermixing, poor coverage) may account for DMI strengths below their expected value in ultrathin ferromagnetic multilayers with ferromagnetic thicknesses below 1.5 nm.

3.5.2 Ferrimagnetic Systems

So far, we have focused on ferromagnets interfaced with heavy metals. However, ferromagnetic multilayers have inherent limitations due to their stray-fields and domain wall dynamics. The stray fields lead to limitations in the size of domains, inconvenient for memory applications. Domain wall dynamics are governed by the Landau-Lifshitz-Gilbert (LLG) equation which describes the effect of effective fields on magnetization over time:

$$\dot{m} = -\gamma m \times H_{eff} + \alpha m \times \dot{m} \tag{3.6}$$

Here m is the normalized magnetization, γ is the gyromagnetic ratio of the ferromagnet ($\gamma = \frac{g\mu_B}{\hbar}$, with g the electron spin g-factor), and α is the Gilbert damping constant. H_{eff} is the total contribution of all effective magnetic fields including externally applied fields, demagnetizing fields arising from stray-field energy, ferromagnetic exchange fields, and anisotropy fields. The first term causes the magnetization to precess around the effective field. With only this term, the magnetization would never align with an applied field. The second term dampens the precession and causes the magnetization to spiral inward toward the direction of the effective field. This precession results in sub-optimal domain wall motion due to a phenomenon called Walker breakdown, in which domain wall velocity slows above a critical effective field. Ferrimagnetic multilayers offer an opportunity to overcome the limitations in ferromagnets by taking advantage of some of the attractive features of antiferromagnets, such as low net moments and spin densities, while remaining readable through each sublattice [6].
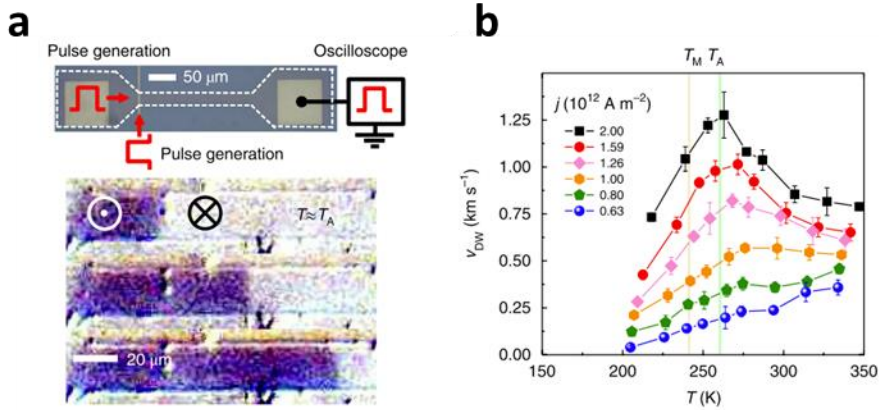
Fig. 3.5: (a) Schematic of domain wall track and corresponding MOKE images of domain wall in motion. (b) Plot of domain wall velocity versus sample temperature detailing a peak velocity at the angular momentum compensation temperature, T_A. Adapted from [6].

Recent experiments with ferrimagnetic multilayers have demonstrated their beneficial properties. Just as in ferromagnetic multilayers, DMI promotes homochiral Néel domain walls in ferrimagnetic multilayers [43]. In ferrimagnetic multilayers, velocity is capped by the current density j, DMI strength D, and spin density S by [6]:

$$v_{FiM} = \frac{\pi}{2} \frac{Dj}{\sqrt{(S(T)j)^2 + (S_0 j_0)^2}} \tag{3.7}$$

At angular momentum compensation, the spin density is zero and precessional dynamics are eliminated, reducing the denominator and allowing for significantly higher domain wall velocities. Velocities over 5.7 km/s have been observed in GdCo ferrimagnets [44]. Small stray fields also have advantages in skyrmion research. Skyrmions are typically destabilized by stray fields as thickness is increased in ferromagnets. Near magnetic compensation in ferrimagnets, small (10 nm) skyrmions have been observed near room temperature [6].

Evidence of a bulk-like DMI has been observed in GdFeCo [26]. This DMI is observed in spite of GdFeCo's lack of any symmetry and without interfacing a heavy metal with high spin orbit coupling with the amorphous layer. Additionally, in contrast to interfacial DMI, the DMI does not decrease inversely with increasing thickness. Instead, it increases directly proportionally to thickness, a telltale sign of a bulk effect. As a final confirmation of the bulk effect, interfacing GdFeCo with heavy metals (Cu, Pt) has no effect on the DMI-thickness proportionality. Transmission electron microscopy (TEM) analysis of the co-sputtered alloy along its growth direction reveals a gradient in composition. This suggests that a composition gradient in an amorphous ferrimagnet sufficiently satisfies the broken inversion symmetry condition of DMI.

3.6 Rare-Earth Transition-Metal Ferrimagnetic Alloys

The material class studied in this thesis is amorphous rare-earth (RE) transition-metal (TM) alloys. These alloys garnered considerable interest in the latter half of the 20^{th} century for their immediate applicability in magneto-optical recording technology [45]. In general, RE-TM alloys consist of two distinct sublattices that are governed by three exchange interactions: J_{TM-TM}, J_{RE-TM}, and J_{RE-RE}. Due to the localized $4f$ orbitals present in RE atoms, typically J_{RE-RE} is negligible and J_{TM-TM} dominates exchange. The sign of J_{RE-TM} is dependent on the particular RE element and determines the overall RE-TM alloy magnetic order. Elements with $Z \geq 64$, that is, the atomic number of Gd, have $J_{RE-Co} < 0$ and accordingly exhibit ferrimagnetic behavior. In contrast, elements with $Z < 64$, such as Dy have oppositely oriented moments due to Hund's rules and are governed by ferromagnetic exchange [46,47].
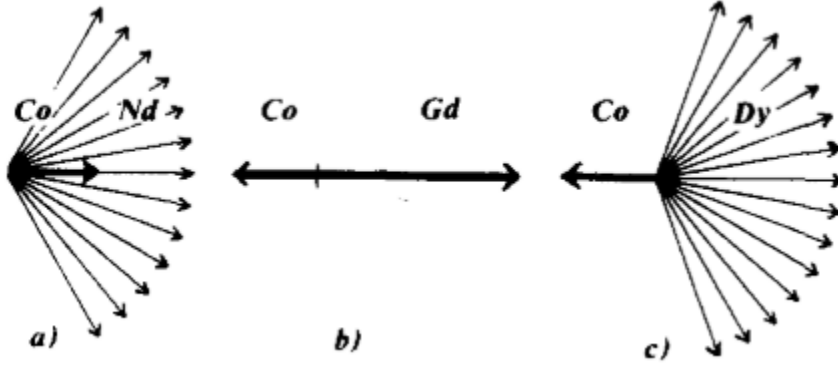
Fig. 3.6: Schematic showing three different types of order in RE-TM amorphous alloys. (a) Speromagnetic ordering, observed when the RE element has $Z < 64$. (b) Colinear ferrimagnetic ordering observed in GdCo. (c) Non-colinear ferrimagnetic ordering, or sperimagnetism, found when the RE has $Z > 64$. Adapted from [46].

In addition to the usual Heisenberg exchange interactions, the RE element can introduce site-level anisotropy due to their crystal fields. This adds an additional term to the effective exchange [46,48,49]:

$$E_H = \sum_i -A_i S_{i,z}^2 + \sum_{i,j} -J_{ij} \mathbf{S_i} \cdot \mathbf{S_j} \tag{3.8}$$

where $\mathbf{A_i}$ is a randomly oriented vector. While this exchange is generally applicable to amorphous alloys, in practice the first term is only significant in RE atoms with significant orbital angular momentum (non S-state elements), such as Nd, Dy, and Tb. The result of this term in applicable RE-TM alloys is to create non-colinear ferrimagnetic ordering as shown in Fig. 3.6. Ideal ferrimagnetic ordering, as observed in GdCo alloys is shown in Fig. 3.6(b). TbCo and DyCo exhibit sperimagnetism, resulting in a distribution of Tb atomic moments described by a cone angle (Fig. 3.6(c)). When the TM is replaced with Fe, the situation becomes even more complex, with both the RE and Fe moments exhibiting a cone distribution about the AFM coupling axis.

The key RE-TM alloys of interest in this thesis are GdCo and TbCo. In these alloys, the rare-earth element and transition metal are antiferromagnetically coupled, i.e. Gd spins pointing up with Co spins pointing down. Unlike an antiferromagnet, however, the spins in each sublattice do not compensate each other completely. This results in a net magnetization in ferrimagnets. In general, each sublattice has a unique Curie temperature and unique temperature dependence as a result. Because each elemental sublattice is magnetized in the same direction, bulk magnetic properties in the material such as saturation magnetization (M_s) and coercivity (H_c) can be tuned by altering the composition of the alloy (thereby changing the ratio of up spins to down spins) or by changing the temperature in order to change the ratio of moment strengths in each sub-lattice. At particular combinations of composition and temperature, it is possible to reduce the net magnetization to zero, called magnetic compensation. In addition to magnetic compensation, ferrimagnets can have compensated angular momentum in their lattices as well when the net spin density drops to zero in the material. This is possible in rare-earth transition metal ferrimagnets due to their distinct Landé g-factors [50]. This large array of tunable properties provides a multitude of opportunities to enhance existing spintronics devices, making ferrimagnets an increasingly interesting material to study.

4 Experimental Methods

This thesis utilizes several experimental techniques to study rare-earth (RE) transition metal (TM) ferrimagnetic alloys. The purpose of this chapter is to introduce the methods used for growth, fundamental magnetic property characterization, and spin transport characterization of magnetic thin films.

4.1 Sputter Deposition

All samples studied in this thesis were grown via DC magnetron sputter deposition. First developed in the 1800s, sputter deposition is a type of physical vapor deposition (PVD) widely used today for thin film growth in a variety of industries such as semiconductor manufacturing and for optical coatings [51,52]. A schematic of a typical sputter deposition process is shown in Fig. 4.1. Sputter deposition is a high vacuum process typically done at a background pressure below 10^{-5} torr. Lower background reduces oxidation and impurities in the deposited film. The RE-TM alloy-based heterostructures grown for this work had a background pressure $< 2 \times 10^{-7}$ Torr. Once a sufficiently low background pressure is achieved, an inert, heavy sputtering gas (typically Ar) is flowed into the vacuum chamber at a pressure of $\sim 10^{-3}$ Torr. In this regime, the sputter deposition rate is approximately proportional to the sputtering gas pressure. A high voltage on the order of a couple hundred volts is applied between the target/sputter gun (cathode) and substrate (anode), ionizing the sputtering gas. The Ar^{+} ions are then accelerated by the electric field into the target, initiating a cascade of collisions within the target that results in ejection of target atoms from the target surface onto the substrate. Modern sputter guns generally employ magnetrons to increase the sputtering rate (Fig. 4.2). These utilize magnetic fields produced by static pole pieces

to create a magnetic field around the target surface. The field traps free electrons originating from the ionized gas in a confined region above the target. The high density of electrons near the target surface results in increased ionization leading to higher incident Ar^+ flux on the target and higher sputter deposition rates [51,53].
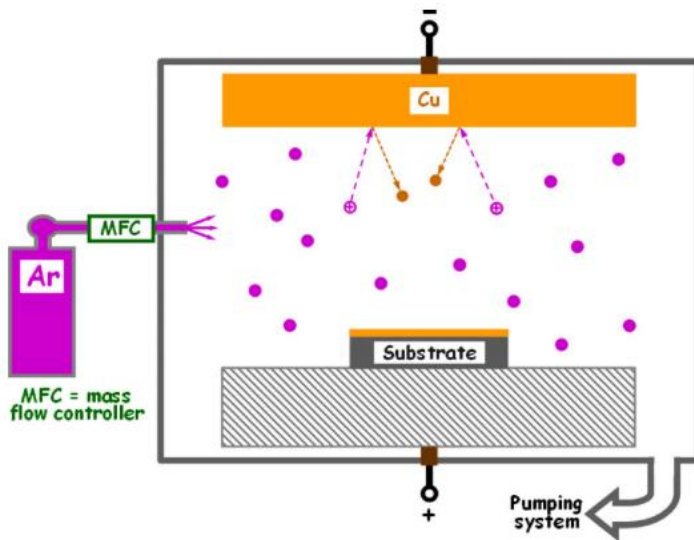
Figure 4.1: Sputter process schematic, from Greene [51]. Ar is the sputtering gas that is ionized and accelerated into the target material (Cu), resulting in Cu condensing on the substrate. In our sputtering system, the target and substrate are flipped, such that the substrate is oriented upside-down.

In contrast to other PVD techniques, such as evaporation, sputter deposition can be done at temperatures well below the melting point of the depositing material. Increasing the substrate temperature enhances adatom surface diffusion, increasing the grain size of the deposited layer. The grain morphology is illustrated in zone diagrams that schematically show texture as a function of homologous substrate temperature and Ar pressure [54–57]. All samples grown in this work

were grown at ambient substrate temperatures, resulting in fine, columnar, polycrystalline grain structures for pure layers. However, RE-TM sputtered alloys have been shown to be amorphous when deposited under these conditions [46]. Additionally, despite its reliance on an applied voltage between target and source, both conductive and non-conductive target materials can be used by switching from DC to RF applied voltages to prevent charge accumulation on insulating targets. As a result, sputter deposition provides a flexible method for growing thin films, regardless of composition constraints.
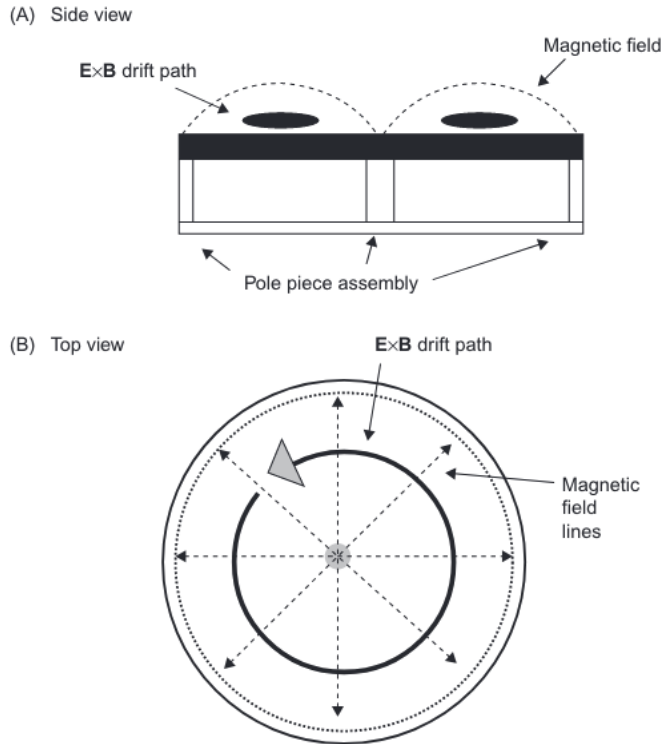
Figure 4.2: Magnetron sputter gun, from Simon [52]. (A) Cross-sectional side view of gun, showing the magnetic pole pieces and magnetic field lines emanating from target surface. (B) Top view of gun, showing the drift path of electrons caught in the magnetic field.

The overall versatility of sputter deposition makes it particularly attractive for the studies presented in this thesis, where a wide composition range and a variety of thicknesses of RE-TM alloys are required. The sputtering system used in this work consists of four sputter guns mounted to the base of the vacuum chamber each with individually controlled shutters to block the ejected target material. The substrates are mounted upside down on up to four sample holders on a rotating platter. A second platter with six holes can be coupled to the sample holder platter and selectively covered or left open to control which samples are exposed to the sputter guns. The substrate rotation increases film uniformity and allows one to sputter alloys by running two or more guns simultaneously. The deposition rate of a target is proportional to the power through the gun. Since the voltage is relatively constant over a known current range, a current-limited power supply can be used to linearly tune the deposition rate. This is useful for deposition of ultrathin films when high accuracy is required, or for sputtering two materials at once (termed "co-sputtering") as in the case of RE-TM alloys, where tuning the relative deposition rates results in different volume fractions of RE and TM in the film. The densities and molar masses of the deposited elements can be used to convert these volume fractions to atomic fractions with high accuracy, limited by the deposition rate calibration accuracy of each target. Deposition rates were determined for each target/gun configuration using X-Ray reflectometry on simple bilayer calibration films with thicknesses ranging from 10 – 30 nm to an accuracy of ~1%. Propagating this uncertainty through the atomic fraction calculation and accounting for minor imprecision in the timing of the depositions to around one second, the typical error in the atomic fraction of the RE-TM alloys grown was estimated to be < 2 at. % RE.

4.2 Vibrating Sample Magnetometry

The primary technique used to quantify the magnetization of films studied in this thesis was vibrating static magnetometry. A schematic of a vibrating static magnetometer (VSM) is shown in Fig. 4.3. A VSM consists of a coupled pair of electromagnet coils, ferrite poles to focus the applied magnetic field, and a quartz sample rod suspended vertically from a vibrating head piece above the electromagnet. The maximum programmable field of the VSM used in this work was ~1.3 T. A gaussmeter is typically inserted near one of the pole pieces to monitor the applied field and provide continuous feedback to the electromagnet power supply for improved accuracy. The magnetic film is attached to the end of the sample rod in either an out-of-plane configuration (OOP, film normal to the applied field) or in-plane configuration (IP, film parallel to the applied field). The VSM head is attached to a swivel that allows for continuous 360° rotation of the sample with respect to the applied field. The VSM head and attached sample rod are mechanically isolated from the electromagnet, meaning that when the vibration in the head is activated, the sample oscillates vertically (along the z-axis in Fig. 4.3) with respect to the electromagnet, and consequently, the applied magnetic field. The magnetized sample emits its own stray fields that pass through the sensing "pickup" coil with a magnitude that changes as the sample oscillates. By Faraday's law of induction and Lenz's law, the changing magnetic flux through the coil induces a voltage in the coil, $V_{ind} = -\frac{d\Phi_B}{dt}$. For a VSM sensing coil, this translates to an induced voltage proportional to the amplitude, A, and frequency, f, of vibration, $V_{ind} = mAfS$, where m is the magnetic moment of the sample and S is the sensitivity constant of the pickup coil which is related to the number of windings and electrical noise of the system [58]. As a result, a large amplitude and high frequency is generally desirable for maximum instrument sensitivity, within practical limits. The sensitivity

of the primary VSM used in this work was $\sim 3 \times 10^{-6}$ emu. To convert the induced voltage in the coil to a magnetic moment, a standard ferromagnetic sample, such as pure Ni, is used for calibration. Due to the geometry of the coils, the VSM measured the magnetization projected along the field direction (x-axis in Fig. 4.3). The VSM used in this work had a nitrogen flow temperature controller as well, allowing for measurement of samples from -160 °C to over 300 °C.
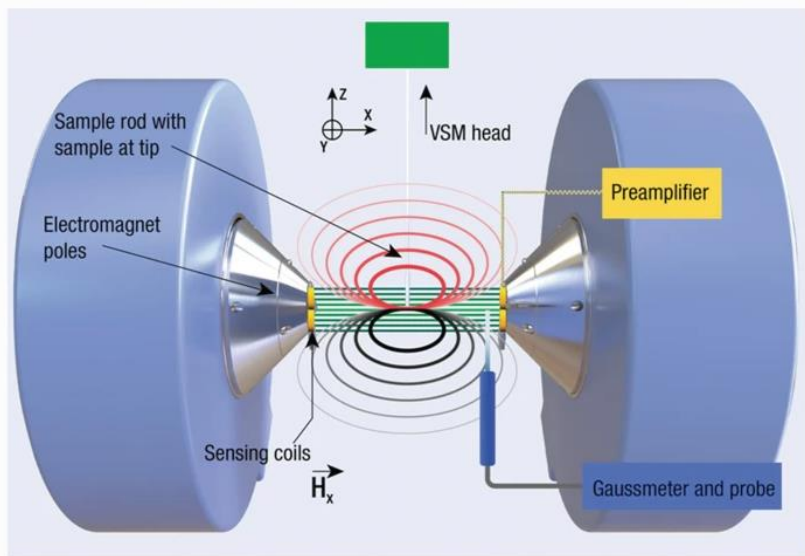
Figure 4.3: Typical VSM layout, showing electromagnet coils in blue with corresponding pole pieces and induced magnetic field (green lines). The sample of interest is placed on the tip of the vibrating sample rod and the sensing coils detect the changing magnetic field flux emitted from the sample. Image from [58].

The two primary disadvantages of VSM measurements are the long acquisition times and B-field measurement scheme. The large inductance of the electromagnet inhibiting the ramp time of the magnetic field combined with the long averaging times required to get accurate low-moment signals make acquiring a single hysteresis loop take anywhere from 5 – 60 minutes, depending on

the field resolution required. This makes VSM impractical for certain field measurements such as coercivity. Additionally, because VSMs operate via induction, they are sensitive to the net magnetization of all vibrating matter attached to the head. Consequently, the diamagnetic signal from the quartz sample holder as well as any contaminating impurities stuck to the rod or sample are added to the total signal, so very careful handling and mounting of samples is necessary for accurate results. This also means that the substrates (typically diamagnetic Si in this work, see Fig. 4.4(a)) that the magnetic films are deposited on affect the final measured moments. Practically, the result of this limitation is that full hysteresis loops up to fields well beyond the saturation fields of the films are required in order to extract a reliable saturation magnetization, M_s. The linear diamagnetic and paramagnetic background contributions of the substrate and sample holder can then be removed to isolate the magnetic layer's hysteretic behavior (see Figs. 4.4(b) and (c)). Additionally, it should be noted that VSMs only measure total magnetic moment, and additional knowledge or assumptions are required to normalize this moment by the magnetic film volume. In this work, the nominal thickness of the magnetic film layer was calculated based on the sputter deposition time and deposition rate. The area of the film was determined by photographing the sample on grid paper as a pixel length reference and using the software ImageJ to determine the boundaries of the film and subsequently count the number of pixels contained within the film.

In addition to measuring M_s, VSM was used to determine the anisotropy of the grown RE-TM film stacks. The orientation of the samples was rotated to align the applied field with the magnetic hard-axis. The anisotropy field was then extracted from the measured hard-axis hysteresis loop (Fig. 4.4(d)) by fitting the positive, negative, and transition branches of the loop and extrapolating the intersection points. This method was used for films with anisotropy fields below ~7000 Oe in order to get accurate fits at saturation given the limited range of the VSM. For

higher anisotropy films, longitudinal MOKE magnetometry at normal incidence was used to determine the saturation field.
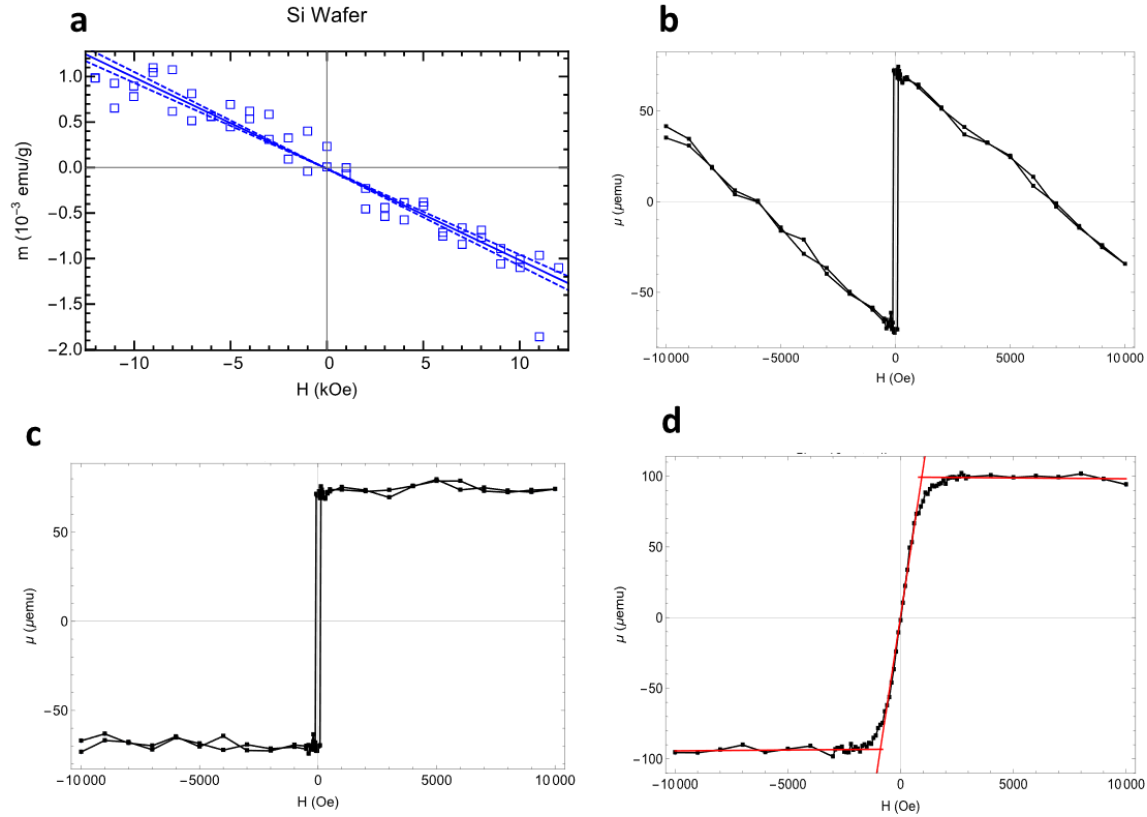
Figure 4.4: Collected VSM hysteresis loops. (a) Linear diamagnetic response of thermally oxidized Si wafer used as a substrate for RE-TM ferrimagnetic layers, normalized by mass, at 295 K. (b) Representative raw hysteresis loop of Si/Ta/Pt/Gd$_{0.27}$Co$_{0.73}$(3 nm)/Ta/Pt stack measured OOP, showing the influence of Si substrate moment on total moment. (c) Hysteresis loop of same stack with Si diamagnetic contribution removed, isolating the GdCo magnetic contribution to reveal a saturation moment of ~70 μemu. (d) A similar stack measured IP, showing a characteristic uniaxial hard-axis loop with $H_k \approx 900$ Oe.

4.3 Magneto-optical Kerr Effect Magnetometry

In addition to VSM, the other main technique used to measure magnetic hysteresis loops in this work is magneto-optical Kerr effect (MOKE) magnetometry. There are three possible geometries for MOKE magnetometry depending on the relative directions of incident light and magnetization of the sample: polar, longitudinal, and transverse (Fig. 4.5). In the polar and longitudinal geometries, incident polarized light reflected off a magnetized surface undergoes a rotation and change in its ellipticity due to the MOKE, proportional to the surface's magnetization (in the transverse geometry, only the intensity of the reflected light is affected). A similar phenomenon occurs in transmission (the Faraday effect). As a result, the magnetization of a sample is determined by measuring the polarization state of the reflected light.
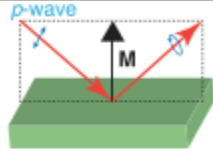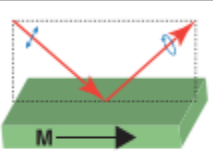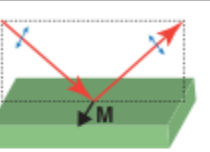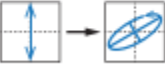
Name	(a) Polar	(b) Longitudinal	(c) Transverse
Geometry	p-wave M	M→	M
Detection	Out-of-plane	in-plane	in-plane
Polarization Variation	Rotation Ellipticity		None
Measurement	Polarization Analysis		Intensity measurement

Figure 4.5: Three possible geometries of MOKE measurements. (a) Polar, with M normal to the film surface. (b) Longitudinal, with M parallel to the film surface and plane of incidence. (c) Transverse, with M parallel to the film surface and perpendicular to the plane of incidence. Only the polar and longitudinal geometries affect the polarization state of the reflected light. Image from [59].

The extent of polarization rotation and induced ellipticity are quantified by the material's Kerr rotation, θ_k, and ellipticity, ϵ_k, angles. Because light ellipticity originates from a phase shift in orthogonal components of a ray of light, the Kerr parameters are often combined into a single complex Kerr angle, $\Phi_k = \theta_k + i\,\epsilon_k$. The Kerr angle can be extracted using ellipsometry or using a MOKE magnetometer (see Chapter 5: Measurement of Kerr Rotation and Ellipticity in Magnetic Thin Films by MOKE Magnetometry", for details). For RE-TM ferrimagnetic alloys, in which the two sublattices are antiferromagnetically coupled, the net complex Kerr angle can be represented as the difference between each sublattice's individual contribution, $\Phi_{k,net} = \Phi_{k,RE} - \Phi_{k,TM}$. The magneto-optical response in TM is from d $\rightarrow$ d band transitions and d $\rightarrow$ f band transitions in RE, making $\Phi_{k,TM}$ dominant at IR and visible frequencies and $\Phi_{k,RE}$ dominant at UV frequencies [60,61]. This allows us to use MOKE magnetometry to probe a single sublattice magnetization. By tracking the polarity of a MOKE hysteresis loop (i.e. whether the measured intensity is higher at positive or negative saturation, see Fig. 4.6) under constant measurement parameters (the analyzer and, optionally, quarter waveplate angle), we can then determine whether a given sample is RE or TM dominated, an important piece of information for determining the magnetic compensation point in RE-TM composition series.
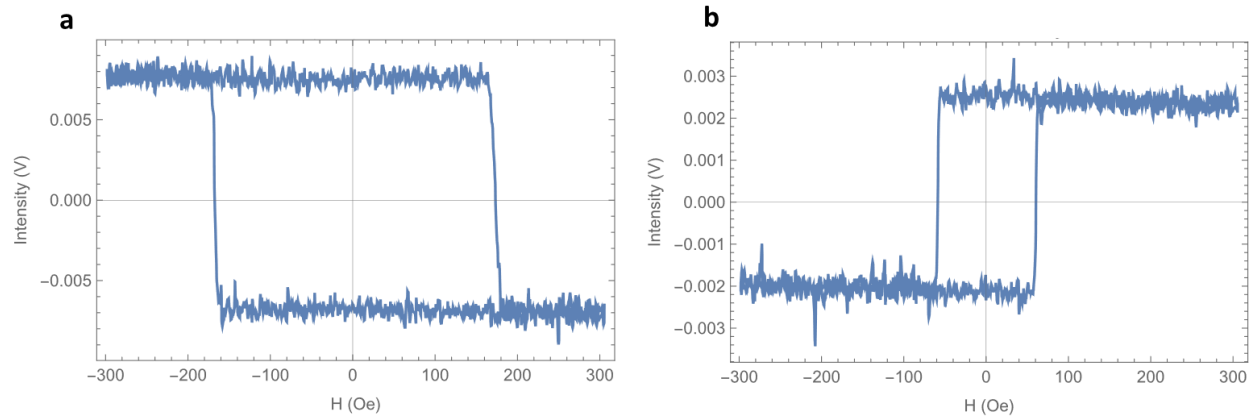
Figure 4.6: Laser MOKE hysteresis loops of (a) Co-dominated 3nm $Gd_{0.27}Co_{0.73}$ and Gd-dominated 6nm $Gd_{0.35}Co_{0.65}$, showing the difference in loop polarity.

4.3.1 Laser MOKE Magnetometry

A MOKE magnetometer setup for both localized laser measurements and wide-field measurements is shown in Fig. 4.7. The key components necessary for any MOKE magnetometer are a light source, input polarizer to set the incident polarization, quarter waveplate, output polarizer (analyzer), and a photodetector. In this section, we will focus on laser MOKE magnetometry. In our lab, we utilize both 532 nm and 635 nm with spot sizes of ~1 μm. For a polar geometry, other optical components such as beamsplitters and mirrors are necessary as well to redirect reflected light away from the source and into the detector. The raw detected signal in our MOKE systems is a few nanoamps, so the photodetector is first routed through a 10^6 gain transresistance amplifier, and then through a bandpass filter to reduce mechanical and optical noise. The quarter waveplate is used to compensate for the induced ellipticity of the reflected light beam but is sometimes neglected in MOKE systems. Its function is to apply a phase shift between the orthogonal electric field components, depending on the waveplate angle, converting the elliptical

light to purely rotated linearly polarized light, enhancing the intensity difference (signal) between +M and -M after passing through the analyzer. Practically, however, MOKE hysteresis loops can be acquired without a quarter waveplate in materials with significant θ_k at the cost of reduced signal-to-noise ratio (SNR).
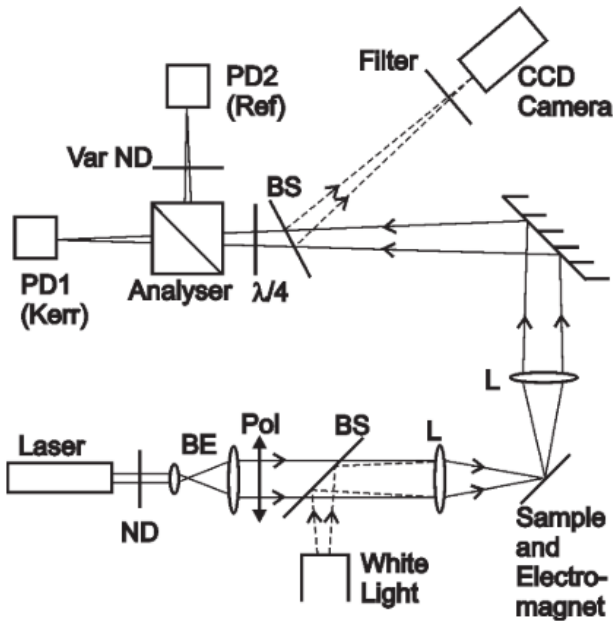
Figure 4.7: Schematic of combined laser and wide-field MOKE magnetometer [62]. PD: photodetector, ND: neutral density filter, BS: non-polarizing beamsplitter, L: lens, BE: beam expander.

The key advantage of laser MOKE magnetometry over VSM is its superior data acquisition speed. Whereas ~15 s/point of averaging is required for an accurate moment measurement in VSM, the intensity at each point is captured in microseconds. Thus, laser MOKE hysteresis loop acquisition time is limited only by the electromagnet ramp speed. For air coils with low inductive loads, the ramp time can be as fast as ~20 kOe/s up to a maximum field of ~2 kOe. Higher fields

(up to ~17 kOe in our longitudinal MOKE magnetometer) require ferrite cores and generally have more significant inductance, limiting their ramp times to ~3.3 kOe/s. For high-quality hysteresis loops, 15 – 100 loops are often averaged, making the total acquisition time on the order of ~1 min compared with > 20 min for a comparable VSM loop. Due to its high efficiency, laser MOKE magnetometry was used extensively to characterize the shape of hysteresis loops in order to determine critical characteristics such as the coercive field, direction of magnetic easy axis (in-plane or normal to the plane), and saturation field.

4.3.2　Wide-Field MOKE Microscopy

Wide-field MOKE microscopy follows the same operating principles as laser MOKE magnetometry, replacing the laser with a LED and photodetector with a CCD or CMOS camera. MOKE microscopy allows one to image magnetic domains. This capability was used to measure the position of domain walls on magnetic racetracks in order to determine their velocity under an applied current. Unfortunately, LEDs have low intensity relative to lasers, resulting in a lower SNR than laser MOKE magnetometers. While a well-tuned laser MOKE magnetometer can acquire a clean hysteresis loop in a single cycle taking ~200 ms (SNR > 1), that same sample analyzed in a MOKE microscope with an equivalent cycle time would produce an incomprehensible hysteresis "loop" (SNR << 1). As a result, MOKE microscopy generally requires long exposure times or averaging multiple frames to resolve magnetic domains.

To acquire a MOKE microscope image detailing regions of positive, negative, and zero magnetization, two reference images are required with the sample positively and negatively saturated. The two reference images are then averaged together to create a new frame, F_{ref}, that establishes the zero-magnetization baseline intensity for the given field of view. Once the reference

image is saved, newly acquired frames, F_{new}, are compared to the reference to produce the contrast image,

$$F_{contrast} = G \frac{F_{new} - F_{ref}}{F_{new} + F_{ref}} \qquad (4.1)$$

where G is a gain factor required to visually see the difference between positively and negatively magnetized domains. The normalization is done to minimize the effects of changes in light source intensity relative to the reference image. An example of a wide-field MOKE microscope image is shown in Fig. 4.8.
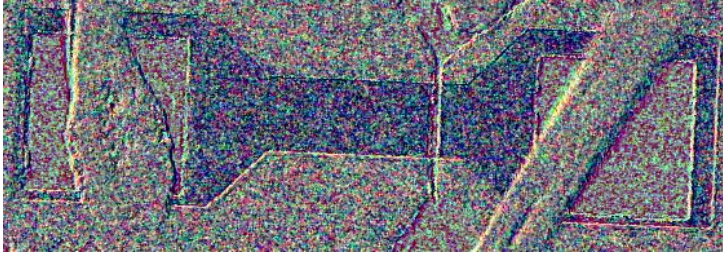
Figure 4.8: Wide-field MOKE microscope image of 8 nm $Gd_{0.35}Co_{0.65}$ magnetic racetrack. The blue region is down-magnetized (into the page) whereas the surrounding gray regions are non-magnetic. The contrast here has been multiplied by 128 ($G = 128$).

At the start of my graduate work, I initially inherited a MOKE microscope prototype built by previous members of my lab for domain wall motion measurements in ferromagnets and > 6 nm GdCo samples. However, due to the low thickness (3 nm) and unusually high Gd concentrations in my composition series (the highest sample I measured was over 50 at.% Gd whereas typical samples measured before were ~35 at.% Gd), the observed contrast in images was unacceptably poor for reliable domain wall position extraction. As a result, a number of redesigns were necessary

to improve the SNR of the system, carried out by me and fellow group member, Siying Huang. In the following sections I describe the key improvements made to the system.

Analytical Expressions for Signal and Noise in Wide-Field MOKE Microscopy

The first step in improving the observed contrast of the MOKE microscope was to quantify its signal and noise contributions to understand where improvements could be made to either boost signal or reduce noise. In MOKE magnetometry (polar and longitudinal), the signal is a result of a change of polarization state transformed into an intensity difference by means of a quarter waveplate and analyzer. This is normalized by the average intensity, $\bar{I}$, to give the normalized MOKE signal,

$$S = \frac{\Delta I}{\bar{I}} \tag{4.2}$$

where $\Delta I = I_+ - I_-$, that is, the difference in intensity between a positively and negatively magnetized sample. The normalized MOKE signal is generally a function of the Kerr angle of the sample, the quality of the optical system, and the analyzer, ϕ_A, and quarter waveplate, ϕ_W, angles. In the context of MOKE microscopy, in which the SNR is usually low, we are interested in maximizing S. The maximum signal is then,[1]

$$S_{max} = \left| \frac{\Delta I}{\bar{I}} \right|_{max} = \frac{2|\Phi_k|}{\sqrt{\gamma_D}} \tag{4.3}$$

Here, γ_D is the depolarization factor, a measure of the extent of depolarization in the system equal to the reciprocal of the extinction ratio. From this expression we see why the 3 nm GdCo composition series exhibited significantly worse contrast than previously measured 6 nm GdCo. As established previously, the Kerr angle of Co is dominant in the visible light regime, meaning

---

[1] See Chapter 5 for the derivation of this expression

$|\Phi_k|$ decreases as the concentration of Gd increases. Additionally, the low thickness of the magnetic layer further reduces $|\Phi_k|$ due to its small interaction volume.
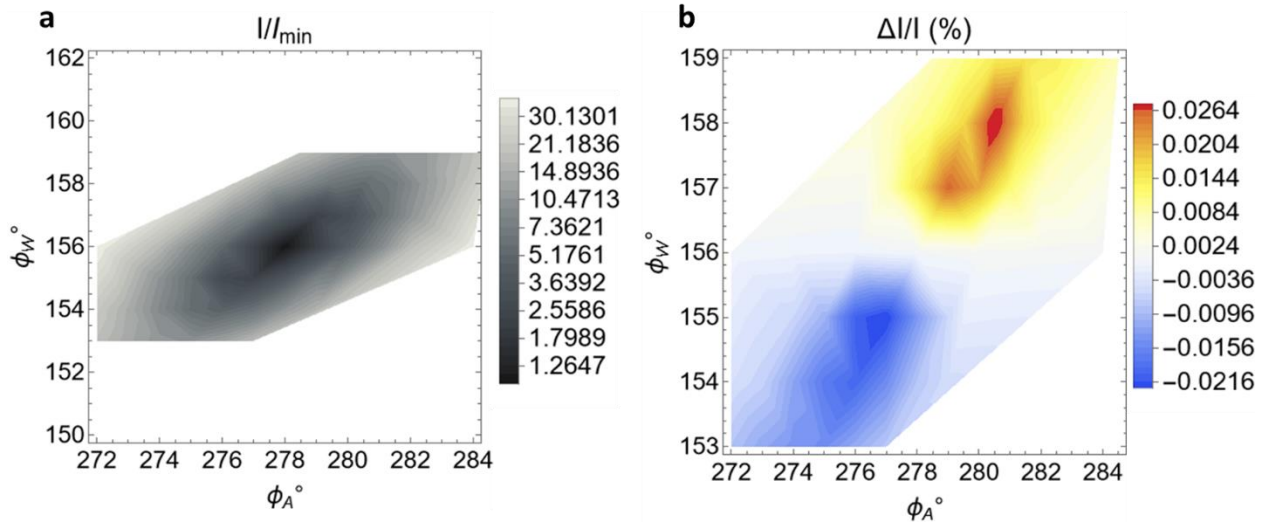
Figure 4.9: Contour plots showing representative (a) intensity as a function of analyzer and waveplate angle with extinction at $\phi_A \approx 278°, \phi_W \approx 156°$ and (b) normalized MOKE signal, S. The extrema of S straddle the extinction point.

S is maximized at particular values of ϕ_A and ϕ_W that in general are functions of θ_k, ϵ_k, and γ_D.[2] Experimentally, γ_D can be determined by measuring the intensity of reflected light off of a non-magnetic sample (I generally used a pristine Si wafer) with polarizer and analyzer both crossed and aligned optical axes. In contrast, for a freshly grown sample, the Kerr parameters are not typically known, meaning the precise angles necessary to maximize S are unknown. However, S_{max} occurs at two sets of angles that straddle the extinction point of the instrument (Fig. 4.9). This means that practically, determining suitable operating angles involves finding the extinction

---

[2] Chapter 5 details the particular expressions of ϕ_A, ϕ_W that maximize S

point and then adjusting ϕ_A and ϕ_W a couple of degrees away from extinction until sufficiently high contrast is achieved. The critical relative waveplate and analyzer angles from extinction are proportional to $\sqrt{\gamma_D}$, meaning that a higher quality optical system featuring a low γ_D (or equivalently high extinction ratio) will result in not only a higher S_{max} (from eq. (4.3)), but also critical angles closer to extinction (Fig. 4.10). Additionally, S exhibits sharper peaks as $\gamma_D \rightarrow 0$, making it more difficult to locate a peak when scanning through waveplate and analyzer angles. The thin films examined in this work generally have $|\Phi_k| \approx 10 - 100$ millidegrees and our MOKE magnetometers have $\gamma_D \approx 10^{-2}$ to 10^{-4}, corresponding to critical angles ranging from a couple of degrees to less than 1° from extinction. With such narrow peaks, high angular resolution analyzer and waveplate rotation mounts are necessary to capitalize on the signal gains realized by minimizing depolarization.
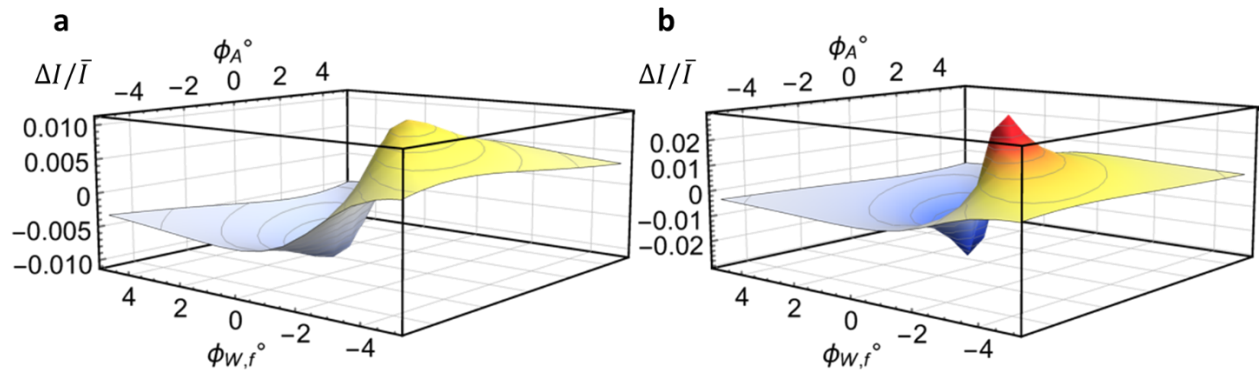
Figure 4.10: 3D calculated plots of S with $\theta_k = \epsilon_k = 0.007°$ and (a) $\gamma_D = 10^{-3}$ and (b) $\gamma_D = 10^{-4}$. The waveplate and analyzer angles are referenced with respect to the extinction point. Decreasing γ_D increasing S_{max}, narrows the peak width, and moves them closer to the origin (the extinction point).

Characterizing the noise, N, requires consideration of the detection scheme. In laser MOKE, there are multiple noise contributions including laser noise, dark noise, Johnson thermal noise, and shot noise which all have dependencies on intensity [62]. As a result, in laser systems, SNR is not maximized at the same critical angles that maximizes S. Because many of the significant noise terms are proportional to intensity, the maximum SNR in laser MOKE magnetometers tends to occur closer to extinction than S_{max}. In wide-field MOKE microscopy, many of these intensity-dependent noise contributions can be neglected. We define wide-field MOKE noise, to be the standard deviation of the intensity in a nominally uniform intensity region normalized by the mean intensity,

$$\sigma = \frac{\sigma_{SD}}{\bar{I}} \tag{4.4}$$

At low intensities, shot noise, σ_{shot}, becomes significant. Shot noise originates from discrete collection of incident photons (converted into electrons via a photocurrent) on the sensor,

$$\sigma_{shot} = \frac{1}{\sqrt{\frac{I_{DN}}{2^{B-1}} N_e}} \tag{4.5}$$

with I_{DN} the intensity digital number, i.e. the intensity readout according to the bit depth of the camera, B (e.g. 0 to 255 for an 8-bit camera), and N_e is the full well capacity (24000 e^- for the Pixelink camera, 15000 e^- for the Hamamatsu camera), or the maximum number of electrons that can be stored in a single CMOS or CCD image sensor. From (4.5) we see that the shot noise is minimized by selecting a sensor with a high full well capacity and by acquiring an image at high average intensity, which maximizes the number of photons collected.

In addition to shot noise, cameras also introduce discretization noise from analog-to-digital conversion. This is related to the bit-depth of the camera, B,

$$\sigma_{bit} = 2^{-B} \tag{4.6}$$

An 8-bit camera (the original camera installed on our wide-field MOKE) has $\sigma_{bit} \approx 0.004$, setting the floor for the minimum noise in a single acquisition. Increasing the bit depth to 16 (the bit-depth of the improved replacement camera on our wide-field MOKE) drastically lowers this floor to $\sigma_{bit} \approx 2 \times 10^{-5}$.
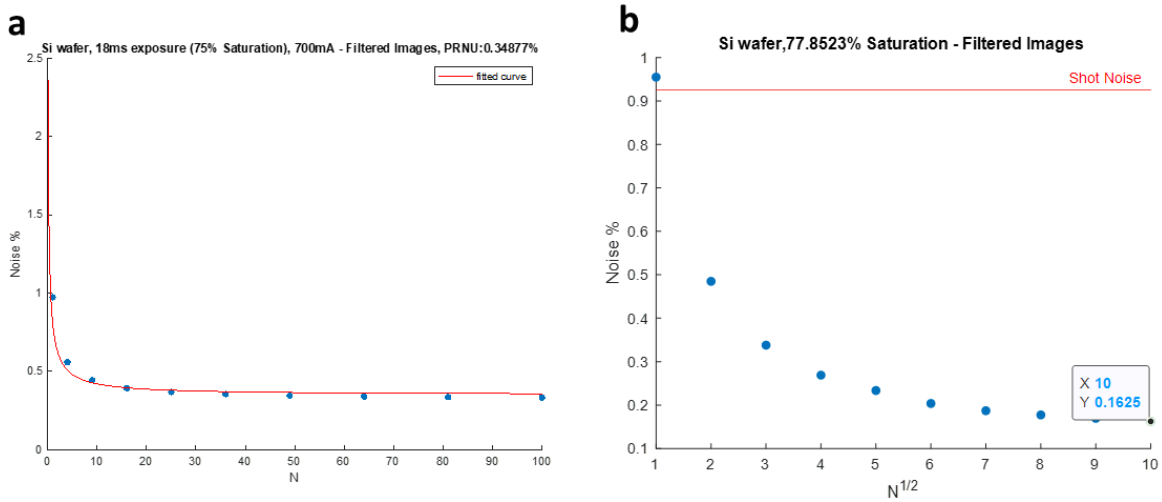
Figure 4.11: Wide-field MOKE microscopy noise plotted as a function of number of averaged images, N. (a) Pixelink 12-bit camera with Sony ICX285 sensor. Red line indicates noise fit based on three contributions: $\sigma_{shot}, \sigma_{bit}, \sigma_{PRNU}$. (b) Hamamatsu Orca Fusion 16-bit camera showing shot noise for a single frame (red line). Note the lower noise floor ($\sigma = 0.1625\%$) at $N = 100$.

Both σ_{shot} and σ_{bit} represent single frame noise floors and are reduced by averaging multiple frames together. We can represent the total noise based on these three contributions as,

$$\sigma = \sqrt{\frac{1}{N}(\sigma_{shot}^2 + \sigma_{bit}^2) + \sigma_{PRNU}^2} \qquad (4.7)$$

This is illustrated in Fig. 4.11. Eventually, averaging produces diminishing returns in noise reduction. At this point, the dominant noise contribution is from spatial variation in pixel

responsivity in the camera sensor, characterized by the camera's photoresponse non-uniformity (PRNU). The PRNU is a measure of the sensor's homogeneity and is the absolute noise floor for MOKE microscopy as the number of averaged frames, N, approaches infinity. The PRNU was the critical specification used to select an improved camera. The original Pixelink camera contained a Sony ICX285 sensor with an advertised PRNU of $< 2\%$. In contrast, the PRNU of the replacement Hamamatsu Orca Fusion is $< 0.06\%$.

Methods for Improving SNR in MOKE Microscopy

Combining the signal (4.3) and noise (4.7) gives the SNR of wide-field MOKE microscopy,

$$SNR = \frac{S}{\sigma} = \frac{\Delta I / \bar{I}}{\sqrt{\frac{1}{N}(\sigma_{shot}^2 + \sigma_{bit}^2) + \sigma_{PRNU}^2}} \tag{4.8}$$

As $N \to \infty$, we see that $SNR = \frac{S}{\sigma_{PRNU}}$, so that the maximum SNR occurs at S_{max} since σ_{PRNU} is independent of intensity. Thus, in applications where many frames can be averaged (or equivalently long exposure times are possible), PRNU is the single most important parameter for reducing noise in the measurement. As stated in the previous section, we replaced our Pixelink camera (PRNU of $< 2\%$) with a Hamamatsu Orca Fusion (PRNU $< 0.06\%$) which boasts the lowest PRNU of any camera on the market. Often, averaging $30 - 100$ frames is not always practical. Depending on the light source intensity, sample reflectivity, and extinction ratio, averaging 100 frames can take minutes. The optical setup must remain stable against mechanical perturbations and sample stage drift on the order of microns over that time to prevent artifacts from appearing in the contrast image. In cases where sample stability is an issue and shorter exposure times are required, the shot noise and bit noise become important.
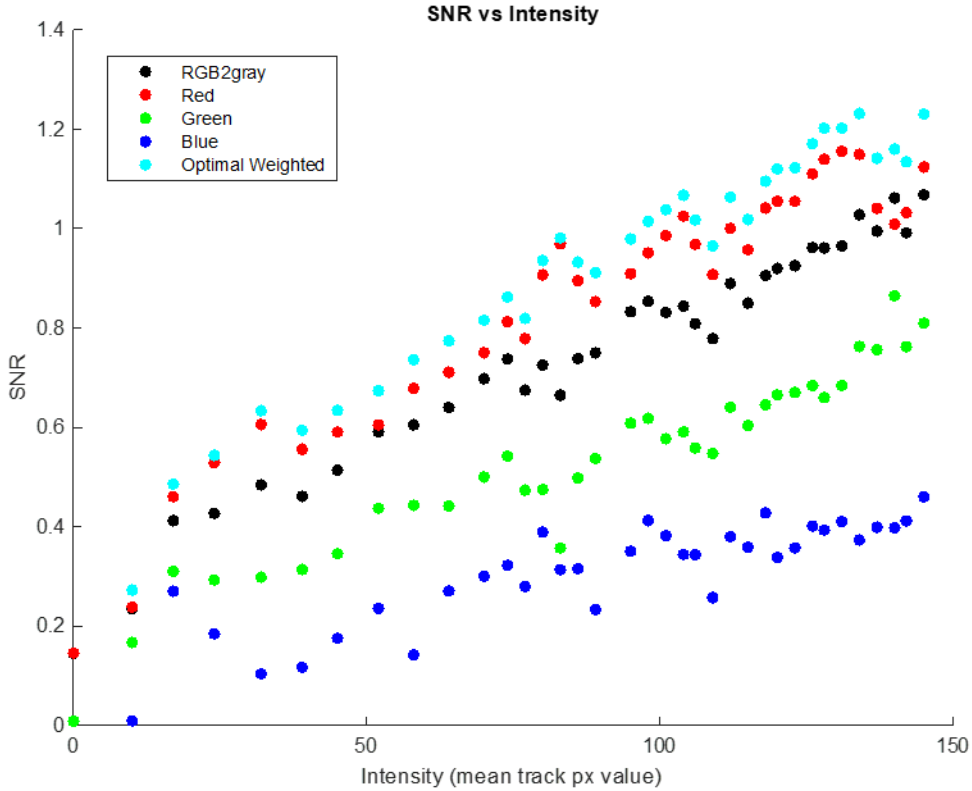
Figure 4.12: Measured SNR as a function of color channel including summed color channels (RGB2gray) and optimally weighted color channels. Data taken using Pixelink 8-bit camera with Sony ICX285 sensor on 8 nm $Gd_{0.35}Co_{0.65}$ magnetic racetrack with a white light source.

Expression (4.3) highlights the key engineering parameter necessary to maximize signal for a sample with set θ_k, ϵ_k: the extinction ratio. The extinction ratio is affected by just about every component of the optical system. Below are listed some design criteria and image acquisition strategies to maximize SNR in order of importance:

1. High-extinction optical components. The most important design component is selection of high-quality polarizers and quarter waveplate with specified extinction ratios of 10^4 or

greater at the light source wavelength combined with non-polarizing beamsplitters where necessary. One should note that in general, every optical component depolarizes the light to an extent. In our optimization of the wide-field MOKE, Huang and I noticed significant depolarization due to certain models of objective lenses, depending of the year of manufacture.

2. Use of low PRNU, monochromatic, flat spectral response camera and optical system. As previously stated, in the long-exposure/high N limit, the most significant noise contribution is the PRNU. However, the other significant selection criterion for cameras is their spectral response. Materials in general have variable $\Phi_k(\lambda)$, meaning that it is often desirable to change the light source wavelength to achieve higher SNR. This means camera sensors with equal efficiencies across the visible light spectrum are ideal. One should also note that the optical components are also rated for specific wavelengths of light. Even the nominally broad-spectrum polarizers used in our MOKE microscope exhibit different effective extinction ratios within the visible spectrum. This is shown in Fig. 4.12, where the SNR of red > green > blue light at a given intensity, despite GdCo having a constant Kerr angle over the visible spectrum [63]. Measurements of the extinction ratio in our system have revealed a > 2 × decrease in depolarization upon switching from a blue to red LED light source. Figure 4.12 also illustrates the importance of using monochromatic light over white light. The black data points are the naively summed color channels and exhibit a lower SNR than just the red channel despite containing 3x as many photons as the red channel. Only by optimally performing a weighted sum of the color channels (cyan points, found here using Lagrange multipliers) is a higher SNR achievable, and even then, the SNR gains are marginal at best.

3. Maximize light source intensity. If the optical system has been well-designed such that the extinction ratio > 3000, maximal SNR will occur within one or two degrees of the extinction point. As a result, the transmitted light intensity will be quite dim. At low light levels, camera sensors are more susceptible to shot noise and dark noise. This is evident from the linear increase in SNR with increasing intensity shown in Fig. 4.12. As a result, to minimize these contributions, the exposure time should be lengthened until 70 – 85% of the full well capacity has been achieved (as high a single frame intensity as possible without oversaturating the image). Depending on Φ_k, γ_D, and the LED intensity, this could require exposure times > 500 ms for a single frame acquisition, which may be impractically slow depending on the experiment and the mechanical stability of the microscope. In general, increasing the LED intensity only improves SNR and acquisition speed. If faster acquisition times are required, the image can be binned to sacrifice spatial resolution for higher contrast. Binning is the act of creating large pixels by summing multiple pixel's intensities together. For example, 2x2 binning combines four pixels into one, reducing spatial resolution by a factor of four. This can be done in post-processing or by adjusting the camera settings.

4. Ensure good light collimation. The analysis done to derive maximal signal assumes perfect optical components save for a depolarization factor to carry all non-idealities and assumes light rays traveling normal to the optical surfaces. In reality, the LED is not a point source but its own optical element with a corresponding numerical aperture (NA) that must be matched with the NA of the subsequent components in the light path. This requires the use of lenses to collimate diverging light and focus light onto the sample plane. Light that is not well-collimated will travel through optical components with at an angle. In the case of

a quarter waveplate the light path is particularly important as it determines the degree of phase delay between perpendicular components of the light, meaning an angled light ray could effectively transform a $\lambda/4$ waveplate into some non-standard order waveplate. In addition to proper lens selection, we have found that reducing the total length of the optical path by moving components closer together and adding an iris before the final lens into the camera to block oblique light has demonstrably improved the SNR of our wide-field MOKE microscope.
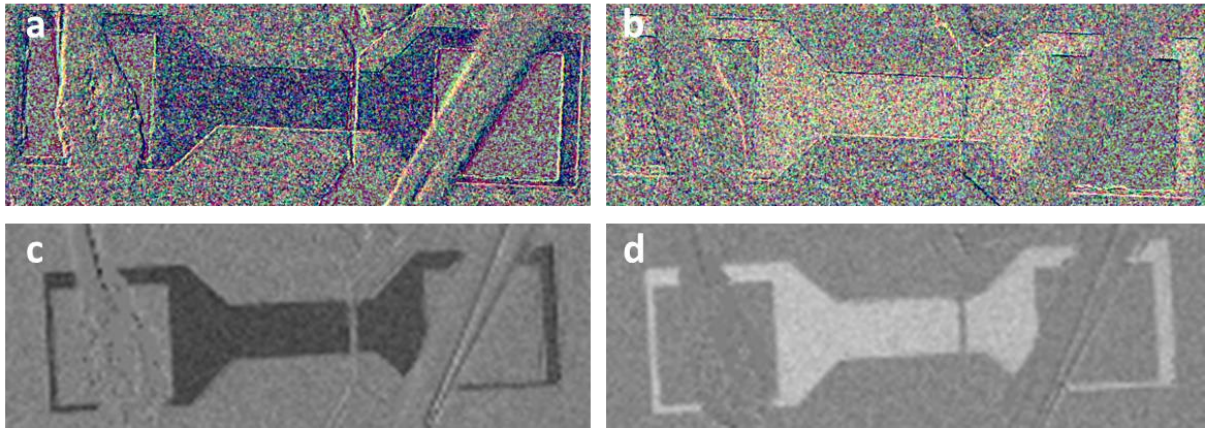
Figure 4.13: Wide-field MOKE microscope images of 8 nm $Gd_{0.35}Co_{0.65}$ magnetic racetrack showing the magnetic region in a down-magnetized state, (a) and (c), and an up-magnetized state, (b) and (d). (a) and (b) were taken prior to being upgraded and have an SNR < 1. (c) and (d) were taken after the upgrades and have SNR ~ 10.

Figure 4.13 shows the results of the improvements made to the wide-field MOKE microscope on a representative sample with a large Φ_k, 8 nm $Gd_{0.35}Co_{0.65}$. Figs. 4.13(a) and (b) show images taken before improvements were made to the system and with $G = 128$. The measured SNR of these images is ~0.8. Salt-and-pepper noise is evident in the images and Fig. 4.13(b) shows

particularly poor contrast compared to the background. In contrast, Figs. 4.13(c) and (d) show post-upgrade images of the same sample with $G = 10$ and a measured SNR ~ 10, an increase of over an order of magnitude. Despite the significantly smaller gain factor, the post-upgrade images exhibit remarkably clearer contrast in both magnetic states.

5 Measurement of Kerr Rotation and Ellipticity in Magnetic Thin Films by MOKE Magnetometry

5.1 Introduction

The magneto-optical Kerr effect (MOKE) describes the change in polarization orientation and ellipticity that occurs when linearly polarized incident light is reflected off a magnetic surface, proportional to the sample's magnetization, *M*. MOKE magnetometry takes advantage of this effect by casting the polarization change into a detectable intensity change via a quarter waveplate and analyzer. MOKE magnetometry is ubiquitous as a high-speed magnetic characterization technique with uses ranging from determination of coercive or exchange bias fields [64,65], dominant sublattice in ferrimagnets [66,67], and domain wall velocity [6,68,69].

The strength of the MOKE-induced polarization change is characterized by the complex Kerr angle, $\Phi_k = \theta_k + i\epsilon_k$. θ_k is the Kerr rotation angle, which describes the change in polarization orientation, and ϵ_k is the Kerr ellipticity angle. Φ_k has been found to influence other magneto-optic measurement techniques such as in Brillouin light scattering (BLS) for detection of magnons [70,71]. Consequently, a simple technique for Kerr angle determination is vitally important for a magnetic materials experimentalist.

Conventional techniques for measuring the Kerr angle typically rely on specialized ellipsometers containing photoelastic modulators [72,73] or require precise knowledge of the Fresnel reflection coefficients of the optical components in the setup [74]. In this paper, we demonstrate a simple technique for measuring the Kerr rotation and ellipticity angles using a standard MOKE magnetometer or MOKE microscope in polar and longitudinal geometries that relies solely on a single measure of the overall quality of the instrument, the depolarization

factor. In Section 5.2 we outline the measurement technique and investigate a few characteristic magnetic films in Section 5.3.

5.2 Normalized MOKE Signal Analytical Expression

5.2.1 Quarter Waveplate Fast Axis Parallel to Incident Polarization

There are three possible geometries for MOKE magnetometry measurements: polar, where M and light path are perpendicular to the sample surface; longitudinal, where M is parallel to the plane of reflection; and transverse, where M is perpendicular to the plane of reflection [75]. In the polar and longitudinal geometries, MOKE results in a transformation of incident linearly polarized light to elliptical, rotated light upon reflection off a magnetized sample, proportional to the sample's magnetization, M [62]. The subsequent analysis applies to these two geometries.

A schematic of a longitudinal MOKE magnetometer is shown in Fig. 5.1(a). The light is initially s-polarized by the input polarizer (P), reflects off the magnetic sample, proceeds through a quarter waveplate (W) and analyzer (A), and finally reaches the photodetector. This setup can be adapted to a polar geometry by reducing the incidence angle and adding a non-polarizing beamsplitter after P.
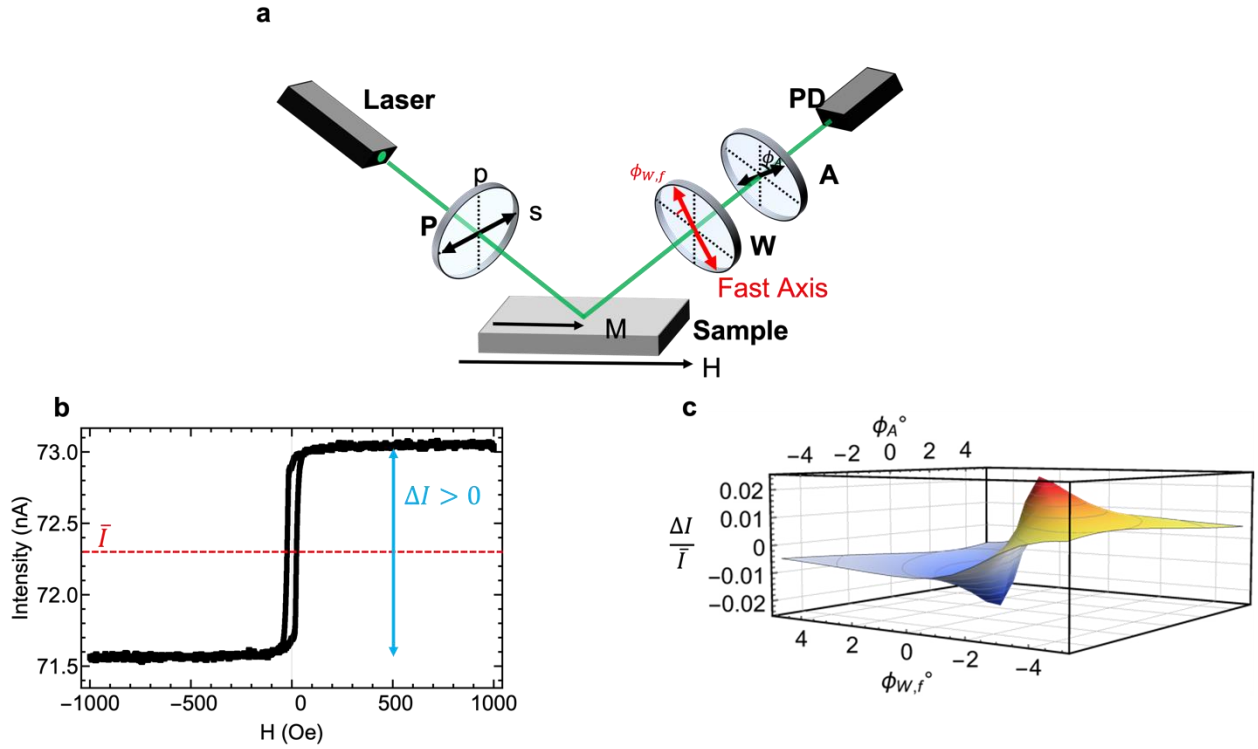
Figure 5.1: Longitudinal MOKE magnetometer and normalized MOKE signal model. (a) Schematic of longitudinal MOKE magnetometer showing the initial polarizer, P; quarter waveplate, W; analyzer, A; and photodetector, PD. The black double-headed arrows signify the optical axes of the polarizers. The red double-headed arrow is the fast axis of Q. (b) MOKE hysteresis loop of 25 nm $Gd_{0.33}Co_{0.67}$ showing the definitions of $\bar{I}$ and ΔI. (c) Predicted normalized MOKE intensity for a magnetic material with $\theta_k = \epsilon_k = 0.1°$ and $\gamma_D = 4 \times 10^{-4}$.

The polarization of a ray of light can be represented by a Jones vector: $\boldsymbol{E} = \begin{pmatrix} E_x \\ E_y \end{pmatrix}$, where E_x and E_y are the complex amplitudes of the electric field components of the ray of light in the horizontal and vertical directions, respectively. For the longitudinal geometry shown in Fig. 5.1(a), the horizontal and vertical components are taken to be s and p-polarized light, respectively. If the incident light is set to s-polarization, the light reflected off a sample is:

$$E_{sample} = \frac{1}{\sqrt{1+b^2}} \begin{pmatrix} 1 \\ be^{i\delta} \end{pmatrix} \tag{5.1}$$

with $b = \frac{E_y}{E_x}$ and $\delta = \delta_y - \delta_x$, the phase difference between orthogonal components. The quantities b and δ are related to the orientation angle, θ, and ellipticity angle, ϵ, by the equations [76,77]:

$$\tan 2\theta = \frac{2b\cos\delta}{1-b^2}, \qquad \sin 2\epsilon = \frac{2b\sin\delta}{1+b^2} \tag{5.2}$$

For small θ and ϵ, this reduces to:

$$b = \sqrt{\theta^2 + \epsilon^2}, \qquad \delta = \arctan\frac{\epsilon}{\theta} \tag{5.3}$$

The Jones vector of the light after passing through W and A is given by the product of the Jones matrices:

$$E_{out} = \begin{pmatrix} E_{out,x} \\ E_{out,y} \end{pmatrix} = R^{-1}(\phi_{A,abs})\, P_y\, R(\phi_{A,abs})\, R^{-1}(\phi_{W,f,abs})\, W_x\, R(\phi_{W,f,abs})\, E_{sample} \tag{5.4}$$

$$R(\phi) = \begin{pmatrix} \cos\phi & \sin\phi \\ -\sin\phi & \cos\phi \end{pmatrix}, \qquad P_y = \begin{pmatrix} 0 & 0 \\ 0 & 1 \end{pmatrix}, \qquad W_x = \begin{pmatrix} 1 & 0 \\ 0 & i \end{pmatrix}$$

Here, $R(\phi)$ is the counterclockwise (CCW) rotation matrix, P_y is a vertically oriented polarizer, and W_x is a quarter waveplate with a horizontal fast axis, parallel to the incident polarization. $\phi_{A,abs}$ and $\phi_{W,f,abs}$ are the CCW angles of the analyzer from vertical (p-axis) and the quarter waveplate fast axis from horizontal (s-axis) as indicated in Fig. 5.1(a). The intensity at the photodetector is then the dot-product of E_{out} with its complex conjugate [76]:

$$I = E_{out,x}E_{out,x}^* + E_{out,y}E_{out,y}^* \tag{5.5}$$

$$I = \frac{1}{4}\Big[(\theta^2 + \epsilon^2 - 1)\cos 2\phi_{A,abs} + (\theta^2 + \epsilon^2 - 1)\cos\big(2(\phi_{A,abs} - 2\phi_{W,f,abs})\big)$$

$$+ 2(1 + \theta^2 + \epsilon^2) + 2\epsilon\sin\big(2(\phi_{A,abs} - \phi_{W,f,abs})\big)$$

$$- 2\theta\cos\big(2(\phi_{A,abs} - \phi_{W,f,abs})\big)\sin 2\phi_{W,f,abs}\Big]$$

Appling a small-angle approximation for ϕ_A and $\phi_{W,f}$ (since MOKE magnetometers operate near extinction) and removing terms above second order gives the approximate intensity:

$$I(\theta,\epsilon) \approx \theta^2 + \epsilon^2 + 2\epsilon\phi_{A,abs} - 2\big(\theta + \epsilon + \phi_{A,abs}\big) + \phi_{A,abs}^2 + 2\phi_{W,f,abs}^2 + \gamma_D \qquad (5.6)$$

where we have added a depolarization factor, γ_D, to account for the limitations of physical optical components, following [62]. The depolarization factor is a measure of the quality of the optical system and is equivalent to the reciprocal of the extinction ratio. θ and ϵ describe the total rotation and ellipticity imparted to light reflected off the sample and can be separated into a Kerr component, θ_k or ϵ_k, and non-Kerr component, θ_0 or ϵ_0,

$$\theta = \theta_k + \theta_0, \qquad \epsilon = \epsilon_k + \epsilon_0 \qquad (5.7)$$

Only the Kerr components, θ_k and ϵ_k, change sign under a reversal in M, resulting in the MOKE signal, ΔI,

$$\Delta I = I_{M^+} - I_{M^-} = I(\theta_k + \theta_0, \epsilon_k + \epsilon_0) - I(-\theta_k + \theta_0, -\epsilon_k + \epsilon_0) \qquad (5.8a)$$

$$\Delta I = 4\big(\theta_0\theta_k + \epsilon_k(\epsilon_0 + \phi_{A,abs}) - (\epsilon_k + \theta_k)\phi_{W,f,abs}\big) \qquad (5.8b)$$

The average intensity, $\bar{I}$, is:

$$\bar{I} = \frac{1}{2}(I_{M^+} + I_{M^-}) = \frac{1}{2}[I(\theta_k + \theta_0, \epsilon_k + \epsilon_0) - I(-\theta_k + \theta_0, -\epsilon_k + \epsilon_0)] \qquad (5.9a)$$

$$\bar{I} = \theta_k^2 + \epsilon_k^2 + \theta_0^2 + \big(\epsilon_0 + \phi_{A,abs}\big)^2 - 2\big(\theta_0 + \epsilon_0 + \phi_{A,abs}\big)\phi_{W,f,abs} + 2\phi_{W,f,abs}^2 + \gamma_D \qquad (5.9b)$$

A MOKE hysteresis loop defining ΔI and $\bar{I}$ is shown in Fig. 5.1(b).

Precisely aligning optical axes of the two polarizers and waveplate requires removing those components from the magnetometer and is experimentally tedious as a result. In a MOKE magnetometer, it is generally more convenient to locate extinction while a magnetic sample of interest is inserted. Using (5.9b), the analyzer and waveplate extinction angles are $\phi_{A,ext} = \theta_0 - \epsilon_0$ and $\phi_{W,f,ext} = \theta_0$. Thus, the non-Kerr rotation and ellipticity only add an offset to the analyzer and waveplate angles. Defining angles relative to extinction, $\phi_A = \phi_{A,abs} - \phi_{A,ext}$ and $\phi_{W,f} = \phi_{W,f,abs} - \phi_{W,f,ext}$ and combining (5.8b) and (5.9b) gives the normalized MOKE signal, $\frac{\Delta I}{\bar{I}}$:

$$\frac{\Delta I}{\bar{I}} = \frac{4\left(\epsilon_k \phi_A - (\epsilon_k + \theta_k)\,\phi_{W,f}\right)}{\theta_k^2 + \epsilon_k^2 - 2\phi_A \phi_{W,f} + \phi_A^2 + 2\phi_{W,f}^2 + \gamma_D} \tag{5.10}$$

Figure 5.1(c) shows the normalized MOKE intensity near extinction for $\theta_k = \epsilon_k = 0.1°$ and $\gamma_D = 4 \times 10^{-4}$. The extrema straddle extinction ($\phi_A = \phi_{W,f} = 0$) and flip polarity moving across extinction. The magnitude of the extrema and their corresponding locations are:

$$\left(\frac{\Delta I}{\bar{I}}\right)_{crit} = \begin{cases} \pm\dfrac{2|\Phi_k|}{\sqrt{\gamma_D}}, \theta_k > \epsilon_k \ or \ \theta_k = \epsilon_k < 0 \\[3mm] \mp\dfrac{2|\Phi_k|}{\sqrt{\gamma_D}}, \theta_k < \epsilon_k \ or \ \theta_k = \epsilon_k > 0 \end{cases} \tag{5.11a}$$

$$\phi_{A,f,crit} = \mp|\epsilon_k - \theta_k|\frac{\sqrt{\gamma_D}}{|\Phi_k|}, \qquad \phi_{W,f,crit} = \pm\frac{\epsilon_k - \theta_k}{|\epsilon_k - \theta_k|}\theta_k\frac{\sqrt{\gamma_D}}{|\Phi_k|} \tag{5.11b}$$

where $\Phi_k = \theta_k + i\epsilon_k$ is the complex Kerr angle.

From (5.11a), the magnitude of the normalized MOKE signal peak is proportional to $|\Phi_k|$ and inversely proportional to the depolarization. In wide-field MOKE microscopy the dominant noise contribution is spatial pixel variation of the detecting camera, resulting in a normalized MOKE signal directly proportional to the signal-to-noise ratio. As a result, minimizing depolarization in a MOKE microscope is critical to imaging samples with low Kerr angles. In

contrast, laser MOKE magnetometry is in general not directly proportional to the normalized MOKE signal due to intensity dependent noise contributions such as shot noise [62,78,79].

Figures 5.2(a)-(c) show the normalized MOKE signal with $|\Phi_k| = 0.1°$ and $\gamma_D = 4 \times 10^{-4}$ for various combinations of Kerr rotation and ellipticity. Without Kerr ellipticity, the $\Delta I / \bar{I}$ peaks occur along a +45° line with the ϕ_A axis, meaning equal rotations of waveplate and analyzer from extinction are required for maximum signal. However, without Kerr rotation, the extrema fall along the ϕ_A axis. When both Kerr rotation and ellipticity equally contribute, a 90° line is made with the ϕ_A axis. We can define the angle with the ϕ_A axis as ψ_f (shown in Fig. 5.2(a)) and calculate the angles as a function of θ_k and ϵ_k:

$$\tan \psi_f = \frac{\phi_{W,f,crit}}{\phi_{A,f,crit}} = \frac{-\theta_k}{\epsilon_k - \theta_k} \tag{5.12}$$

From (5.12), the angle of the $\Delta I / \bar{I}$ extrema determines the ratio of θ_k to ϵ_k. Combining this result with the magnitude of the $\Delta I / \bar{I}$ peak, given in (5.11a) and (5.11b), allows for the unique determination of magnitude and sign of θ_k and ϵ_k.
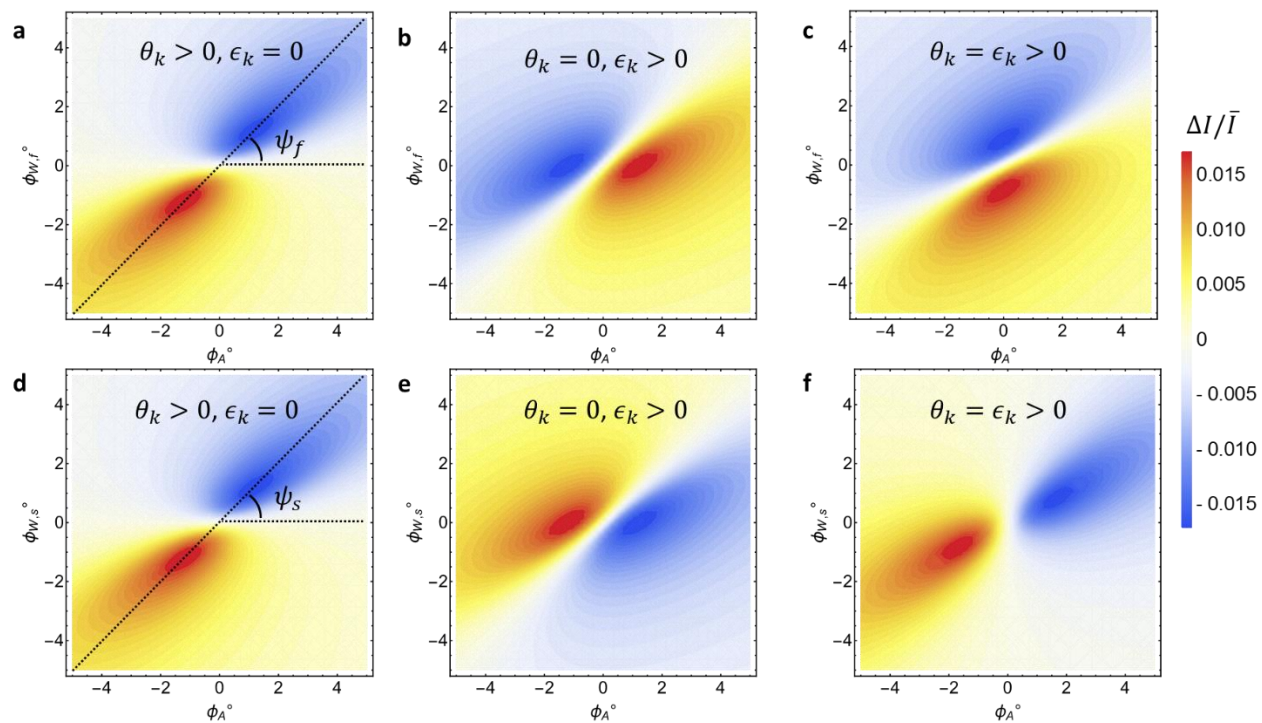
Figure 5.2: Normalized MOKE signal for different Kerr rotation and ellipticity values. (a)-(c)

Normalized MOKE signal with waveplate fast axis parallel to incident polarization. (d)-(f)

Normalized MOKE signal with waveplate slow axis parallel to incident polarization.

5.2.2 Quarter Waveplate Slow Axis Parallel to Incident Polarization

The average intensity, $\bar{I}$, relative to extinction is identical for a quarter waveplate regardless of whether the fast or slow axis parallel to the incident polarization direction. As a result, the fast and slow axes can easily be mistaken for one another, resulting in a flipped ϵ_k sign. The fast axis can be verified using the same components as a MOKE magnetometer, following [80]. Using the same methods as described in the previous section, the normalized MOKE intensity with a waveplate slow axis parallel to incident polarization is (relative to extinction):

$$\frac{\Delta I}{\bar{I}} = \frac{-4\left(\epsilon_k \phi_A + (\theta_k - \epsilon_k)\, \phi_{W,s}\right)}{\theta_k^2 + \epsilon_k^2 - 2\phi_A \phi_{W,s} + \phi_A^2 + 2\phi_{W,s}^2 + \gamma_D} \tag{5.13}$$

The extrema are:

$$\left(\frac{\Delta I}{\bar{I}}\right)_{crit} = \pm \frac{2|\Phi_k|}{\sqrt{\gamma_D}} \frac{\theta_k + \epsilon_k}{|\theta_k + \epsilon_k|} \tag{5.14a}$$

$$\phi_{A,s,crit} = \mp |\epsilon_k + \theta_k| \frac{\sqrt{\gamma_D}}{|\Phi_k|}, \qquad \phi_{W,s,crit} = \mp \frac{\epsilon_k + \theta_k}{|\epsilon_k + \theta_k|} \theta_k \frac{\sqrt{\gamma_D}}{|\Phi_k|} \tag{5.14b}$$

And the angle with the ϕ_A axis is:

$$\tan \psi_s = \frac{\phi_{W,s,crit}}{\phi_{A,s,crit}} = \frac{\theta_k}{\epsilon_k + \theta_k} \tag{5.15}$$

The differences between the two waveplate orientations is shown in Fig. 5.2. With no Kerr ellipticity, the normalized MOKE signal is independent of waveplate orientation (Figs. 5.2(a) and (d)), whereas with no Kerr rotation, the two orientations result in opposite MOKE signal polarities (Figs. 5.2(b) and (e)). Finally, mixed contributions to the Kerr angle result in qualitatively different plots for each orientation (Figs. 5.2(c) and (f)). Despite these qualitative differences, however, mistaking the waveplate optical axes only results in a flipped Kerr ellipticity; the magnitudes (dependent on the peak height) and sign of the Kerr rotation are unaffected.

5.3 MOKE Magnetometry Measurements

The Kerr angles of BiYIG, GdCo, and TbCo were measured using the expressions in Section 5.2. The BiYIG sample was prepared by pulsed laser deposition. The remaining samples were grown on Si by D.C. magnetron sputter deposition with layer structure Ta(4)/Pt(4)/GdCo or TbCo/Ta(4)/Pt(2), with the values in parenthesis representing the thickness in nanometers. Samples of 50 nm BiYIG, 25 nm $Gd_{0.33}Co_{0.67}$, and 6 nm $Tb_{0.12}Co_{0.88}$ with in-plane anisotropy were analyzed using a longitudinal MOKE magnetometer with a 45˚ incidence angle and incident s-polarized 532-nm light. The quarter waveplate was oriented with its slow axis along the s-pole, parallel to the incident light. Magnetic MOKE hysteresis loops were collected at various combinations of ϕ_A, $\phi_{W,s}$ and the normalized MOKE signal was recorded in accordance with Fig. 5.1(b). The results of these measurements are shown in Fig. 5.3. The similarity between Figs. 5.3(a) and 5.2(e) suggest that the BiYIG is dominated by Kerr ellipticity, whereas the 25-nm $Gd_{0.33}Co_{0.67}$ and 6-nm $Tb_{0.12}Co_{0.88}$ have $\Delta I/\bar{I}$ plots indicative of substantial contributions from both Kerr rotation and ellipticity. These data were then fitted to (5.13) to determine θ_k and ϵ_k quantitatively. The depolarization factor was measured by inserting a bare Si wafer into the magnetometer, setting the waveplate and analyzer angles to extinction, and measuring the resultant intensity as a function of analyzer angle. These data were then fitted to the function, $I = I_{ext} + I_0 \sin^2 \phi_A$. The depolarization factor was then calculated from $\gamma_D = \frac{I_{ext}}{I_0} = (4.5 \pm 0.8) \times 10^{-4}$. While fitting the data to (5.13), γ_D was allowed to vary within the measured uncertainty of the value. The contour lines in Fig. 3 show the agreement between the fitted model with the measured MOKE signal. The values of the parameters extracted from the fit are shown in Table 5.1.
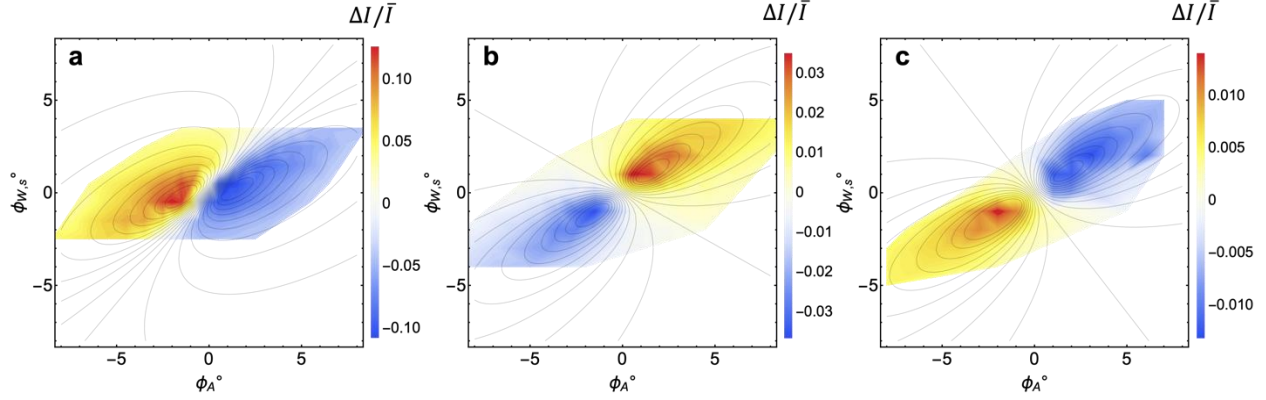
Fig 5.3: Normalized MOKE signal for (a) 50 nm BiYIG, (b) 25 nm $Gd_{0.33}Co_{0.67}$, and (c) 6 nm $Tb_{0.12}Co_{0.88}$ with quarter waveplate slow axis parallel to incident polarization. Contour lines show fitted function.

A 3 nm Gd_xCo_{1-x} composition series of samples with perpendicular magnetic anisotropy (PMA) was analyzed using a polar wide-field MOKE microscope with 650 nm light. The Kerr angle of thin film GdCo is of particular importance due its recent prevalence in domain wall motion [5,6] , voltage gating [66], and Brillouin light scattering experiments [81], all of which depend on the GdCo Kerr angle. In these ferrimagnetic films, the Kerr signal primarily originates from the Co sublattice, making MOKE magnetometry a useful tool for determining the dominant sublattice [45]. A representative MOKE signal plot is presented in Fig. 5.4(a) and the resulting Kerr angles as a function of Gd atomic fraction are plotted in Fig. 5.4(b) along with best fit lines for each Kerr component. We observe a linear decrease in $|\Phi_k|$, $|\theta_k|$, and $|\epsilon_k|$ with increasing Gd atomic fraction, consistent with previous reports in thicker films of rare-earth transition metal alloys but about 10x smaller in magnitude [82,83]. The reduced value is likely due to the difference in thickness (3 nm versus 100 – 300 nm) and to the capping layer's attenuating effect in our samples [71]. The measured GdCo composition range was limited to its PMA range. In general, the polar Kerr angle is significantly larger than its longitudinal counterpart [71]. As a result, to

investigate whether the linear trend continued to pure Co, we measured an ultrathin 0.8 nm Co sample deposited on Pt exhibiting PMA and determined the polar Kerr angle: $\theta_k = -(33.3 \pm 1.1) \times 10^{-3}$ °, $\epsilon_k = (14.9 \pm 0.6) \times 10^{-3}$ °. In samples under 30 nm, the Kerr rotation and ellipticity increase linearly with magnetic layer thickness [84]. Scaling up these values to 3 nm gives $\theta_{k,3nm} = -(125 \pm 4) \times 10^{-3}$ ° and $\epsilon_{k,3nm} = (56 \pm 2) \times 10^{-3}$ °. When compared to the extrapolated linear fit at $x = 0$ ($\theta_{k,fit} = -(50 \pm 8) \times 10^{-3}$ °, $\epsilon_{k,fit} = (42 \pm 10) \times 10^{-3}$ °), we find reasonable agreement between the linear fit and measured Kerr ellipticity, but a significant underestimate of the Kerr rotation compared to the measured value. This suggests that the initial addition of Gd to Co may non-linearly reduce the Kerr rotation before settling into a linear dependence at higher Gd concentrations. A previous report has found the Kerr rotation to be directly proportional to the Co sublattice magnetization, M_{Co} [82]. M_{Co} is expected to be approximately linear over the composition range in Fig. 5.4(b) but drop steeply at low Gd concentrations due to the large atomic volume of Gd relative to Co, which may explain the high measured Kerr values of pure Co.

Table 5.1: Measured longitudinal Kerr angles of various films measured via MOKE magnetometry

	θ_k° $(\times 10^{-3})$	ϵ_k° $(\times 10^{-3})$	$\lvert\Phi_k\rvert$° $(\times 10^{-3})$	γ_D $(\times 10^{-4})$
50 nm BiYIG	11.5 ± 0.9	72 ± 1.3	73.0 ± 1.3	4.2 ± 0.2
25 nm Gd$_{0.33}$Co$_{0.67}$	-18.1 ± 0.3	-6.5 ± 0.2	19.2 ± 0.3	3.7 ± 0.2
6 nm Tb$_{0.12}$Co$_{0.88}$	7.1 ± 0.3	4.0 ± 0.2	8.1 ± 0.3	4.5 ± 0.6

5.4 Conclusion

The Kerr rotation and ellipticity can be measured using a standard MOKE magnetometer without augmentation. The ratio of Kerr rotation to ellipticity is easily determined by recording the waveplate and analyzer angles at normalized MOKE signal maxima. Combined with the magnitude and sign of the normalized MOKE intensity, this allows for accurate calculation of the sign and value of the Kerr angle. We demonstrate this technique's applicability to both longitudinal and polar configurations. Finally, we find that the complex Kerr angle of thin film GdCo decreases linearly with increasing Gd content. In light of previous reports connecting the measured Kerr angle to M_{Co} in rare-earth transition-metal alloys, Kerr angle extraction may be an accessible method for determining the relative sublattice magnetizations in ferrimagnetic materials.
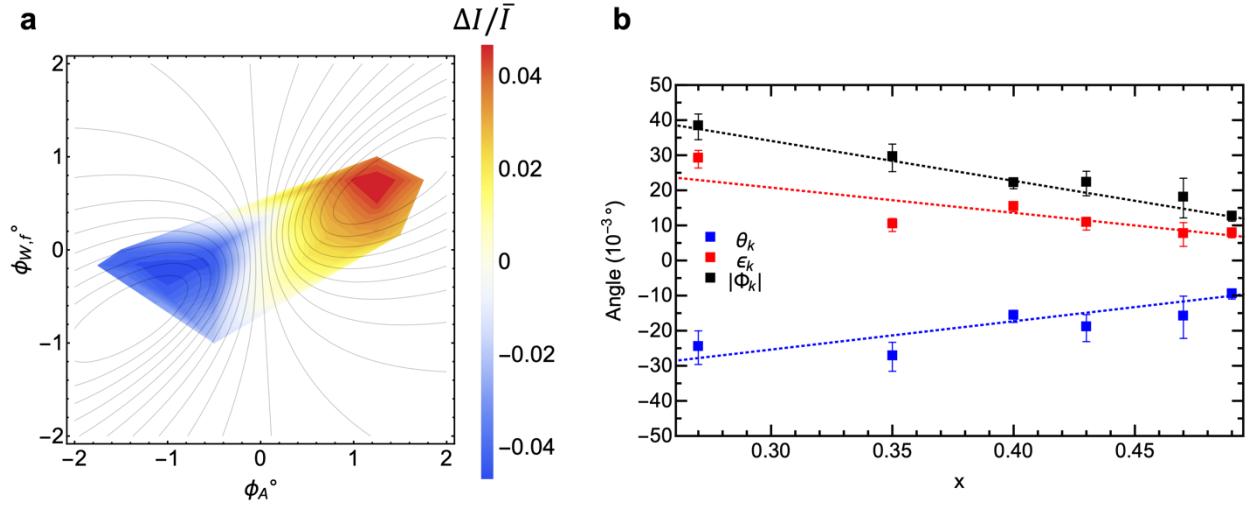
Figure 5.4: Kerr data for 3 nm GdCo, measured by polar MOKE microscopy. (a) Normalized MOKE signal of 3 nm $Gd_{0.4}Co_{0.6}$ with quarter waveplate fast axis parallel to incident polarization. Contour lines show fitted function. (b) Polar Kerr rotation, θ_k; ellipticity, ϵ_k; and complex Kerr angle magnitude, $|\Phi_k|$, as a function of Gd atomic fraction, x.

6 Thickness and composition effects on atomic moments and magnetic compensation point in rare-earth transition-metal thin films[3]

The previous chapter investigated the optical properties of magnetic thin films and found that the magnitude of the Kerr rotation and ellipticity decreases linearly with increasing Gd concentration in 3-nm GdCo heterostructures. Based on previous studies of thicker GdCo films, this suggests a linear decrease in M_{Co} over this composition range. In this chapter, we investigate the magnetic properties of rare-earth transition-metal thin films as a function of rare-earth concentration and film thickness. Using x-ray magnetic circular dichroism, we probe the spin and orbital angular momenta of each sublattice in GdCo and TbCo individually and find an unexpected, monotonic decrease in rare-earth and transition-metal atomic moment with increasing rare-earth content. We additionally posit the existence of a rare-earth dead layer that results in a substantial shift in magnetic compensation composition as the thickness of the ferrimagnetic layer is reduced below 10 nm.

6.1 Introduction

Rare-earth transition-metal (RE-TM) amorphous alloys have regained prominence in recent years due to their utility in spintronic devices. Novel spin transport phenomena such as ultrafast domain wall motion [5,6,68,85], stable room temperature skyrmion generation [6,86], all-

---

[3] This chapter is adapted from an accepted publication in Physical Review B [122] and is presented here in a mostly unaltered form.

optical switching [87,88], and field-free spin-orbit torque switching [89,90] have all been observed in RE-TM heterostructures, facilitated by their unique properties. Many of these properties are due to the antiferromagnetic coupling between the RE and TM sublattices, resulting in net ferrimagnetic behavior. The ferrimagnetic nature of RE-TM alloys means that their magnetization and net spin can be tuned by varying the temperature (T) and the compositions of the RE and TM sublattices, allowing for fine control of a variety of dependent magnetic properties such as anisotropy and compensation temperatures, with critical consequences on static and dynamic behavior.

Generally, RE-TM alloys are modelled as a pair of antiferromagnetically coupled sublattices such that the net saturation magnetization is given by $M_S = |M_{RE} - M_{TM}|$. This model allows one to estimate net properties such as the effective g-factor of the material or the T-dependent saturation magnetization [91,92]. In practice, the sublattice magnetizations are not known individually, or their values are assumed based on the pure elemental magnetizations scaled by their volume fractions in the alloy.

In this work, we investigate the variation of magnetic moment in GdCo and TbCo as a function of RE composition (x) and thickness (t). We find that the compensation composition undergoes a systematic shift to higher RE concentrations with decreasing t as the RE-TM film drops below 10 nm. We use x-ray magnetic circular dichroism (XMCD) to probe the atomic magnetic properties of each element independently as a function of x and observe a clear decrease in both RE and TM moment with increasing x at room temperature. We additionally observe a significant variation in atomic g-factors as a function of x. Finally, we model the M_S as a function of t and x for RE-TM alloys by inclusion of a RE dead layer that shifts the compensation composition of thin films.
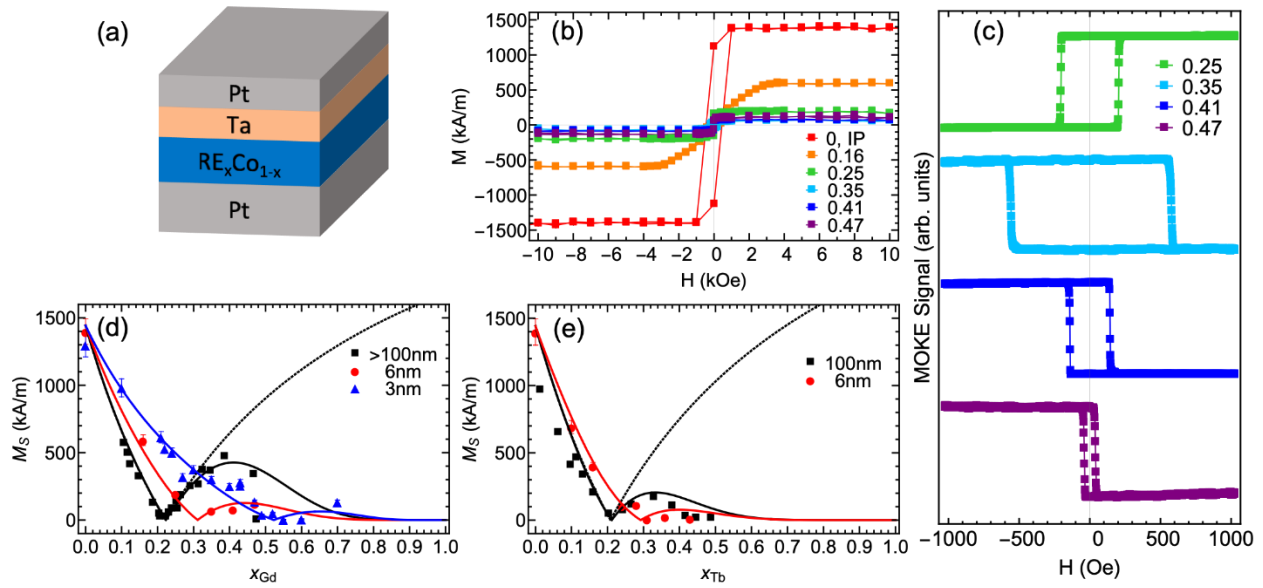
Figure 6.1: VSM and MOKE data of GdCo and TbCo films. (a) Layer structure of RE-Co films grown by sputter deposition. (b) VSM hysteresis loops of 6 nm GdCo films used to determine saturation magnetization M_s. All loops were measured in an out-of-plane configuration except for pure Co (red). The legend refers to Gd atomic fraction. (c) MOKE loops of 6 nm GdCo with PMA. Right-facing loop (green) is Co-dominant and left-facing loops (cyan, blue, purple) are Gd-dominated. (d) GdCo M_s data at room temperature. Solid curves are based on a combined environment plus Gd dead layer model (see text). Dotted line is the predicted M_s assuming constant atomic Gd, Co moments across composition. Black squares are from Ref. [93]. (e) TbCo M_s data at room temperature. Black squares are from Ref. [83].

6.2 Experimental Methods

Films of Ta(4)/Pt(4)/Gd$_x$Co$_{1-x}$(t)/Ta(4)/Pt(2) and Ta(4)/Pt(4)//Tb$_x$Co$_{1-x}$(6)/Ta(3)//Ta(3)/Pt(2) were grown by DC magnetron sputtering (numbers in parenthesis are thickness in nm and x is the RE atomic fraction; see Fig. 6.1(a)) on thermally oxidized Si wafers with $x = 0$ to 0.7 and $t = 3$, 6 nm. The TbCo films were grown in three steps (with vacuum breaks indicated by double slashes) due to a sputter gun limitation. The GdCo and TbCo layers were grown by co-sputtering Gd or Tb with Co. An Ar pressure of 3 mTorr with a background pressure $< 2 \times 10^{-7}$ Torr was used during deposition. Layer thicknesses and nominal alloy atomic fractions were determined from sputtering rates calibrated using x-ray reflectometry. The atomic compositions of RE-Co layers were calculated using the ratio of the RE and Co deposition rates normalized by their molar masses and bulk densities with ~1% uncertainty. The compositions were controlled by controlling the RE gun current to tune the RE deposition rate relative to the Co rate. The films' bottom Pt layer was chosen to replicate the Pt/GdCo multilayers used for current-induced domain wall motion and room-temperature magnetic skyrmion generation [5,6,24,68]. The top Ta/Pt layer was added to prevent sample oxidation. For each sample, the M_s was measured by acquiring an out-of-plane hysteresis loop signal using a vibrating sample magnetometer (VSM) and then subtracting the linear diamagnetic Si substrate background signal (Fig. 6.1(b)). Polar magnetooptical Kerr Effect (MOKE) hysteresis loops were taken on samples with perpendicular magnetic anisotropy (PMA) using a 660 nm laser. In the visible regime, the Kerr rotation is dominated by the Co sublattice, allowing one to determine the magnetically dominant sublattice via the polarity of a MOKE loop [45]. Measured MOKE loops for 6 nm GdCo are shown in Fig. 6.1(c). The polarity change from $x = 0.25 - 0.35$ indicates the samples shifting from Co-dominated to Gd-dominated with increasing Gd content.

Figures 6.1(d) and (e) show measured and previously reported M_s values for GdCo and TbCo films as a function of RE content at room temperature. The precise thickness of the GdCo measured in Ref. [93] (Fig. 6.1(d), black squares) was not reported, however, based on the stated deposition rate (50 nm/min) and thickness of the protective capping layer (30 – 100 nm), we conclude the thickness to be at least 100 nm. The node position of the solid curves, indicating the magnetic compensation composition, was verified by confirming a polarity change in the MOKE hysteresis loops for the grown films (6 nm and below). In both GdCo and TbCo films, the magnetic compensation composition of thick films is $x \approx 0.22$. As t decreases, the compensation composition shifts to higher x, shifting to $x \approx 0.3$ for 6 nm films and $x \approx 0.52$ for 3 nm films.

Proximity-induced magnetism (PIM) can exist at Pt/Co interfaces and could in principle cause the apparent magnetic compensation point to shift. An unaccounted-for magnetic Pt layer would lead to an over- (under-) estimation of the measured RE-Co M_s ($M_{s,meas}$) if it were oriented parallel (antiparallel) to the net magnetization. This effect can be quantified as

$$\frac{M_{s,meas}}{M_{s,RE-Co}} = 1 + \frac{M_{s,Pt}t_{Pt}}{M_{s,RE-Co}t} \tag{6.1}$$

where $M_{s,RE-Co}$ and $M_{s,Pt}$ are the true M_s of RE-Co and Pt, respectively, $M_{s,Pt}t_{Pt}$ is the areal moment density of the magnetic Pt, and the rightmost term quantifies the fractional overestimate. Given the previously reported effective proximity moment of ~1 μ_B per interfacial Pt atom [94], we calculate $M_{s,Pt}t_{Pt} = 130$ μA, which would shift x_{comp} by only ~1 at.% RE for $t = 3$ nm. We conclude that PIM cannot account for the ~30 at.% Gd shift in x_{comp} observed in Fig. 6.1(d) at low t. Instead, the shift in x_{comp} implies a decrease in the ratio of the effective RE magnetic moment relative to the Co magnetic moment with decreasing t.
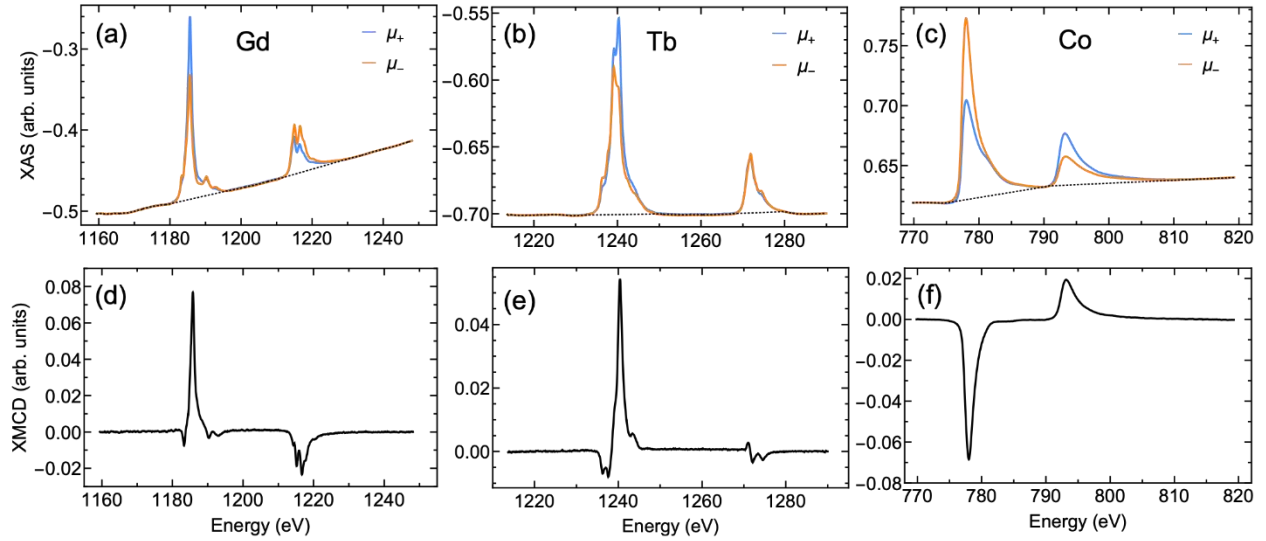
Figure 6.2: Representative XAS and XMCD spectra of perpendicularly saturated 6 nm GdCo and TbCo. Top plots (a)-(c): X-ray absorption spectra at Gd $M_{5,4}$, Tb $M_{5,4}$, and Co $L_{3,2}$ edges using positive (μ_+, blue) and negative (μ_-, orange) circularly polarized light. Black dotted line is interpolated background function used for calculation of r (see text). Bottom plots (d)-(f): XMCD signal derived from $\mu_+ - \mu_-$. Spectra (a), (c), (d), (f) are of 6 nm $Gd_{0.25}Co_{0.75}$. Spectra (b), (e) are of 6 nm $Tb_{0.28}Co_{0.72}$.

To quantify the sublattice magnetic moments, we conducted XMCD measurements on 6 nm GdCo and TbCo composition series at 2 K and 300 K. Previous studies have used XMCD to probe the magnetic properties of each sublattice in RE-TM films [38,66,95–100], however a comprehensive study of sublattice magnetic moments over a wide range of compositions has yet to be reported. X-ray absorption spectroscopy (XAS) measurements were taken in a transmission geometry at the BOREAS beamline of the ALBA synchrotron using a 90% circularly polarized x-ray beam produced by an Apple-II-type undulator. The incident beam was normalized using a gold mesh. A field of 15 kOe was selected to ensure sample saturation. Four spectra were collected at

each helicity at the Gd or Tb $M_{5,4}$ and Co $L_{3,2}$ edges. The XAS spectra of each element were aligned to have consistent pre- and post-edge intensities, and the best-fit line of the pre- and post-edge regions was subtracted from the raw spectra to yield the corrected XAS spectra in Figs. 6.2(a)-(c). The XMCD signal was then calculated from the difference of the aligned XAS spectra at each helicity (Figs. 6.2(d)-(f)). The remaining XAS background was removed for determination of r by subtracting the linear interpolation of off-peak intervals from the raw spectra for each helicity. The off-peak intervals for interpolation were defined as $E < 1180$ eV, 1196 eV $< E < 1210$ eV, and $E > 1230$ eV for Gd; $E < 1232$ eV, 1250 eV $< E < 1268$ eV, and $E > 1280$ eV for Tb; and $E < 775$ eV, 790 eV $< E < 790.8$ eV, and $E > 815$ eV for Co. The background functions are plotted in Figs. 6.2(a)-(c).

The averaged orbital (m_o) and spin (m_s) atomic magnetic moments of the rare earth elements were calculated using the relations [101,102]:

$$m_z = m_o + m_s$$

$$m_{o,RE} = -\frac{2q}{r} N_h \mu_B,$$

$$m_{s,RE} = -2 \frac{\langle S_{eff} \rangle}{2 + 6 \frac{\langle T_z \rangle_{free}}{\langle S_z \rangle_{free}}} \mu_B, \qquad \langle S_{eff} \rangle = \frac{5p - 3q}{r} N_h \qquad (6.2)$$

with the free ion dipolar and spin operators $\langle T_z \rangle_{free} = 0.010$ and $\langle S_z \rangle_{free} = -3.466$ for Gd, and $\langle T_z \rangle_{free} = 0.243$ and $\langle S_z \rangle_{free} = -2.943$ for Tb [103]. The number of holes, $N_h = 7$ and $N_h = 6$ were chosen for Gd and Tb [38]. Similar relations were used for the Co sublattice [101,104]:

$$m_{o,Co} = -\frac{4q}{3r} N_h \mu_B, \qquad m_{s,Co} = -\frac{6p - 4q}{r} N_h \mu_B, \qquad (6.3)$$

with $N_h = 2.5$ for Co [38]. The integrated values of the XMCD and background-corrected XAS spectra were used to determine $p = \int_{L_3/M_5}(\mu_+ - \mu_-)d\omega$, $q = \int_{L_3+L_2/M_5+M_4}(\mu_+ - \mu_-)d\omega$, and $r = \int_{L_3+L_2/M_5+M_4}(\mu_+ + \mu_-)d\omega$.
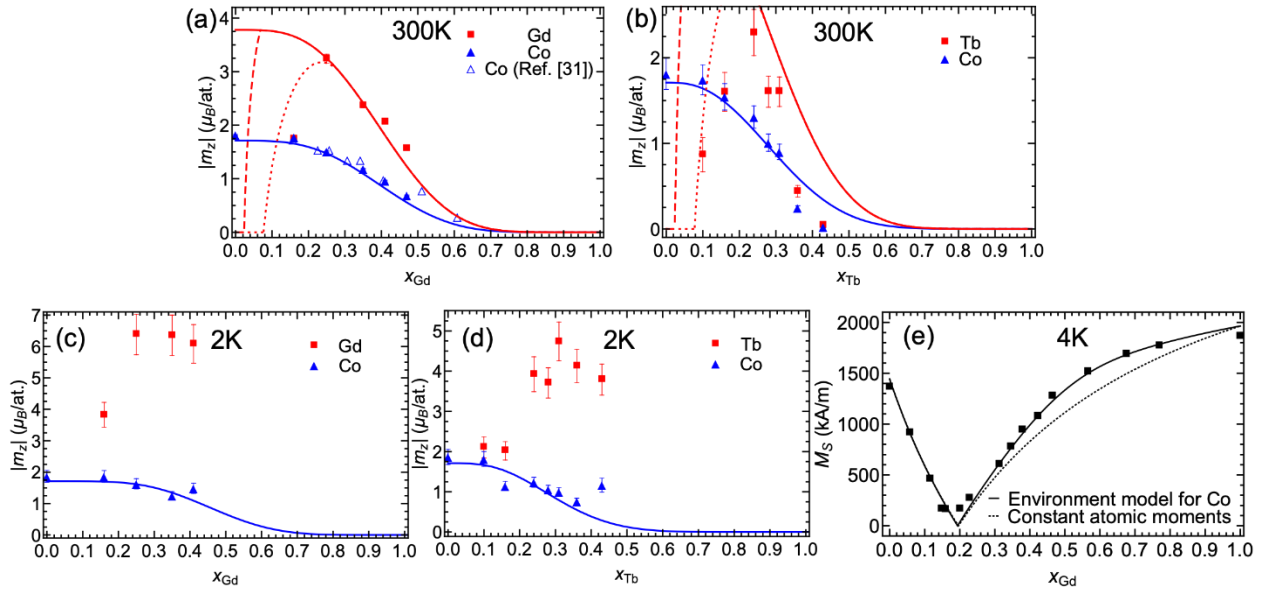
Figure 6.3: Average atomic moment variation of 6 nm (a) GdCo and (b) TbCo with varying RE composition at 300 K (a), (b) and 2 K (c), (d). (a), (b) Average atomic magnetic moments at 300 K. The combined environment and RE dead layer model is indicated by the solid red and blue lines with (a) $j = 7$ and (b) $j = 10$. The dashed (dotted) red lines indicate the predicted moment variation due to preferential deposition of one (three) atomic layer(s) of dead RE prior to alloy formation (see text). The open blue triangles in (a) are from a thick film of GdCo in Ref. [105]. (c), (d) Average atomic magnetic moments at 2 K with (c) $j = 7$ and (d) $j = 9$ for the Co sublattice. (e) GdCo M_s data at 4 K in a thick film, adapted from [93]. Solid line uses environment model for the Co sublattice while dotted line assumes constant moments for both sublattices (see text).

6.3 Variation of Atomic Moments with Composition

The extracted atomic magnetic moment magnitudes of 6 nm GdCo and TbCo as a function of composition are plotted in Fig. 6.3. In both GdCo and TbCo, the RE and Co moments have opposite signs across all compositions, indicating persistent antiferromagnetic ordering, consistent with previous observations of ferrimagnetic order in GdCo films as thin as 1 nm [38]. In the GdCo series, the orientations of the two sublattices invert between $x = 0.25 - 0.3$, suggesting a magnetic compensation composition in this range, consistent with the node of the red solid line in Fig. 6.1(d) and considerably higher than previously reported values in thick films of around $x = 0.2 - 0.22$ [45,93]. The Tb and Co sublattice orientations invert between $x = 0.31 - 0.36$, similarly far from the magnetization compensation composition found in 100 nm films [83].

As seen in Figs. 6.3(a)-(d), the magnitudes of the Gd, Tb, and Co moments decrease monotonically with increasing x at compositions above $x \approx 0.2$. The fact that the Co moment approaches the bulk moment of ~1.7 μ_B as $x \rightarrow 0$ suggests the absence of a significant Co dead layer, as is sometimes observed at interfaces in thin Co films and alloys [106]. The decrease in the Co moment upon alloying with the RE is reminiscent of previous studies of magnetic transition metals (Fe, Co, Ni) alloyed with non-magnetic impurities, which report a similar decrease in transition metal moment with increasing impurity concentration [105,107]. The reduction in transition metal moment has been accurately described by a discontinuous "environment model" proposed by Jaccarino and Walker [107]. This model asserts that the magnetic moment of a given magnetic transition metal atom is either zero or a maximum, depending on the number of transition metal atoms surrounding it. The average atomic moment is then just the maximum moment multiplied by the probability of a given atom having at least a critical number of transition metal

atom nearest neighbors. Described mathematically in the context of RE-Co, the average atomic moment of species i (Co, Gd, or Tb) is:

$$m_{z,i,env}(x) = P_j(x)m_{z,i}(x = 0) \qquad (6.4)$$

where x is the RE atomic fraction and

$$P_j(x) = \sum_{k=j}^{N} \binom{N}{k}(1-x)^k x^{N-k} \qquad (6.5)$$

is the probability of an atom having at least j nearest neighbor Co atoms as a function of RE concentration. Here N is the coordination number, $m_{z,i}(x = 0)$ is the maximum magnetic moment of species i, which occurs at $x = 0$, and $\binom{N}{k} = \frac{N!}{(N-k)!\,k!}$ is the binomial coefficient. Amorphous GdCo and TbCo have a random dense packed structure with maximal coordination numbers of $N = 12$ [46,105].

The solid blue lines in Fig. 6.3 show the environment model applied to the Co sublattice $m_{z,Co}(x = 0) = 1.71\,\mu_B$, showing excellent agreement with the measured Co moments in both GdCo and TbCo (solid blue triangles) at both 300 K and 2 K. The critical number of nearest Co neighbors j is found to be seven for GdCo (Fig. 6.3(a)) and 10 for TbCo (Fig. 6.3(b)) at room temperature. Previous investigations into atomic moment variations in magnetic alloys have focused on transition metal atomic moments and have found critical j values ranging from four in LaCo$_{5x}$Cu$_{5-5x}$ to eight in Y$_x$Co$_{1-x}$ alloys [105,107]. Replacing Y with Gd reduces the necessary number of nearest neighbors to seven, potentially arising from the influence of the weak Gd-Co antiferromagnetic interaction in addition to the strong Co-Co interaction. The open triangles in Fig. 6.3(a) correspond to data taken from Ref. [105] for Co in thick GdCo films. The consistency between the Co moments in thick and thin films suggests the Co magnetic moment is independent

of film thickness. XMCD measurements performed by Streubel et al. on $1 - 15$ nm GdCo confirm this assertion [38].

The RE atomic moment in RE-TM alloys is often assumed to remain constant across all compositions [4,108–110]. In contrast, our XMCD results at 300 K reveal non-linear RE moment dependencies on composition in both GdCo (Fig. 6.3(a)) and TbCo (Fig. 6.3(b)). Both Gd and Tb have Curie temperatures below 300 K [111], which suggests that the Gd-Gd/Tb-Tb interactions are negligibly weak relative to the Gd-Co/Tb-Co interactions. As a result, the RE atoms are highly sensitive to the local Co environment at temperatures near and above the RE Curie temperature, T_c. The solid red lines in Figs. 6.3(a) and (b) show the environment model applied to the Gd (Tb) moments with $j = 7$ ($j = 10$) and $m_{z,Gd}(x = 0) = 3.25\ \mu_B$ ($m_{z,Tb}(x = 0) = 4.5\ \mu_B$). Above $x = 0.2$, the environment model reasonably predicts the average RE atomic moment, especially for Gd. At low RE concentrations, both the Gd and Tb moments are significantly lower than the environment model predicts. We speculate that this moment reduction may be caused by the preferential growth of a RE dead layer at the Pt/RE-Co interface. This is discussed further below.

Upon reducing T to 2 K (Figs. 6.3(c) and (d)), the Co moments are virtually unchanged. The RE moments, however, are approximately constant above $x = 0.2$, suggesting that the environment model is still valid at low temperatures for transition metals, but not for rare earths as the RE-RE interactions become dominant relative to the RE-TM interactions. The low temperature RE moments allow us to determine the maximum possible fraction of Gd and Tb lost to oxidation during the deposition process by comparing our measured values with previous studies on pure Gd and Tb at low temperatures. Taking the 0 K atomic Gd moment as 7.02 μ_B [103] or 7.63 μ_B [112] and the measured Gd moment averaged over the films with x_{Gd} spanning $0.2 - 0.45$ as ~6.3 $\pm$ 0.4 μ_B, we determine a maximum Gd oxidation of 11 ± 5 % or 18 ± 5 % during

deposition. A similar calculation on the Tb moments using 9.34 μ_B as the 0 K Tb moment [113]

yields a Tb moment of 4.1 ± 0.2 μ_B corresponding to a maximum Tb oxidation of 57 ± 2 %. We

note that although the XAS spectra contain chemical state information, in our case, they do not

allow us to unambiguously characterize possible oxidation of the RE in our structures. The RE

edges are unaffected by oxidation and the O K-edge cannot be used to discriminate between

oxidized RE elements and Ta oxide, which is present due to partial oxidation of the capping layer.

Nonetheless, our data suggest that the highly reduced 2 K Tb moment is likely due to a

combination of oxidation during deposition and the sperimagnetic character of TbCo. Higher Tb

oxidation is expected due to a vacuum break between deposition of Ta/Pt/TbCo/Ta and the

protective Ta/Pt capping layer because of a sputter gun limitation. Without vacuum break, we

expect the Tb to oxidize at a similarly low rate as the Gd. Additionally, in TbCo, the RE and Co

sublattices are not collinear in contrast to GdCo, with Tb cone angles over 150°

reported [46,95,114,115]. As a result, the average Tb moment projected along the film normal will

be reduced relative to elemental Tb.

Low temperature M_s data of thick GdCo films as a function of Gd content are consistent

with our finding of constant RE and decreasing transition metal moment with increasing Gd

concentration at low T. Figure 6.3(e) shows M_s for thick GdCo films at 4 K, taken from the report

of Hansen, et al. [93]. The dotted line shows the predicted saturation magnetization assuming both

the RE and Co moments do not change with composition:

$$M_s(x) = \left| \frac{m_{z.Co}(1-x) - m_{z,RE}x}{v_{Co}(1-x) + v_{RE}x} \right| \tag{6.6}$$

with $m_{z,Co} = 1.72$ μ_B, consistent with previous low-temperature moment

measurements [104,116], and $m_{z,Gd} = 7$ μ_B . $v_{Co} = 1.100 \times 10^{-29}$ m^3 , $v_{Gd} = 3.305 \times$

10^{-29} m^3, and $v_{Tb} = 3.211 \times 10^{-29}$ m^3 are the atomic volumes of Co, Gd, and Tb, derived from

their bulk densities. This constant moment model predicts M_s well below compensation but underestimates the observed magnetizations at higher Gd concentrations. The solid curve in Fig. 6.3(e) instead assumes that the Co moment decreases according to the environment model with j = 7 ($m_{z,Co}(x) = 1.72\mu_B P_7(x)$) but keeps the Gd moment constant as indicated by the XMCD results. The resulting curve overlaps the constant moment curve below compensation but predicts higher magnetizations above compensation in alignment with the data. We conclude that far below T_c of the RE, while the TM moment still decreases with increasing RE concentration, as it does at room temperature, the RE moment is no longer affected by its local environment, maintaining a constant moment independent of composition.
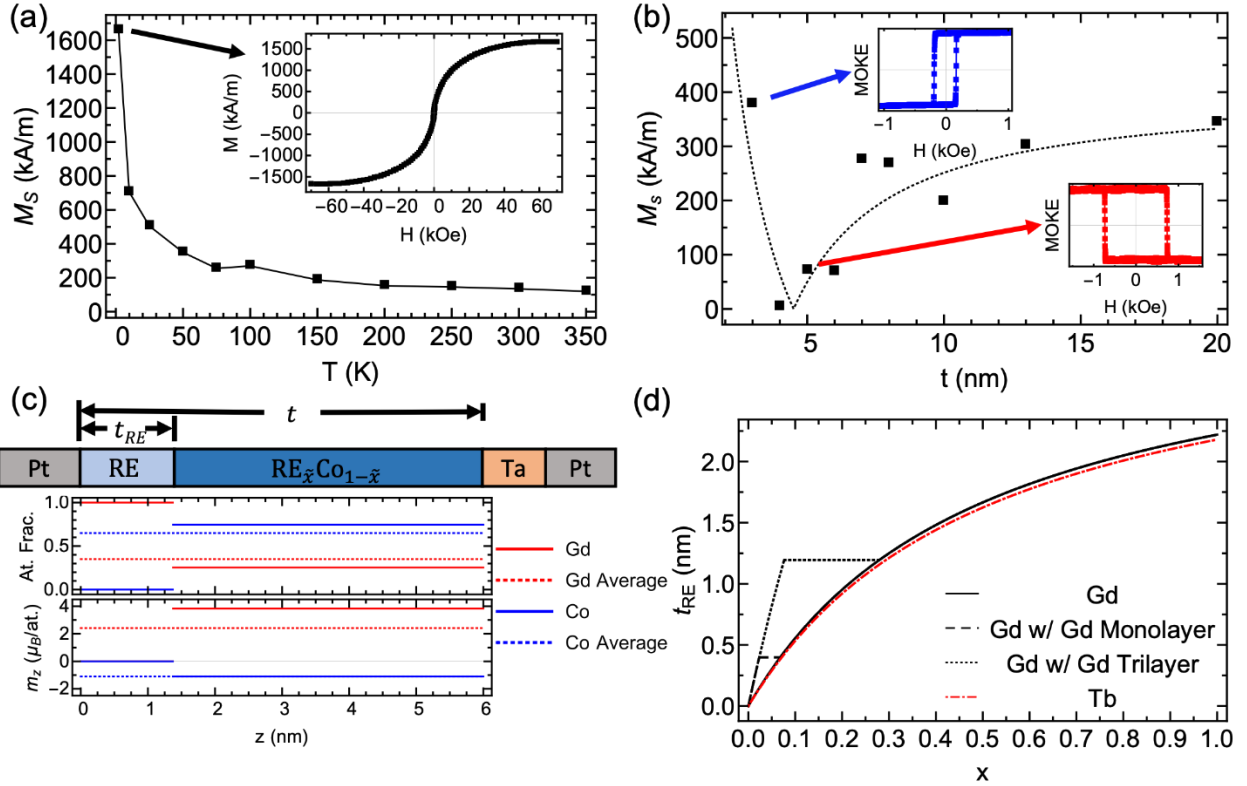
Figure 6.4: Dead layer effects on M_s and model schematic. (a) M_s extracted from SQUID hysteresis loops for a 3 nm $Gd_{0.7}Co_{0.3}$ film. All loops were measured in an out-of-plane configuration. Inset, 2 K hysteresis loop. (b) M_s data measured at $T = 300$ K for $Gd_{0.3}Co_{0.7}$ thickness series. Dotted line is model prediction for $x_{Gd} = 0.35$. Insets, MOKE loops indicating Co-dominant (blue) sample at 3 nm and Gd-dominant (red) sample at thicknesses above 4 nm. (c) Top, schematic of RE-Co sample with RE dead layer and alloyed RE-Co indicated. Middle, atomic concentration of Gd, Co versus z-coordinate along film thickness direction. Bottom, atomic magnetic moment versus z-coordinate. Solid lines indicate the local concentration/moment while the dotted lines indicate the average concentration/moment (equivalent to the nominal concentration) throughout the sample. (d) Best-fit rare-earth dead layer thicknesses used by model versus RE atomic fraction, x.

6.4 Reduction in Rare-Earth Moment due to Dead Layer

Having determined the GdCo atomic moment variations with composition, we investigated the apparent shift in compensation composition with decreasing ferrimagnet thickness. We first measured $M_S(T)$ for a 3 nm $Gd_{0.7}Co_{0.3}$ film, which had the highest Gd concentration in our film series, using superconducting quantum interference device (SQUID) magnetometry. The results are shown in Fig. 6.4(a). Previous work has found that T_c is reduced to below room temperature for Gd concentrations above $x \approx 0.47$ in thick films (Fig. 5.1(d)), where, for example, $T_c \sim 200$ K for $x = 0.7$ [45,93]. We observe a significant saturation magnetization of 135 kA/m at 300 K in our 3 nm $Gd_{0.7}Co_{0.3}$ film, in stark contrast with that finding. The low temperature M_S value of 1660 kA/m in Ref. [93], however, agrees well with the 4 K data in Fig. 6.3(e), indicating the nominal composition is accurate. The concavity of the plot in Fig. 6.4(a) is also notable. The T-dependence of RE-TM alloys can typically be approximated by two sublattices following a power-law with critical exponents, resulting in concave $M_S(T)$ curves except in the linear regime just around compensation [92,99,117]. The 3 nm $Gd_{0.7}Co_{0.3}$ film, however, has a convex $M_S(T)$ curve and a sharp drop in M_S from 2 to 100 K. A previous report on TbCo films with $x > 0.7$ and $t < 12$ nm has shown similar $M_S(T)$ behavior [114]. This suggests that there is a third contribution to the total M_S in thin films that has a much stronger temperature dependence than the other two sublattices.

To further confirm the observed M_S thickness dependencies in Fig. 6.1(d), we grew a thickness series of $Gd_{0.3}Co_{0.7}$ films at a constant composition and measured the resulting M_S (Fig. 6.4(b)). We observe a striking M_S behavior. At thicknesses above 7 nm, the M_S is approximately constant, as expected. Below 7 nm, the M_S dramatically drops to compensation at 4 nm, then increases again at $t = 3$ nm. The MOKE hysteresis loops undergo a polarity change across the M_S node as well, indicating a switch in dominant sublattice from Gd-dominant above 4 nm to Co-

dominant below. The thick film M_s data indicate that $Gd_{0.3}Co_{0.7}$ is expected to lie on the Gd-dominated side of compensation, making the 3 nm point anomalous. The crossover to Co-dominance at 3 nm could be explained by the reduction in Gd concentration in the alloyed 3 nm GdCo which would necessarily occur if there was Gd segregation in the sample.

The shift in compensation composition with thickness, the steep, concave reduction in M_s with temperature, and the M_s nodal behavior of the constant composition GdCo thickness series all suggest the presence of paramagnetic, "dead" Gd at room temperature that is segregated from the alloyed GdCo and only becomes significant in thin films. Previous investigations have observed complex structures in RE-TM alloys such as gradients [26] and agglomerations [118] that could result in a non-magnetic fraction of RE above and beyond what is predicted by the environment model. Additionally, the Gd atomic moment magnitude has been found to decrease with decreasing film thickness while the Co moment remains unchanged [38]. For simplicity, we will treat the excess dead Gd as a dead layer to explain our data phenomenologically. The dead layer results in an effective decrease in Gd moment relative to Co moment resulting in an increase in Gd concentration at compensation with decreasing film thickness seen in Figs. 6.1(d) and (e). The Gd dead layer magnetization decreases faster with increasing T compared to alloyed Gd since the dead layer Gd-Gd interactions are far weaker than the alloyed Gd-Co interactions. In very thin films with high Gd content, the Gd dead layer contributes heavily to the overall M_s at low T, resulting in the convex curvature seen in Fig. 6.4(a). Finally, the presence of a dead layer effectively reduces the concentration of alloyed Gd, whose influence on M_s becomes increasingly important as the ferrimagnetic layer gets thinner. At a critical thickness, this results in a dip in alloyed Gd concentration below the thick film compensation composition and shifts the dominant sublattice from Gd-dominant to Co-dominant as seen in Fig. 6.4(b).

6.5 Modeling Atomic Moment Variation in RE-TM Alloys

With knowledge of the atomic moment variations with composition and the existence of a RE dead layer, we can model the room temperature magnetic properties as a function of composition and thickness. To start, we assume a one-dimensional (1D) layer structure with an added dead RE layer at the bottom interface of the RE-Co (Fig. 6.4(c), top), although the physical location of the dead layer is not important to the model. The presence of the pure RE dead layer reduces the RE concentration in the alloyed region below the overall RE composition, x, to a new composition, $\tilde{x}$ (Fig. 6.4(c), middle). The atomic concentrations of RE and Co are given by

$$c_{RE}(x,z) = \begin{cases} 1, 0 \le z \le t_{RE} \\ \tilde{x}, t_{RE} < z \le t \end{cases} \quad c_{Co}(x,z) = \begin{cases} 0, 0 \le z \le t_{RE} \\ 1 - \tilde{x}, t_{RE} < z \le t \end{cases} \tag{6.7}$$

$$\tilde{x} = \frac{(t - t_{RE})x v_{RE} - t_{RE}(1 - x)v_{Co}}{(t - t_{RE}x)v_{RE} - t_{RE}(1 - x)v_{Co}} \tag{6.8}$$

with $\tilde{x}$ derived using the relation (see Appendix):

$$\frac{1}{t}\int_0^t \frac{c_{RE}v_{RE}}{c_{RE}v_{RE} + (1 - c_{RE})v_{Co}} dz = \frac{x v_{RE}}{x v_{RE} + (1 - x)v_{Co}} \tag{6.9}$$

given by conservation of volume. The moments are then determined as a function of position, z, by applying Eq. 6.4 to the concentration profiles above (Fig. 6.4(c), bottom). This results in a reduced average RE moment compared to a thick film due to the influence of the RE dead layer. As a first-order approximation, a constant fraction of RE atoms is assumed to contribute to the RE dead layer, up to a maximum dead layer thickness, $t_{RE,max}$. The resulting dead layer (Fig. 6.4(d)) is given by $t_{RE,max}$ scaled by the total RE volume fraction, $t_{RE}(x) = \frac{x v_{RE}}{x v_{RE} + (1-x)v_{Co}} t_{RE,max}$. The M_s was calculated using Eq. 6.6 and replacing the average RE moment,

$$\overline{m}_{z,RE,env} = \frac{(1 - x)\tilde{x}}{x(1 - \tilde{x})} m_{z,RE,env}\big(c_{RE}(x, t_{RE} < z \le t)\big) = \frac{(1 - x)\tilde{x}}{x(1 - \tilde{x})} m_{z,RE,env}(\tilde{x}) \tag{6.10}$$

for the standard RE moment $m_{z,RE}$ and using $m_{z,Co,env}(\tilde{x})$ for $m_{z,Co}$. This M_s function was then fitted to the $M_s(x)$ data in Figs. 6.1(d) and (e). The critical number of nearest neighbors, j, and maximum dead layer thickness, $t_{RE,max}$, were chosen as fitting parameters.

The solid curves in Figs. 6.1(d) and (e) show the combined environment and dead layer model fits. The dead layer determines the extent of compensation composition shift with thickness. A single maximum dead layer of $t_{Gd,max} = 2.22$ nm was found to describe the shift in GdCo compensation composition from the bulk condition in both 6 nm and 3 nm films. A nearly identical maximum dead layer was found in TbCo (Fig. 6.4(d)), demonstrating the generalizability of this dead layer model to other RE-TM alloys. The model curves also predict the downturn in M_s observed at high RE concentrations as the T_c drops below room temperature. For comparison, the dotted lines in Figs. 6.1(d) and (e) show the calculated M_s under the assumption of constant atomic moments, demonstrating the superior accuracy of the environment model and highlighting the significant errors introduced by ignoring coordination effects.

We return now to the anomalously low RE atomic moments at low RE concentrations seen in Figs. 6.3(a)-(d). As previously stated, the RE moments generally follow the environment model except below $x \approx 0.25$. This deviation does not significantly affect the M_s model calculation since the RE concentration is so low that variations in its moment have a minor effect on the volume-averaged M_s. However, it is unusual enough to warrant some speculation. The presence of a dead fraction of RE, whether in the form of a dead layer or due to agglomerates, implies some form of preferential growth takes place during the deposition of RE and Co upon Pt(111). Both elemental Gd and Tb have a surface energy three times smaller than Co and twice as small as Pt(111) [119]. As such, it is energetically favorable for RE to form an initial monolayer of atoms on Pt(111). This would cause an initially quick buildup of a RE dead monolayer, faster than the constant RE fraction

curve assumed in the black solid and red dash-dotted lines in Fig. 6.4(d) and would result in a reduction in RE moment at low concentrations due to all available RE atoms contributing to the dead layer initially. The dashed and dotted lines in Figs. 6.3(a) and (b) show the calculated moments under the assumption of a preferential Gd or Tb monolayer or trilayer at 300 K, highlighting the reduction in RE moment at low x. Similar reasoning can be applied to the 2 K RE moments. At low T (Figs. 6.3(c) and (d)), one would expect the pure RE layer to be ferromagnetic instead of magnetically dead. As a result, the pure RE moments can either align parallel or anti-parallel to the alloyed RE moments, depending on the dominant sublattice in the alloyed region. The anomalously low 2 K RE moments are below $x \approx 0.2$, meaning that the alloyed region is Co-dominated. In this case, under an applied field, the Co atoms will align parallel to the field, the alloyed RE atoms will align antiparallel to the field, and the ferromagnetic RE atoms will align parallel to the field, partially cancelling out the alloyed RE moments and resulting in a reduced average RE moment.

In addition to the total atomic moments, XMCD allows for the extraction of orbital and spin moments for each element. Figures 6.5(a) and (b) show the extracted orbital (m_o) and spin (m_s) magnetic moments of 6 nm GdCo and TbCo as a function of RE content at 300 K. As expected, the Gd orbital moment is quite small whereas the Tb orbital moment is comparable to its spin moment. The atomic spectroscopic g-factors were calculated from these moments using the relation [116]: $g = \frac{2m_e}{e} \frac{m_z}{\langle S_z \rangle} = \frac{2(m_s + m_o)}{m_s}$, with m_e the electron mass and $\langle S_z \rangle$ the spin angular momentum. As seen in Figs. 6.5(c) and (d), the atomic g-factors vary significantly as a function of composition, with the RE and Co g-factors even crossing over each other in both GdCo and TbCo. At the ends of the composition range, the atomic g-factors agree with previous measurements (g_{Gd} = 2.00 [120,121], g_{Co} = 2.187 [116]) but deviate from the expected values as their elemental

concentration decreases. Elemental *g*-factors are often used to calculate g_{eff} in ferrimagnets [91]. These results indicate that care must be taken to ensure that the atomic *g*-factors do not deviate from their pure elemental values at the composition of interest for accurate computation of net spin properties in RE-TM alloys.
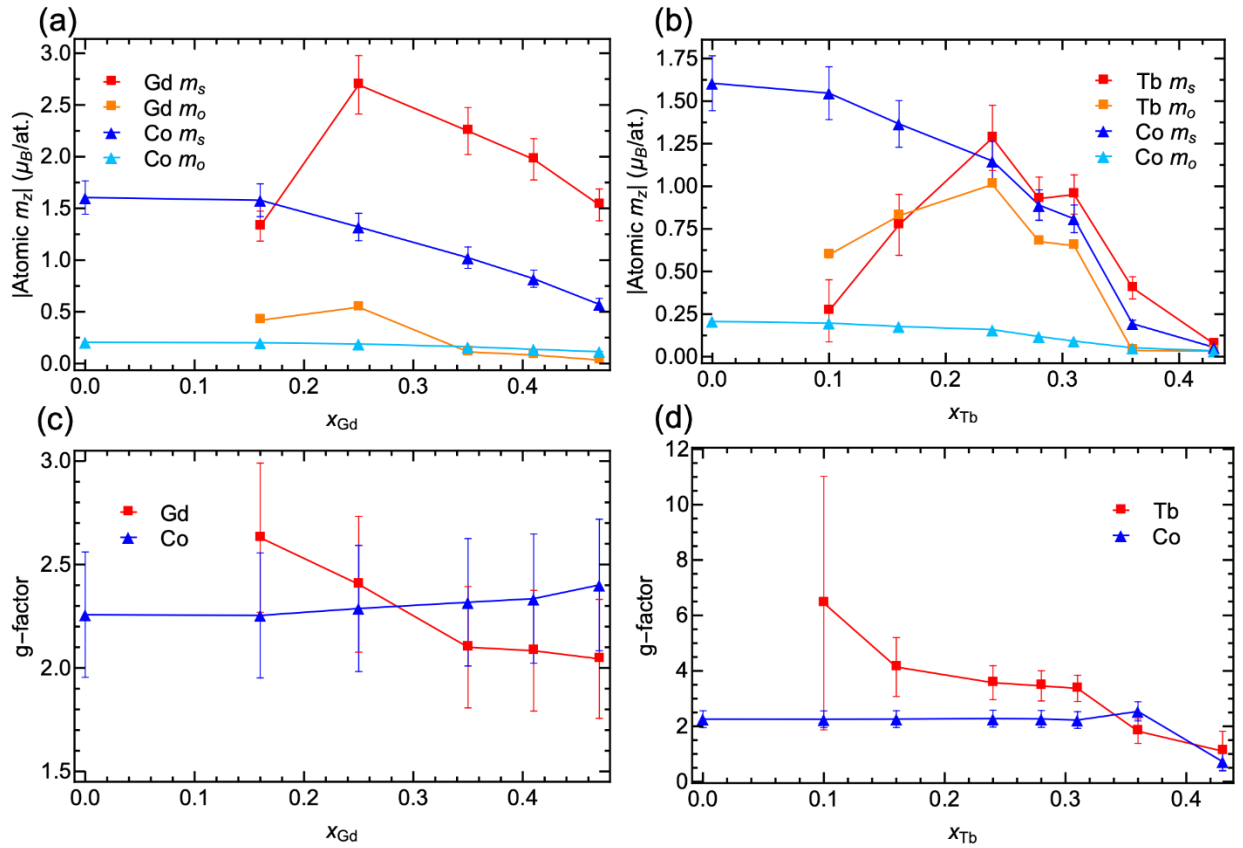

Figure 6.5: Spin and orbital moment contributions of GdCo and TbCo at 300 K. (a) GdCo and (b) TbCo spin (m_s) and orbital (m_o) moment data versus RE atomic fraction derived from XMCD data. (c), (d) Atomic spectroscopic *g*-factor data for GdCo and TbCo versus RE atomic fraction, calculated from spin and orbital atomic moments in (a) and (b).

6.6 Environment Model and Local Exchange

The discontinuous environment model describing the reduction in RE and TM atomic moment with increasing RE concentration that is presented in Eq. 6.4 assumes two possible values for the magnetic moment of a given atom depending on the discrete number of TM nearest neighbors: 0 or a maximum (Fig. 6.6(a)). After averaging all atomic moments of a given species by determining the probability of it having at least the critical number of nearest neighbors (Eq. 6.5), a continuous range of *average* atomic moments are possible, giving rise to the smooth moment reduction observed in Fig. 6.3. As demonstrated previously in this chapter, this simple model allows for accurate prediction of sublattice atomic moments in a tractable and intuitive manner. However, the environmental model can be refined by allowing the individual atomic moment to take on continuous values in accordance with conventional Weiss theory. As will be shown below, this formulation also demonstrates the intrinsic relation between number of TM nearest neighbors and Curie temperature, a property directly proportional to the Heisenberg exchange strength.

In a conventional ferromagnet, M_s reduces with increasing temperature according to:

$$M_s \propto \left(1 - \frac{T}{T_c}\right)^\beta$$
(6.11)

with β the critical index that typically ranges from $0.3 - 0.5$. Equation 6.11 gives the typical ferromagnetic behavior shown in Fig. 6.6(b) where M_s slowly decreases with increasing T and then rapidly decreasing near T_c. If Eq. 6.11 is plotted as a function of T_c at fixed T, the plot in Fig. 6.6(c) results. At fixed T, as T_c increases, M_s initially rapidly increases and then slowly increases according to β as $T_c > T$. The dotted red line overlaid on Fig. 6.6(c) represents the discontinuous environment model approximation of the same phenomenon. The deviation between the red dotted

line and solid black curve is the error introduced by assuming a simple discontinuous model. This error is a function of the curvature of M_s, governed by the value of β. The modulation of the number of nearest neighbor TM atoms is akin to tuning the local T_c. Since the Curie temperature is directly proportional to the effective exchange energy, $T_c \propto J_{ij}$, the number of nearest neighbor TM atoms must also be directly proportional to the local exchange energy. Thus, the observations of reduced Gd, Tb, and Co with increasing RE concentrations can also be interpreted as a reduction in average effective exchange in RE-TM alloys due to local exchange variation due to reduced TM coordination. This exchange reduction is explored quantitatively in the following chapter.
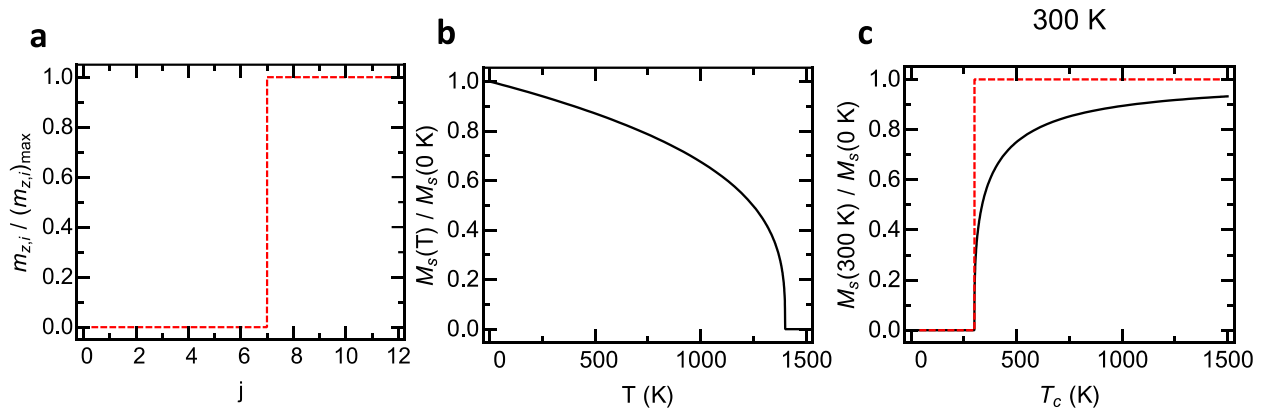
Figure 6.6: Environment model comparison to conventional Weiss theory. (a) Individual atomic moment versus number of nearest TM neighbors, j. (b) Normalized reduction in ferromagnet $M_s(T)$ from Weiss theory with $\beta = 0.313$ (3D Ising model) and $T_c = 1400\ K$. (c) Typical ferromagnet $M_s(T_c)$ at 300 K (solid black curve). Red dotted line represents discontinuous environment model approximation over the same T_c range, directly proportional to the number of TM nearest neighbors.

6.7 Summary

RE-TM alloys are an important class of materials for existing and future spintronic devices. Our results show a clear composition and thickness dependence on magnetic properties of the constituent elements in GdCo and TbCo alloys. We find that a nearest neighbor environment model describes the reduction in both RE and Co moments with increasing RE concentration at room temperature. The presence of a dead RE layer results in a systematic shift in magnetic compensation composition as the thickness of the film decreases. We demonstrate a simple, first-order model that predicts the saturation magnetization and average atomic moments as a function of thickness and RE composition. Finally, we observe a significant change in atomic g-factors as a function of composition in both GdCo and TbCo. This understanding of fundamental atomic magnetic properties in ferrimagnetic alloys allows future utilization of ultra-thin RE-TM films optimized for a variety of spintronic applications.

6.8 Appendix: Derivation of alloyed RE atomic fraction with RE dead layer

The overall RE volume fraction in a binary alloy of RE_xCo_{1-x} is given by:

$$f_{RE} = \frac{x v_{RE}}{x v_{RE} + (1-x) v_{Co}} \qquad (6.A1)$$

By conservation of volume, this is equal to the RE volume fraction at z averaged over the film thickness, giving equation Eq. 6.9. Applying the piecewise concentration profile of the RE from Eq. 6.7, $c_{RE}(x,z)$, Eq. 6.9 expands to:

$$\frac{1}{t}\left(\int_0^{t_{RE}} dz + \int_{t_{RE}}^{t} \frac{\tilde{x} v_{RE}}{\tilde{x} v_{RE} + (1-\tilde{x}) v_{Co}} dz \right) = \frac{1}{t}\left(t_{RE} + (t - t_{RE}) \frac{\tilde{x} v_{RE}}{\tilde{x} v_{RE} + (1-\tilde{x}) v_{Co}} \right) = f_{RE} \quad (6.A2)$$

Applying Eq. 6.A1 to Eq. 6.A2 and solving for $\tilde{x}$ yields the expression for alloyed RE atomic fraction presented in Eq. 6.8.

7 Dzyaloshinskii-Moriya interaction in rare-earth transition-metal thin films

7.1 Introduction

The preceding two chapters have focused on the optical and conventional magnetic properties of rare-earth (RE) transition-metal (TM) amorphous ferrimagnets. We found in those chapters that the magnetic properties of RE-TM alloys are in general strong functions of both composition and ferrimagnetic film thickness. Accordingly, RE-TM alloy characteristics that have often been assumed to be independent of composition and thickness, such as the average atomic moment of each sublattice or the magnetic compensation composition, have been shown to vary with thickness and composition in both GdCo and TbCo films. This chapter focuses on the dynamic properties of RE-TM heterostructures. We start by analyzing a 3 nm GdCo composition series via current-induced domain wall motion experiments in patterned magnetic racetracks, allowing for the determination of spintronic properties in a technologically relevant heterostructure. We first focus on films exhibiting perpendicular magnetic anisotropy (PMA) and then expand our measurement to low Gd content alloys with in-plane anisotropy using Brillouin light scattering (BLS) to observe the magnon dispersion relation under applied in-plane fields. By analyzing the domain wall motion results in the context of the RE-TM magnetic property variations explored in the previous chapter, we are able to extract the strength of Dzyaloshinskii-Moriya interaction (DMI) as a function of Gd concentration in Pt/GdCo/Ta heterostructures.

7.2 3 nm GdCo Magnetic Properties

Films of Ta(4 nm)/Pt(4 nm)/Gd$_x$Co$_{1-x}$(3 nm)/Ta(4 nm)/Pt(2 nm) were grown by D.C. magnetron sputter deposition on thermally oxidized Si wafers across a wide range of Gd concentrations, $x = 0 \rightarrow 0.7$. The lower Pt layer was selected to induce high interfacial DMI in the adjacent GdCo layer and additionally to provide a source of SOT to enable current-driven domain wall motion. A thin GdCo layer was chosen to maximize the interfacial DMI while minimizing potential unintentional bulk contributions to the DMI due to the presence of a growth-induced composition gradient [26]. The top Ta/Pt layers were added to prevent oxidation of the ferrimagnetic layer after growth and to maintain an asymmetric stack structure for maximum interfacial DMI. This 3 nm GdCo composition series was presented in Chapter 6 and used to support the existence of a RE dead layer (Fig. 6.1(d), blue triangles). The saturation magnetizations, M_s, of the films were measured by vibrating sample magnetometry (VSM) and are plotted again for convenience in Fig. 7.1(a). As observed previously, the apparent magnetic compensation point is at $x \approx 0.52$, in contrast with bulk amorphous GdCo compensation at $x \approx 0.22$ at room temperature [45,93]. The solid line shown in Fig. 7.1(a) is the combined environment and dead layer model fit used in the previous chapter. This model uses the standard expression for saturation magnetization,

$$M_s(x) = |M_{Co} - M_{Gd}| = \left| \frac{m_{z.Co,env}(1 - x) - \bar{m}_{z,Gd,env}x}{v_{Co}(1 - x) + v_{Gd}x} \right|, \tag{7.1}$$

with x the atomic fraction of Gd and v_i the atomic volume of Gd or Co, calculated from their bulk densities. $m_{z.Co,env}$ describes the Co atomic moment reduction due to a decrease in average number of Co nearest neighbors (see Eq. 6.4 and 6.5). $\bar{m}_{z,Gd,env}$ describes the Gd atomic moment reduction due to same effect that is further diluted due to the presence of a Gd dead layer (Eq.

6.10). Our extracted Co moment, $m_{z.Co,env}(x = 0) = 1.72\ \mu_B$, agrees with room temperature bulk Co magnetic parameters [18], indicating that the discrepancy in compensation composition between bulk and thin film GdCo is due to the reduced Gd atomic moment.
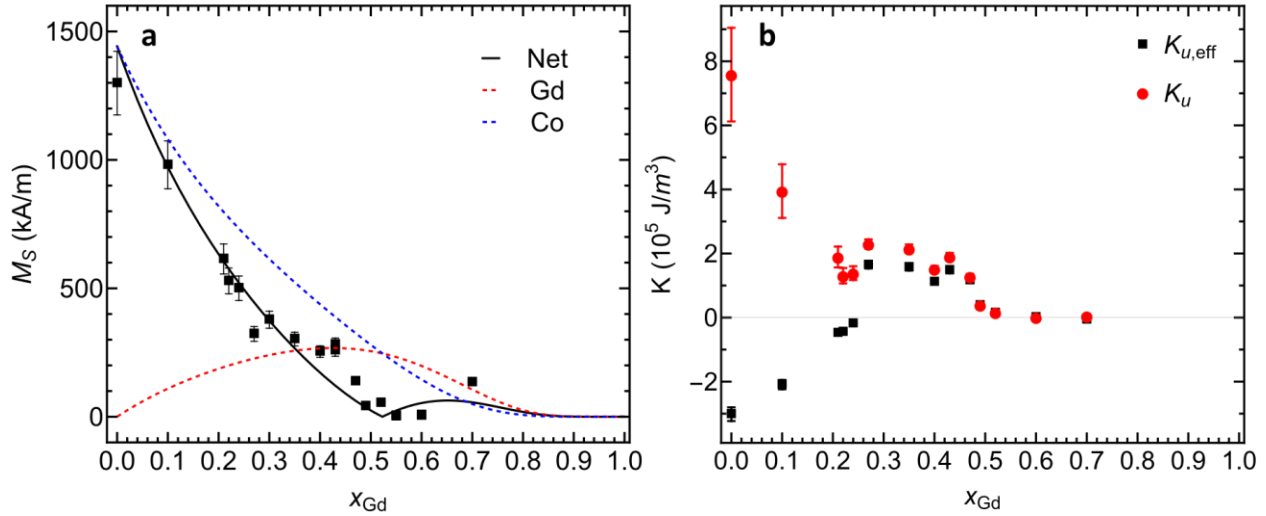
Figure 7.1: Saturation magnetization, M_s, and anisotropy of 3 nm GdCo. (a) M_s measured by vibrating static magnetometry. The solid black line is the combined environment model and dead layer model fit (see Chapter 6, [122]). The dotted red and blue lines show the expected sublattice magnetizations, M_{Gd} and M_{Co}, respectively. (b) Total effective, $K_{u,eff}$, and uniaxial anisotropy, K_u, of 3 nm GdCo deposited on Pt.

The effective magnetic anisotropy energy density (Fig. 7.1(b)), $K_{u,eff}$, was determined by measuring the anisotropy field, H_k, and using the equation: $K_{u,eff} = \pm \frac{1}{2}\mu_0 H_k M_s$, with positive (negative) sign indicating perpendicular (in-plane) magnetic anisotropy. H_k was determined via one of two methods (Fig. 7.2). Samples with in-plane anisotropy had easy-axis and hard-axis loops taken using a VSM. H_k was then determined by fitting the transition region and each saturation

branch of the hard axis loop and calculating the field intercepts (Fig. 7.2(a)). For PMA samples with $H_k > 7$ kOe, where saturated branches are difficult to spot on the VSM, longitudinal magneto-optical Kerr effect (MOKE) hysteresis loops were taken at normal incidence. For PMA samples in this geometry, the applied field is along the hard-axis, and the film normal component of the sample M is probed. The Stoner-Wohlfarth model for a sample with uniaxial anisotropy has energy:

$$f = \frac{1}{2}\sin^2(\theta - \phi) - h\cos\theta, \qquad h = \frac{M_s}{2K_{u,eff}}H, \tag{7.2}$$

with θ the angle of M with respect to the applied field H and ϕ the angle of the easy axis relative to H. When the applied field is along the hard axis, then $\phi = \pi/2$ and the film normal component is given by [123]:

$$m_\perp = \begin{cases} \pm\sqrt{1 - h^2}, & -1 \leq h \leq 1 \\ 0, & |h| > 1 \end{cases} \tag{7.3}$$

In an ideal case, this yields a circular longitudinal MOKE hysteresis loop. Due to a combination of slight misalignment between H and the hard-axis and small longitudinal Kerr angle being probed, the observed loops show switching (Fig. 7.2(b)). However, despite this non-ideality, the saturation field is readily apparent and can be accurately extracted by fitting Eq. 7.3 to the loop data.
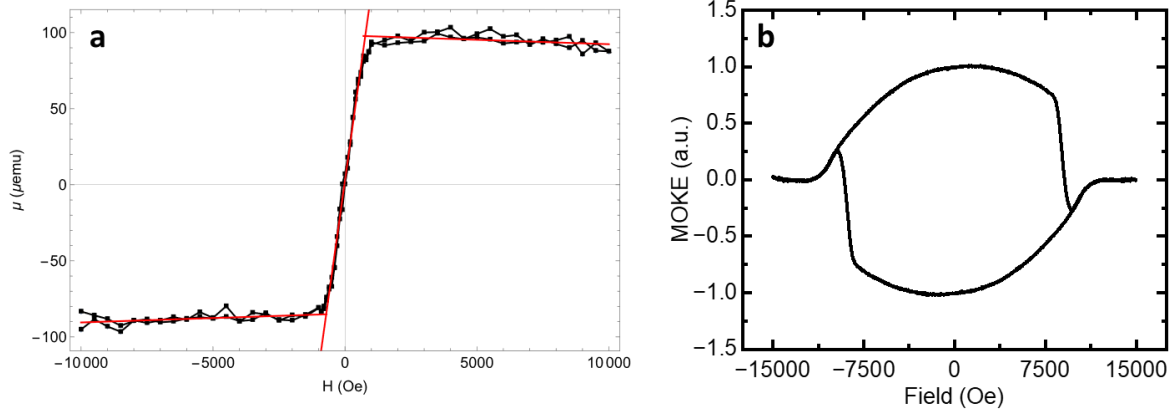
Figure 7.2: Methods of H_k extraction for anisotropy determination. (a) Hard-axis VSM loop of 3 nm $Gd_{0.24}Co_{0.76}$, displaying in-plane anisotropy with $H_k \approx -740$ Oe. Red lines show best fit lines of each branch of the loop. (b) Longitudinal MOKE hysteresis loop taken at normal incidence of PMA 3 nm $Gd_{0.27}Co_{0.73}$. $H_k \approx 10$ kOe.

The uniaxial anisotropy, K_u, was extracted by subtracting the in-plane magnetostatic contribution from the effective anisotropy, $K_u = K_{u,eff} - K_{ms} = K_{u,eff} + \frac{1}{2}\mu_0 M_s^2$. The K_u extracted for pure Pt/Co ($K_u = (7.6 \pm 1.5) \times 10^5$ J/m^3) was found to be slightly higher than the magnetocrystalline anisotropy reported in single-crystal bulk Co samples, $K \approx 5 \times 10^5$ J/m^3 [124]. This minor enhancement may be due to the spin-orbit coupling (SOC) induced by the Pt underlay, which is well-known to promote PMA in ultrathin Pt/Co structures [125,126]. The positive $K_{u,eff}$ (black squares) in Fig. 7.1(b) show the region of perpendicular magnetic anisotropy (PMA). The measurements of $K_{u,eff}$ near magnetic compensation ($x = 0.40 - 0.55$) agree with previously reported values of sputtered GdCo films at the same relative compositions ($x = 0.15 - 0.30$) [127–129]. At lower Gd concentrations $K_{u,eff}$ peaks at $x \approx 0.3$ before dropping below zero for $x < 0.27$ and $x > 0.6$. The uniaxial anisotropy K_u (red data points) decreases by over two

orders of magnitude over the composition series, $x = 0 - 0.7$, however, two distinct trends are evident in the K_u data. Overall, an exponential decrease is observed with increasing x, but starting at $x \approx 0.22$, K_u begins to increase with x until plateauing and finally decreasing $< 1 \times 10^5$ J/m^3 as $x \to 0.5$. This suggests that two factors contribute to the observed K_u. The overarching exponential decrease in K_u as x increases can be attributed to the induced interfacial PMA from the Pt underlayer and appears to proportionally decrease with the expected Co sublattice magnetization, M_{Co} (Fig. 7.1(a)). In addition to the Pt induced interfacial PMA, anisotropic pair-pair correlations have been found to introduce bulk PMA in RE-TM ferrimagnets [128,130–133]. This bulk PMA term is increases with the number of RE-TM pairs, with pair models indicating a maximum in the pair-ordering induced anisotropy from $x = 0.3 - 0.5$, consistent with the observed K_u trend in Fig. 7.1(b).

These results suggest that the uniaxial magnetic anisotropy in Pt/GdCo multilayers is governed by the combination of an interfacial Pt/Co interaction and bulk Gd-Co pair ordering. In 3 nm GdCo films, the Pt/Co PMA contribution dominates, and is diluted by the presence of Gd. As $x \to 0.24$, the large number of Gd-Co pairs results in a significant bulk PMA contribution that increases K_u, despite the reduced Pt/Co interaction, until the number of Gd-Co pairs is reduced at $x > 0.5$ and K_u rapidly decays. In the 3 nm GdCo series, this region exhibits net PMA behavior due to the small magnetostatic contribution from being near magnetic compensation. Despite the large uniaxial anisotropy at low x, the films exhibit in-plane anisotropy due to the large magnetostatic contribution overwhelming K_u. At $x > 0.5$, the uniaxial anisotropy is significantly weakened, and a small increase in magnetization is enough to yield in-plane anisotropy. As a result, only a finite window of compositions exhibits PMA, and an even smaller sliver of those are Gd-dominant. Based on these findings, we expect the PMA composition range to decrease with

increasing GdCo film thickness due to a weakening of interfacial Pt/Co with increased thickness and the significantly larger expected M_s at $x \approx 0.4$ due to its lower compensation composition, which would lead to an increase in K_{ms}, overwhelming the bulk PMA even at maximum pair population. Empirical evidence finds this to be true in 6 nm GdCo, where we observe a PMA range from $x = 0.25 - 0.47$ (Fig. 6.1(c)). It should also be noted that the compensation composition is not generally centered in the PMA composition range. In the 3 nm GdCo series, compensation occurs around $x \approx 0.52$, meaning only samples $0.52 < x \leq 0.6$ have PMA and are Gd-dominated, that is it is difficult to fabricate 3 nm GdCo Gd-dominated PMA samples. In contrast, in the 6 nm GdCo series, compensation occurs at $x \approx 0.3$, so samples $0.3 < x \leq 0.47$ are Gd-dominated and it is instead relatively difficult to fabricate 6 nm GdCo Co-dominated samples. Thus, understanding of the multiple contributions to $K_{u,eff}$ is of critical importance for the efficient design of PMA heterostructures.
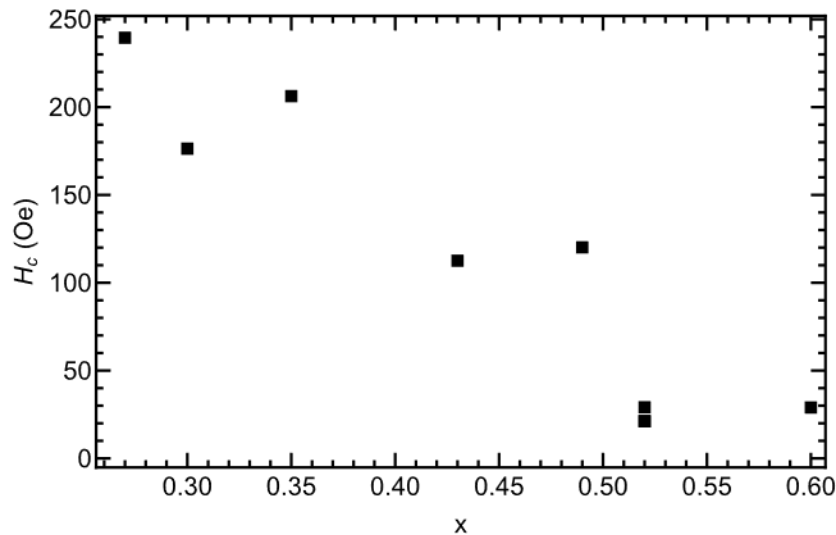
Figure 7.3: Coercivity of 3 nm Gd_xCo_{1-x} PMA films, measured by MOKE magnetometry.

The extracted coercive fields, H_c, of the PMA 3 nm GdCo films are plotted in Fig. 7.3. Typically, $H_c \propto \frac{K_{u,eff}}{M_s}$ [117,134], meaning that the coercivity is expected to diverge as x approaches the compensation composition in ferrimagnets. This trend is observed in previously grown 6 nm GdCo (Fig. 6.1(c)) and TbCo composition series. However, in the 3 nm GdCo composition series, H_c appears to monotonically decrease with increasing x. We note that $K_{u,eff}$ (Fig. 7.1(b)) is not constant over the entire composition range displayed in Fig. 7.3 ($x = 0.27 - 0.6$), however for $x = 0.27 - 0.47$, $K_{u,eff} \approx 1.8 \times 10^5$ J/m³ and precipitously drops at higher Gd content. Even over this reduced composition range, H_c falls by over 2x. Previous reports have observed a relationship between coercivity and surface roughness, with H_c decreasing with increasing roughness at moderate surface roughness with magnetization reversal due to a combination of coherent rotation and domain wall nucleation and growth [135,136]. As previously discussed in Chapter 6, interfacial effects such as a RE dead layer are increasingly prominent as the thickness of RE-TM films is reduced below ~10 nm. The coercivity trend observed in Fig. 7.3 suggests that in 3 nm GdCo, there may an increase in interfacial roughness, potentially due to the increased Gd dead layer thickness that works to reduce coercivity by lowering the energy barrier for domain wall nucleation and growth.

7.3 Domain Wall Motion Experiments

With the magnetic properties of the 3 nm GdCo composition series established, a series of current-induced domain wall motion experiments was conducted. A two-step photolithography process was employed to pattern magnetic racetracks onto the subset of samples exhibiting PMA. First, samples were coated with a negative resist and a UV laser writer was used to expose the racetrack regions, leaving resist covering the racetrack regions after development. Ar ion milling was then used to etch the resist-free regions down to the Si substrate and the remaining resist was removed using acetone. After acetone cleaning, the sample was again patterned and Ta(5 nm)/Au(150 nm) was deposited on the exposed regions to serve as contact pads. The contact pads were electrically connected to a waveguide by wedge wire-bonding. A wide-field MOKE difference image showing a magnetic racetrack with three wire-bonds attached to the Au contacts is shown in Fig. 7.4.

After the signal-to-noise (SNR) improvements to the wide-field MOKE microscope discussed in Chapter 4 were implemented, the remaining initial challenge for domain wall motion experiments was domain wall nucleation. Domain walls were nucleated via two methods. The first method utilized a 3 μm wide Au wire transverse to the magnetic racetrack to induce an Oersted field in the adjacent region of the racetrack, thereby nucleating a domain wall. The optimization of the pulse amplitude and length of the nucleation current density, j_{nuc}, necessary for nucleation made this method generally cumbersome and difficult to execute. The second method nucleated domain walls through spin-orbit torque (SOT) switching [137–139]. A large current density ($|j_{drive}| > 10^{12}$ A/m^2) was applied along the length of the racetrack under an applied ±1 kOe longitudinal magnetic field, H_x. This resulted in a switch in track magnetization direction with

domain wall nucleation at the Au wire on the left side of the track and at the track shoulder on the right side. The second method proved to more reliably nucleate domain walls.
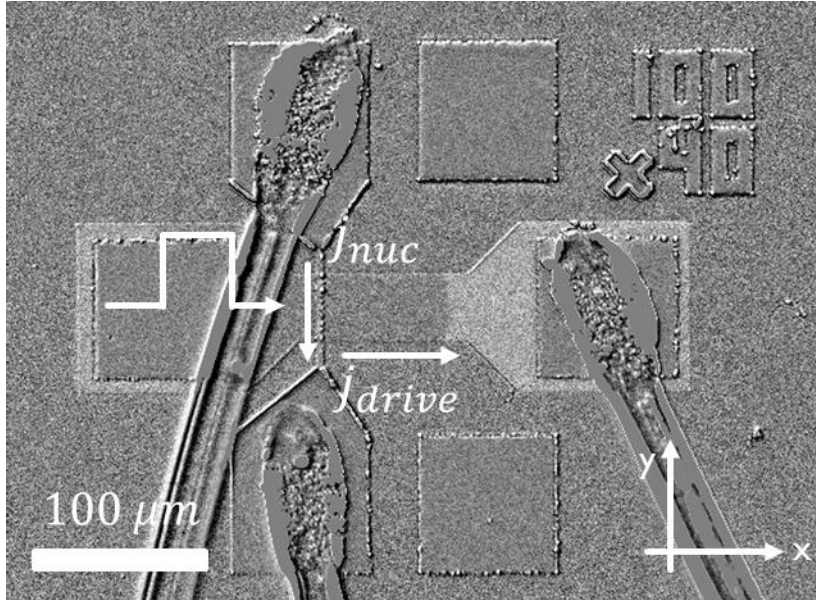
Figure 7.4: Wide-field MOKE microscope image of 100 x 40 μm magnetic racetrack showing a single "down-up" domain wall. Lighter region signifies $+z$ magnetization. Current pulses were injected from the left side with positive conventional current flowing along $+x$. Domain wall name (up-down/down-up) was defined with respect to the current flow direction.

7.3.1 Domain Wall Velocity Measurements

Once a domain wall was nucleated two sets of experiments were conducted. First, current-induced domain wall velocity was measured as a function of current density at zero applied longitudinal in-plane field H_x. Current pulses of $2 - 5$ ns were injected into the Pt underlayer to induce spin current injection into the adjacent ferrimagnetic layer, resulting in translation of the domain wall in the direction of conventional current flow. After each pulse train of $1 - 5$ pulses,

an image was acquired to determine extent of domain wall displacement. Once a net displacement of ~70 μm had occurred and $10 - 20$ images were acquired, the slope of the domain wall displacement versus total current pulse time was used to determine the domain wall velocity.
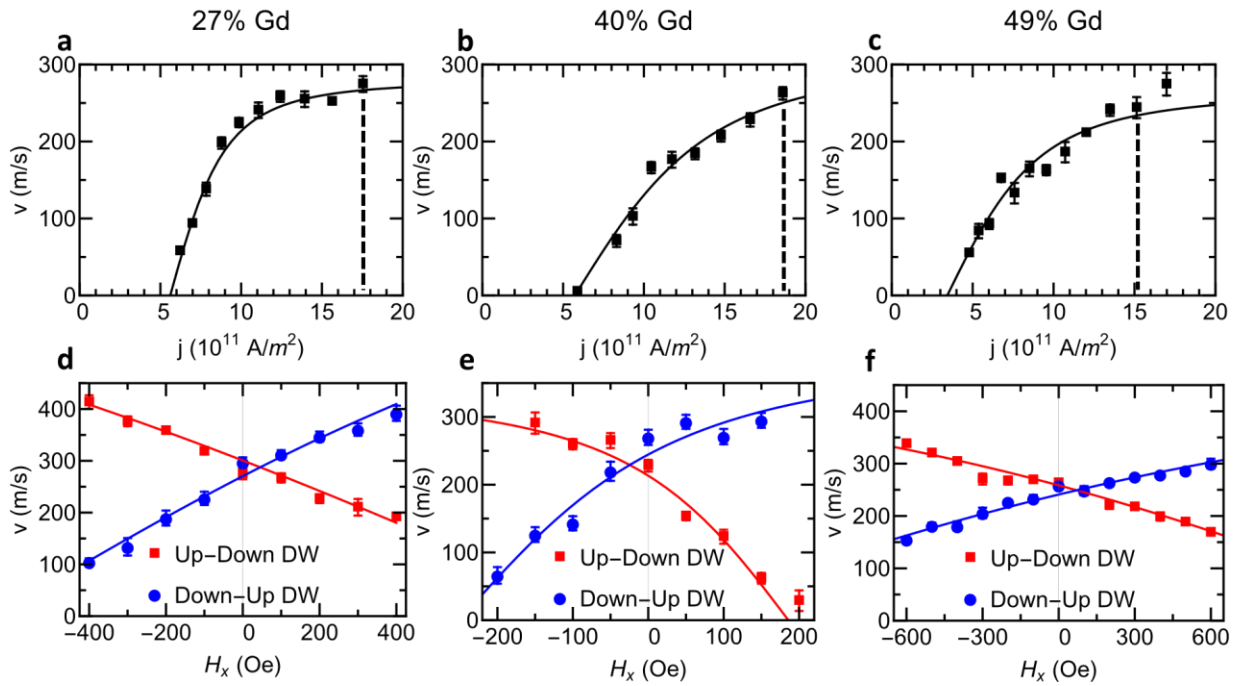
Figure 7.5: Current-induced domain wall velocity measurements in Pt/GdCo heterostructures at 3 representative compositions. (a) – (c) Domain wall velocity vs. applied current density at $H_x = 0$. Dotted line indicates j used for corresponding v vs. H_x measurement below. (d) – (f) Domain wall velocity vs. H_x. Solid lines are fits to the 1D model (see text). The error bars are the standard error of $5 - 20$ measurements.

Figures 7.5(a) – (c) show the measured domain wall velocity as a function of applied current density, j, under $H_x = 0$ in $x = 0.27, 0.40,$ and 0.49, spanning the PMA composition range. At all compositions the domain wall velocity initially increases linearly with j before eventually saturating at some critical current density. An applied charge current through the heavy metal Pt

layer induces a transverse spin current due to the spin Hall effect (SHE), creating an effective out-of-plane field proportional to the applied current density, $H_{SH} = \chi j$. The proportionality constant is related to the spin Hall angle of the heavy metal, θ_{SH}^{eff}, by [140]:

$$\chi = \frac{\pi \hbar \theta_{SH}^{eff}}{4 e \mu_0 M_s t},$$ (7.4)

with e elementary charge, μ_0 the permeability of free space, and t the thickness of the magnetic layer. In samples with homochiral Néel domain walls due to DMI, the resulting domain wall velocity is described by the 1D model [33]:

$$v = \frac{\frac{\pi}{2} \gamma_{eff} \Delta \, \mu_0 H_{SH}}{\sqrt{\alpha_{eff}^2 + \left(\frac{H_{SH}}{H_D + H_x}\right)^2}}$$ (7.5)

where Δ is the domain wall width, H_D is the DMI effective field, and H_x is the externally applied in-plane longitudinal field, parallel to the current direction. The terms γ_{eff} and α_{eff} are the effective gyromagnetic ratio and Gilbert damping, defined for ferrimagnetic materials by [6,91]:

$$\gamma_{eff} = \frac{M_s}{S}, \qquad \alpha_{eff} = \frac{S_0}{S}, \qquad S = \left| \frac{M_{Co}}{\gamma_{Co}} - \frac{M_{Gd}}{\gamma_{Gd}} \right|, \qquad S_0 = \alpha_0 \left(\frac{M_{Co}}{\gamma_{Co}} + \frac{M_{Gd}}{\gamma_{Gd}} \right)$$ (7.6)

with M_i the ferrimagnetic sublattice magnetization and S the net spin density. H_D is normal to the domain wall and acts to stabilize it in a Néel state, allowing for current-induced motion to occur. It is related to the DMI strength, D by,

$$D = \mu_0 M_s H_D \Delta$$ (7.7)

Under large, applied j, and equivalently large H_{SH}, Eq. 7.5 simplifies to:

$$v \approx \frac{\pi}{2} \gamma_{eff} \Delta \, \mu_0 (H_D + H_x),$$ (7.8)

signifying that the domain wall velocity saturates at a value proportional to the DMI effective field. Substituting Eqs. 7.6 and 7.7 into 7.8 reveals that the maximum velocity, v_{max}, is solely dependent

on the DMI strength and net spin density in the absence of an applied field, $v_{max} \propto \frac{D}{S}$. At small j, α_{eff} becomes important and v increases approximately linearly with j. Returning to Figs. 7.5(a) – (c), we see the characteristic linear behavior of v at small j and a clear saturation velocity in Figs. 7.5(a) and (c). In Fig. 7.5(b), we do not observe complete saturation over the applied current density range. To determine v_{max}, the data in Figs. 7.5(a) – (c) was fit to a variant of Eq. 7.5 of the form:

$$v = \frac{v_{max}(j - j_0)}{\sqrt{\xi^2 + (j - j_0)^2}}, \qquad \xi = \frac{\alpha_{eff}H_D}{\chi}, \qquad (7.9)$$

with j_0 the depinning current density, or the minimum current necessary to induce domain wall motion and j_0, v_{max}, and ξ chosen as fitting parameters.
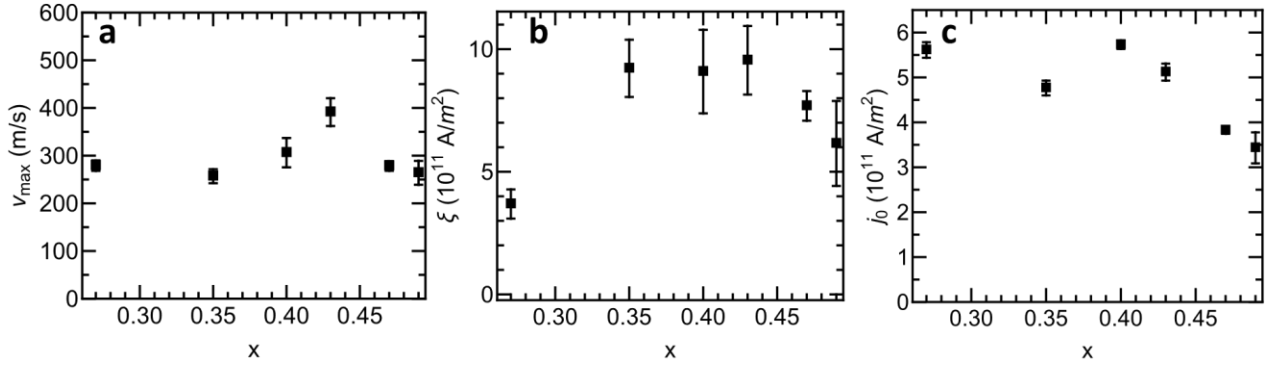

Figure 7.6: Extracted fitting parameters from v vs. j domain wall measurements.

The values of the fitting parameters are shown in Fig. 7.6. The terminal velocity is similar at $x = 0.27$ and $x = 0.49$ and shows a peak around $x = 0.43$. This behavior is reminiscent of $v(T)$ data observed near angular momentum compensation previously reported in 6 nm

GdCo in which the domain wall velocity was found to diverge [4–6], suggesting that angular momentum compensation occurs at $x = 0.43$ in this series.

To determine the DMI effective field, H_D, domain wall velocities were measured at constant j as a function of H_x. A large j was chosen in the velocity saturation regime based on the zero-field domain wall velocity data in an effort to achieve a linear response between v and H_x, as predicted by Eq. 7.8, in which the zero-velocity field (horizontal-axis intercept) is H_D. The results are shown in Figs. 7.5(d) – (f). For all compositions, the up-down (down-up) domain wall velocity decreases (increases) with increasing H_x, indicating no domain wall chirality flip occurs over this composition range and consistent with left-handed domain walls and $D > 0$. However, while the data in Figs. 7.5(d) and (f) show linear trends in $v(H_x)$, the data in Fig. 7.5(e) exhibits highly non-linear behavior due to application of j below the saturation regime. As a result, the simple linear model of Eq. 7.8 is insufficient and the full 1D model of Eq. 7.5 is required to fit the data. Generally, α_{eff}, Δ, and γ_{eff} are not known, nor is χ, meaning that the scaling factor between j and H_{SH} is not known, so it is not possible to use Eq. 7.8 in isolation to fit the measured data. To work around this, we define a reduced field and rewrite Eq. 7.5,

$$v = \frac{\beta h\, H_D}{\sqrt{\alpha_{eff}^2 + \left(\frac{h\, H_D}{H_D + H_x}\right)^2}} \qquad (7.10a)$$

with,

$$h = \frac{H_{SH}}{H_D}, \qquad \beta = \frac{\pi}{2}\gamma_{eff}\Delta\mu_0 \qquad (7.10b)$$

The reduced field, h, is determined from the $v(j)$ data using a reduced velocity,

$$v_r = \frac{v}{v_{max}} = \frac{h}{\sqrt{\alpha_{eff}^2 + h^2}} \tag{7.11}$$

v_r is a measure of the degree of saturation. At true saturation, $v_r = 1$ and the 1D model is fully linear. α_{eff} is determined independently from depinning experiments described below. Equation 7.10 in combination with Eq. 7.11 allows for the accurate fitting of $v(H_x)$ at any j, as demonstrated by the solid lines in Figs. 7.5(d) – (f). The extracted values of β, representing the curvature observed in the $v(H_x)$ data, are plotted in Fig. 7.7(b). Figure 7.7(a) shows the variation in H_D with Gd concentration. The DMI effective field shows a minimum near the presumed angular momentum compensation point. With knowledge of the domain wall width, both H_D and β can be converted to key spintronic properties, the DMI strength and effective g factor, respectively. In Section 7.4, a method for estimating Δ in RE-TM films is discussed.
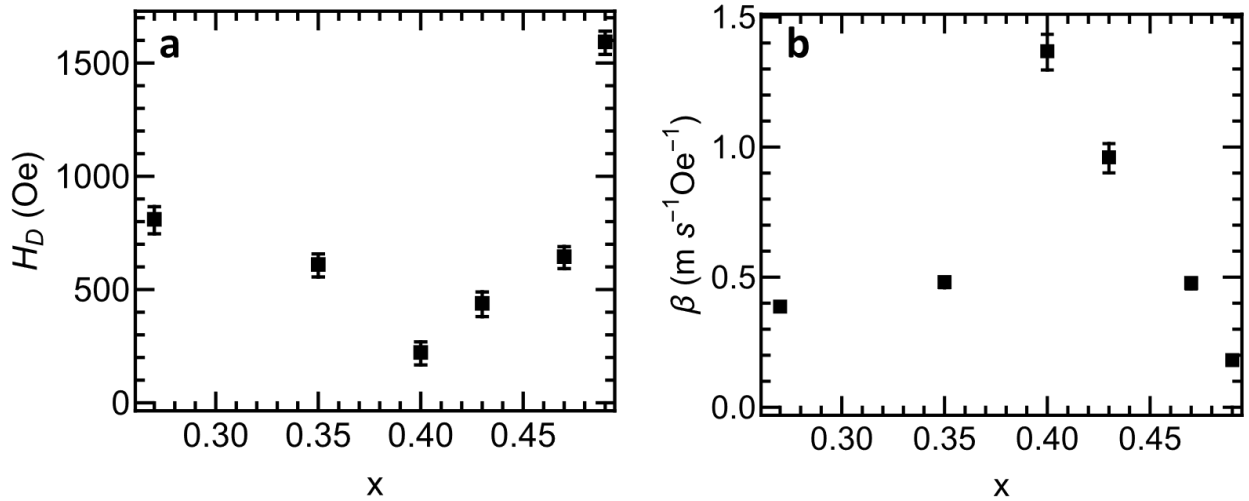

Figure 7.7: Extracted fitting parameters (a) H_D and (b) $\beta = \frac{\pi}{2}\gamma_{eff}\Delta\mu_0$ from v vs. H_x domain wall measurements.

7.3.2 Domain Wall Depinning Measurements

To fully characterize the spin transport properties of GdCo, domain wall depinning experiments were carried out on the devices. To start, a domain wall was consistently nucleated at the same location on a magnetic racetrack. A low DC drive current was then applied, and an assisting out-of-plane field was slowly increased until the domain wall moved ~50 μm. The field at which motion occurred for a given j is the depinning field, ΔH_{dp}. The experiment was repeated for both up-down and down-up domain walls. A representative plot showing data measured on Gd$_{0.4}$Co$_{0.6}$ is displayed in Fig. 7.8(a). As expected, the required depinning field linearly decreases with increasing j, and is unaffected by the domain wall polarity (up-down/down-up). By extracting the slope of $\Delta H_{dp}(j)$, the SOT efficiency, χ, or the effective out-of-plane induced per unit current density is determined (Fig. 7.8(b)). χ is found to exponentially increase with decreasing M_s (From Fig. 7.1(a) magnetic compensation is $x \approx 0.52$), consistent with Eq. 7.4 and previous reports near magnetic compensation [141–143]. However, when χ is plotted against inverse magnetization, it is found to increase quadratically with M_s^{-1} instead of linearly as expected (Fig. 7.8(c)). Solving for the effective spin Hall angle, θ_{SH}^{eff}, using Eq. 7.4 explains this behavior. θ_{SH}^{eff} is found to increase with Gd concentration. A report TbCo alloys reported a similar increase in θ_{SH}^{eff} with increasing Tb content [144] and theoretical work has shown significant SOT generated by RE atoms, dependent on the RE atoms' Fermi level and 4f electron energy [145]. Determination of θ_{SH}^{eff} rely on domain wall depinning measurements that observe net SOT phenomena. As a result, the extracted θ_{SH}^{eff} does not distinguish between individual sublattices (that is, Pt/Co versus Pt/Gd interactions); only the combined effect is measured. The increase in θ_{SH}^{eff} with RE content suggests that the RE sublattice contributes non-trivially to the total SOT in RE-TM alloys.
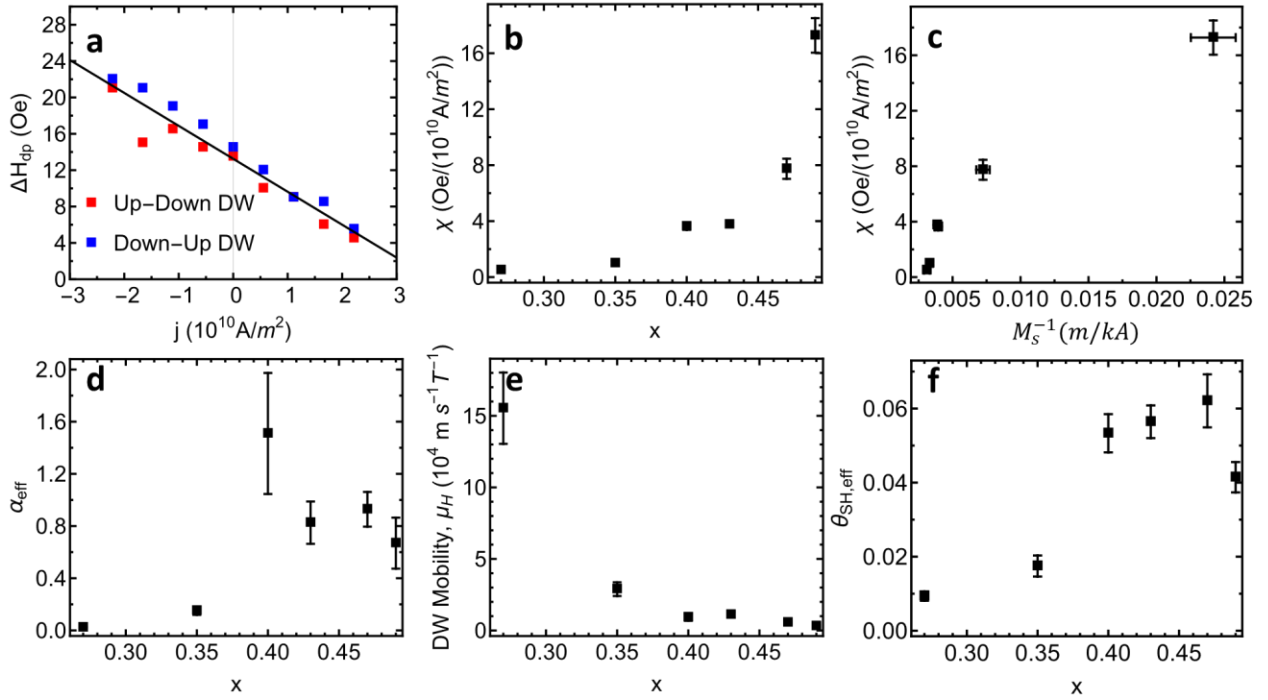
Figure 7.8: Domain wall depinning experimental results. (a) Representative $\Delta H_{dp}(j)$, taken on Gd$_{0.4}$Co$_{0.6}$. (b) SOT efficiency extracted from the slopes of the data measured in (a). (c) SOT efficiency versus M_s^{-1}. (d) Damping values in GdCo, showing angular momentum compensation at $x \approx 0.4$. (e) Domain wall field mobility versus composition. (f) Effective spin Hall angle versus composition.

From Eq. 7.9, knowledge of χ and H_D allows for the calculation of the damping constant, α_{eff}, shown in Fig. 7.8(d). Based on Eq. 7.6, we expect α_{eff} is increase as the net spin density decreases, suggesting that in Fig. 7.8(d), spin is minimized at $x \approx 0.4$, consistent with observation of enhanced terminal domain wall velocity near that same composition in Fig. 7.6(a). We observe $> 10 \times$ higher α_{eff} on the Gd-dominated side of angular momentum compensation compared the

Co-dominated side. We attribute this significant increase in α_{eff} to the presence of the Gd dead layer potentially increasing surface roughness, which has been shown to enhance damping [146]. Finally, we plot the field domain wall mobility, μ_H, determined from,

$$\mu_{DW,H} = \frac{\frac{\pi}{2}\gamma_{eff}\Delta}{\alpha_{eff}} = \frac{v_{max}}{\alpha_{eff}\mu_0 H_D} \tag{7.12}$$

We see μ_H exponentially decrease with increasing x, complementing the SOT observed. In the measured composition series, these two effects balance each other out, resulting in steady v_{max}, except in the vicinity of angular momentum compensation.

7.4 Exchange Stiffness in RE-TM Ferrimagnets

Using only the domain wall motion experiments described in the previous section, a number of dynamic magnetic properties can be extracted such as α_{eff}, χ, and θ_{SH}^{eff}. However, both the DMI strength, D, and γ_{eff} are dependent upon the domain wall width, Δ. In general, due to its small scale Δ is difficult to determine experimentally. However, its value can be estimated from magnetostatic theory from $K_{u,eff}$ and the exchange stiffness, A. In this section, we discuss how to estimate A based on previous reports and our findings from Chapter 6.

7.4.1 Exchange in thick films

In ferrimagnetic materials, two or more sublattices are antiferromagnetically coupled to produce a net magnetic moment (and net spin density) smaller than the sum of the sublattice magnetizations (spin densities). For rare-earth (RE) transition-metal (TM) amorphous

ferrimagnets this results in three distinct exchange interactions: ferromagnetic RE-RE and TM-TM interactions and an antiferromagnetic RE-TM interaction. Exchange interactions are quantified by an exchange constant, J_{ij}, which dictates the strength of the Heisenberg interaction between spins S_i and S_j, and typically derived from mean field analysis [45,99,147–149]. Changes in the relative strength of these three exchange interactions may result in radically different magnon dispersion relations ranging from purely FM to AFM in character.

Previous reports on amorphous GdCo thin films have reported a linearly decrease in J_{Co-Co} with increasing atomic fraction of Gd while observing no change in J_{Gd-Co} with composition [93,148]. Additionally, a study on GdCoMoAr alloys observed constant J_{Co-Co} and a significant decrease in J_{Gd-Co} with increasing Ar [147,148]. A recent study in our group found that both FM and AFM exchange could be reduced upon introduction of hydrogen [66]. These reports suggest that composition is an important parameter in tuning the exchange interaction in ferrimagnets, and that distinct exchange interactions can independently be tuned by alloying non-magnetic elements.
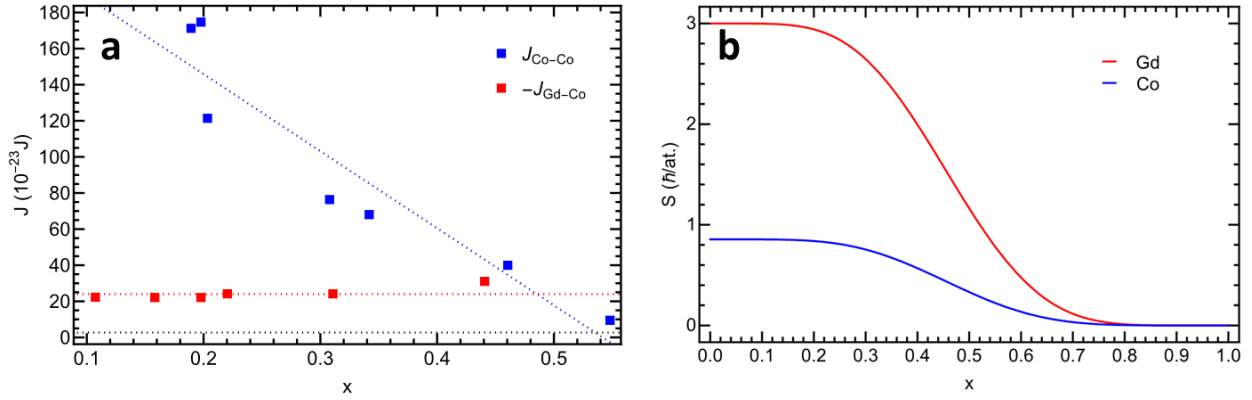
Figure 7.9: (a) Previously reported exchange energies in thick GdCo films. Black dotted line shows J_{Gd-Gd} exchange level from [148]. Red and blue squares are from [93,148]. (b) Average atomic spin in thick Gd_xCo_{1-x} films showing decay due to environment model.

Studies on Y_xCo_{1-x} and $LaCo_{5x}Cu_{5-5x}$ systems have found the average Co atomic moment (and by extension, its spin) to decrease with decreasing Co content according to a discontinuous environment model based on each Co atom's number of Co nearest neighbors [105,107]. Our recent work on GdCo and TbCo alloys has demonstrated that this effect extends to RE elements above their Curie temperature $T_{C,RE}$, i.e., both the TM and RE element atomic moments decrease with increasing RE concentration (see Chapter 6, [122]). This results in average atomic spins in Gd_xCo_{1-x} that follow the form:

$$S_{z,i,env}(x) = P_j(x)S_{z,i}(x = 0)$$

,

$$P_j(x) = \sum_{k=j}^{N} \binom{N}{k} (1-x)^k x^{N-k} \tag{7.13}$$

P_j describes the probability of atom i having at least j nearest neighbor Co atoms. $S_{z,i}(x = 0)$ is the maximum spin at a given temperature in a pure material composed of i. The variation in Gd and Co spin is plotted for a thick GdCo film as a function of Gd composition in Fig. 7.9. The

environment model predicts the downturn observed in M_s (Fig. 7.10(a)) at high Gd concentrations at room temperature owing to the low T_c of pure Gd.
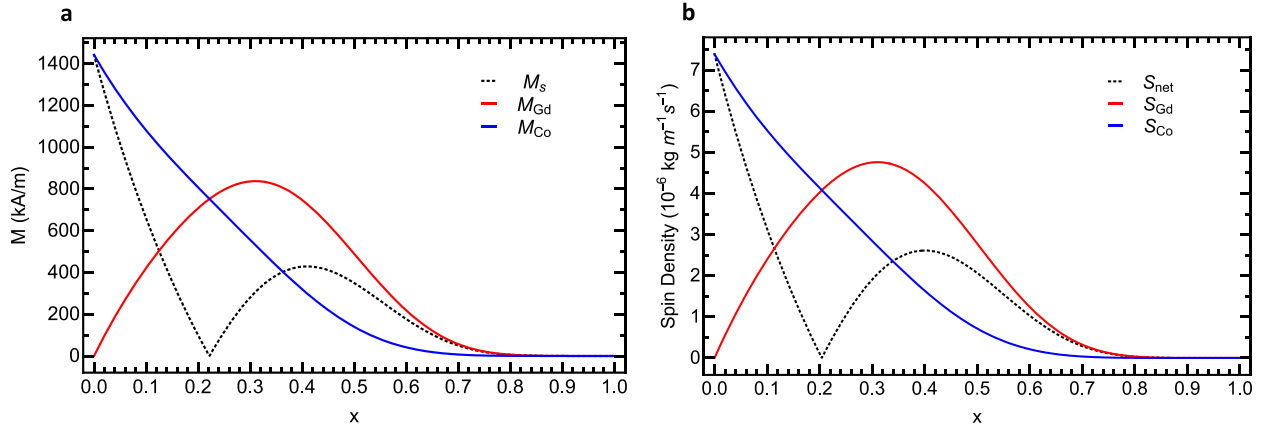
Figure 7.10: Sublattice magnetizations (a) and spin densities (b) as a function of x in thick GdCo.

In practice, exchange is often characterized by a volumetrically normalized exchange energy termed exchange stiffness. For a cubic system ferromagnet the exchange stiffness is given by $A = \frac{nJS^2}{a}$, with n the number of atoms/unit cell, a the lattice constant, and S the spin magnitude [117]. However, for a two-sublattice ferrimagnet, the exchange stiffness is the sum of each interaction [147],

$$A_{tot} = A_{11} + A_{22} + A_{12} \tag{7.14}$$

with

$$A_{11(22)} = \frac{1}{6} N_a S_{1(2)}^2 J_{11(22)} N_c r_{11(22)}^2 x_{1(2)}^2, \qquad A_{12} = \frac{1}{3} N_a S_1 S_2 J_{12} N_c r_{12}^2 x_1 x_2 \tag{7.15}$$

Here, N_a is the number of atoms per unit volume, N_c is the coordination, r_{ij} is the distance between i and j atoms, and x_i is the mole fraction of species i. Combining our model for spin decay with empirical exchange energy data allows us to compute the expected exchange stiffness as a function of composition (Fig. 7.11(a)). From the plot we can see that GdCo is initially dominated by Co-Co FM interactions until $x \approx 0.3$ where AFM interactions begin to dominate. The ratio of FM exchange to AFM exchange can be tuned at a constant x by adding a non-magnetic alloying element, such as Y (Fig. 7.11(c)). As demonstrated in Fig. 7.11(c), the addition of Y tunes the dominant exchange from AFM to FM while keeping x constant. This strategy allows one to maintain the ferrimagnet's degree of angular momentum and magnetic compensation while independently adjusting the ratio of exchange, potentially enabling AFM-like magnon characteristics while maintaining FM-like static properties.
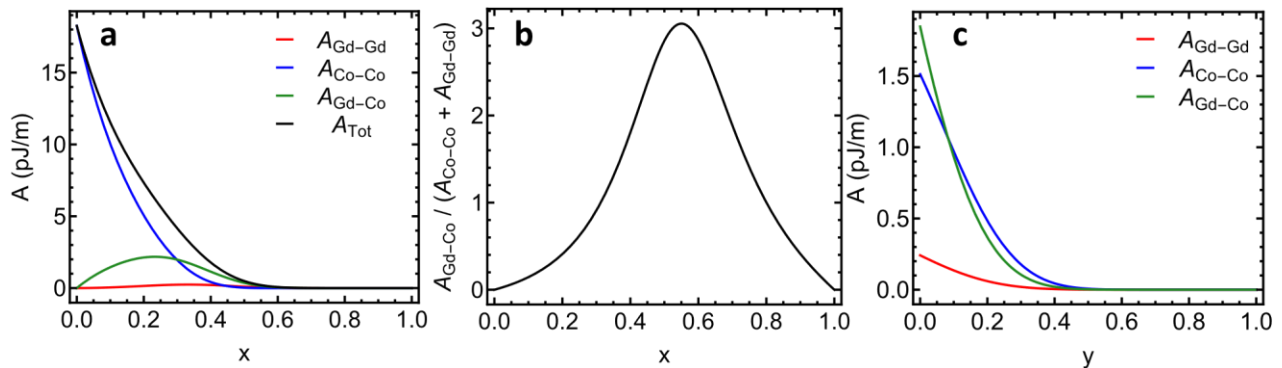

Figure 7.11: Exchange Stiffness as a function of (a) Gd atomic fraction and (c) Y atomic fraction, y, of $Gd_{0.32}Co_{0.68}$. (b) Ratio of AFM to FM exchange.

7.4.2 Exchange in thin films

The methodology used to calculate A above can be applied to the 3 nm GdCo thickness series by taking the RE dead layer into account. The RE dead has two relevant effects for the calculation of A: (1) it decreases the average RE atomic moment and spin across all compositions relative to thick films, and (2) it shifts the true alloyed composition to RE poor compared to the nominally deposited composition. The extent of RE atomic moment reduction is easily determined from the extracted RE dead layer in Chapter 6. However, the exchange energies, J_{ij}, used for calculation of A were determined using mean field analysis on thick GdCo films where the Gd dead layer is insignificant. As a result, assuming that the net J_{ij} only depends on the ratio of *alloyed* Gd and Co, the true alloyed Gd composition must be calculated for each 3 nm GdCo sample to assign its corresponding J_{ij}. This was done using the previously derived expression for $\tilde{x}$ in Eq. 6.8. The transformation is plotted in Fig. 7.12(a), showing the deviation between nominal composition and alloyed composition for all grown 3 nm GdCo samples. In general, this can be thought of as a composition scale factor to compare the magnetic properties of RE-TM films of various thicknesses. Once the appropriate $J_{ij}(x)$ is determined, the reduced $S_{Gd}(x)$ are calculated to yield A_{ij} (Fig. 7.12(b)). Note that the composition transformation effectively elongates the horizontal axis when compared to thick films, akin to the shifts observed in compensation composition in Chapter 6.
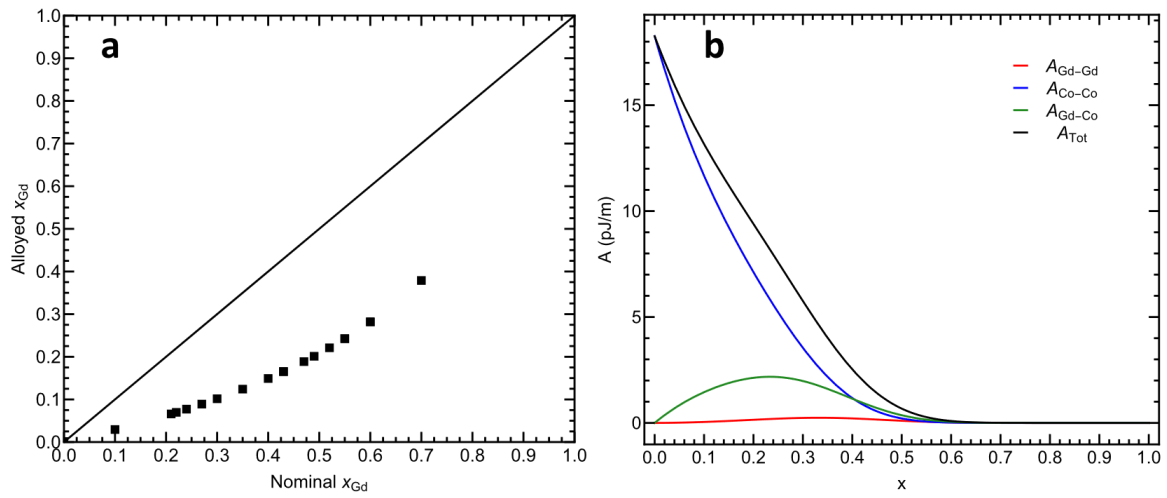
Figure 7.12: (a) Relation between nominal Gd composition and alloyed composition from Chapter 6, used to correct the 3 nm GdCo compositions. (b) Adjusted exchange stiffness as a function of nominal Gd concentration in 3 nm GdCo.

7.5 Extraction of DMI in 3 nm GdCo

After determining the exchange stiffness in 3 nm Gd_xCo_{1-x}, the domain wall width can be estimated using the relation,

$$\Delta = \sqrt{\frac{A}{K_{u,eff}}} \tag{7.15}$$

where A is the sum of the various exchange interactions in GdCo. The resulting domain wall widths are plotted in Fig. 7.13(a). The domain wall width shows a minimum in the middle of the PMA range near $x \approx 0.47$, stemming from the peak observed in K_u over the same range due to increased Gd-Co pair density. The exchange stiffness decreases by a factor of 7 over this range. The values of Δ are slightly lower than previously reported domain wall widths in 6 nm GdCo films, likely due to the increased $K_{u,eff}$ observed as a consequence of interfacial Pt/Co anisotropy discussed previously.

Figures 7.13(c) and (d) show the measured spin properties of the composition series. We find that the spin density is minimized and g_{eff} diverges around $x \approx 0.4$, confirming the location of angular momentum compensation suggested by the terminal velocity and damping data discussed earlier. S remains depressed on the Gd-dominated side of compensation, likely due to the highly reduced Co moment from low Co coordination. Away from angular momentum compensation, g_{eff} drops to $g_{eff} = 4.1 \pm 0.2$ on the Co-dominated side and $g_{eff} = 2.7 \pm 0.2$ on the Gd-dominated side. Pure Co and Gd have g factors of $g_{Co} \approx 2.2$ and $g_{Gd} = 2$, respectively, significantly lower than the g_{eff} observed at the edges of the measured composition range, indicating that the inclusion of Gd, even at $x = 0.27$, drastically alters the overall dynamic properties of GdCo.
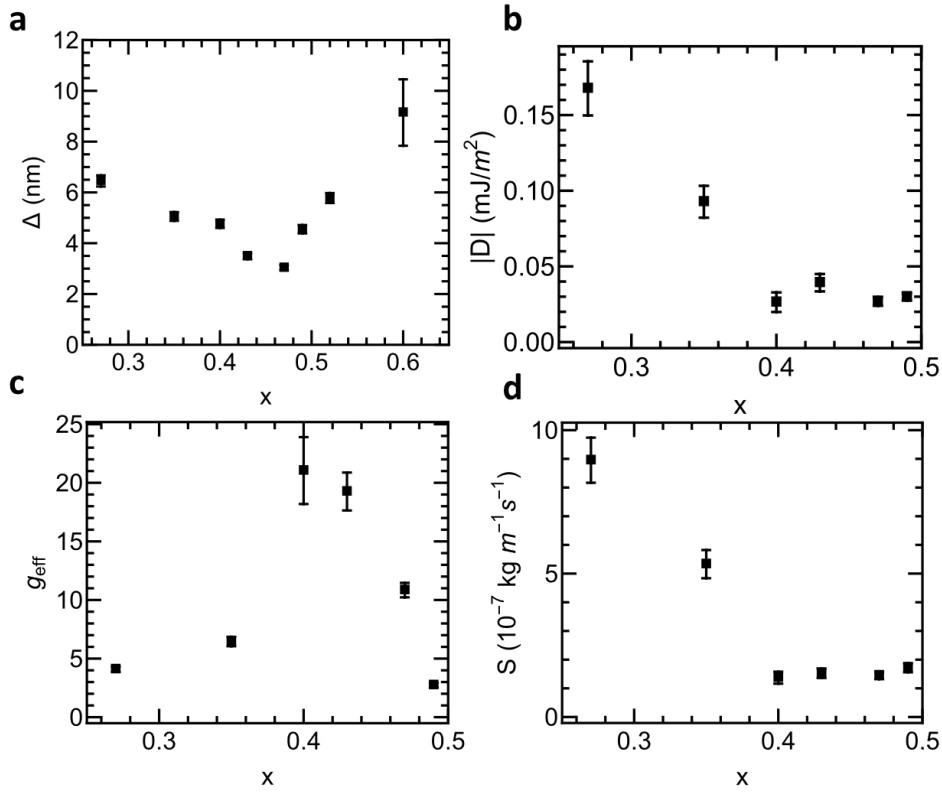
Figure 7.13: Dynamic magnetic properties of PMA 3 nm GdCo films showing (a) Domain wall width, calculated using Eq. 7.15, (b) DMI strength, (c) effective g factor, and (d) net spin density.

Finally, the DMI strength is shown in Fig. 7.13(b). After multiplying by M_s and Δ, a clear trend in D is evident. We observe a monotonic decrease with increasing Gd content across the entire PMA composition range, suggesting that the Pt/Co interaction is primarily responsible for the occurrence of DMI in GdCo films, and that the addition of Gd only dilutes the strength of the DMI. The value of D at $x = 0.44$ is smaller than the reported DMI in a 6 nm film at the same composition [6]. In heavy metal/ferromagnetic systems, $D \propto \frac{1}{t}$ when induced at an interface [40], making the reduced D value observed in 3 nm GdCo surprising. We note that measured SOT (Fig. 7.8(b)) is also lower than the reported SOT in 6 nm GdCo, which, combined with a reduced D, results in lower domain wall velocities than previously observed. Because DMI is sensitive to

interfacial quality [28,35,39,150], we ascribe both of these effects to increased surface roughness in thin GdCo films.

7.6 Conclusion

A number of RE-TM magnetic properties critical to spintronic devices and stabilization of chiral spin textures are found to strongly depend on RE concentration. The total effective anisotropy is found to strongly decrease with increased Gd concentration, consistent with a Pt/Co interfacial origin. The value $K_{u,eff}$ is also higher than in thicker GdCo films and in single crystal Co, further supporting an interfacial anisotropy origin. We also observe a sub-dominant increase in uniaxial anisotropy that is maximized at $x \approx 0.4$, consistent with a pair-ordering bulk anisotropy origin that is often used to explain bulk PMA in RE-TM alloys. The combination of domain wall velocity and depinning measurements under longitudinal and polar applied fields allows for determination of a variety of dynamic magnetic properties in Pt/GdCo heterostructures including DMI field, damping, spin density, SOT, and effective spin Hall angle. These fundamental measurements are combined with knowledge of the ferromagnetic and antiferromagnetic exchange interactions in GdCo to determine the magnitude of antisymmetric exchange constant D. D is found to monotonically decrease with increasing Gd content, suggesting that the Pt/Co interface is the primary source of DMI in Pt/GdCo films.

8 Summary and Outlook

8.1 Summary

In summary, we have thoroughly characterized the magnetic properties of Pt/RE-TM heterostructure through magneto-optical Kerr effect magnetometry (MOKE), x-ray magnetic circular dichroism (XMCD), and current-induced domain wall motion experiments. Our results have shown complex behavior in RE-TM alloys as a function of composition and film thickness, including changes in fundamental properties previously assumed to be independent of these factors. These insights should aid in the design of thin film amorphous ferrimagnets, paving the way for engineered RE-TM heterostructures with potential applications in racetrack memory, skyrmionics, and magnon devices.

Using Jones matrix analysis, we have developed a simple method for measurement of complex Kerr angles using conventional MOKE magnetometers to probe the normalized MOKE intensity as a function of waveplate and analyzer angle. The magnitude of the complex Kerr angle was found to decrease linearly in GdCo PMA films with increasing Gd concentration, consistent with a dominant Co Kerr angle contribution. This analysis was also combined with a study of noise contributions in wide-field MOKE microscopy to develop optical system design criteria to maximize SNR and, consequently, increase system sensitivity, enabling high-quality imaging of thin, low TM content films.

The average atomic moments of both TM and RE were found to decrease with increasing RE content at room temperature in GdCo and TbCo films. By contrast, near 0 K, the RE moment is independent of composition and, in the case of Gd, has an atomic moment close to its free ion expected value of 7 μ_B. The low temperature Tb moment is shown to have a moment far below its

elemental state, likely due to TbCo sperimagnetic ordering. We develop a model to describe the RE moment reduction at room temperature and TM moment reduction at all temperatures based on the average local exchange of a given atom. We additionally observe evidence of a RE dead layer that drastically alters the magnetization at low thicknesses in GdCo and TbCo films.

Finally, we probed the dynamic and spin transport properties of thin PMA GdCo films by measuring current-induced domain wall motion in microscale patterned magnetic racetracks. By observing the changes in domain wall velocity with current density under in-plane longitudinal fields, we determined the DMI strength monotonically decreases with increases Gd content, suggesting the presence of Gd interferes with the dominant interfacial Pt/Co interaction to reduce the DMI. We also observe reduced SOT and domain wall velocities compared to thicker films, potentially due to additional surface roughness at high Gd concentrations.

8.2 Outlook

In this final section, we discuss a couple of the potential developments in RE-TM research moving forward, including ferrimagnetic magnon dispersion and RKKY-coupled heterostructures for temperature-stable, compensated racetrack devices.

8.2.1 Brillouin Light Scattering for DMI Measurement

While the domain wall motion experiments discussed in Chapter 7 provide an effective method to determine several dynamic properties, they have inherent limitations. Due to the geometry of the wide-field MOKE microscope and layer structure, current-induced domain wall motion experiments only work on samples with PMA, meaning that only a limited subset of the grown 3 nm GdCo composition series was measurable using this scheme. Additionally, estimation

of the domain wall width is required for DMI extraction. Finally, domain wall motion experiments require lithographic patterning of samples, slowing throughput.

In contrast, Brillouin light scattering (BLS) can directly measure DMI by observing dispersion asymmetries in surface spin wave modes. It is a technique used to measure the difference in spin wave propagation in opposite directions caused by DMI. The application of an in-plane field causes spin waves to propagate in opposite directions at the top and bottom surfaces of the magnetic layer. The incident light reacts with the quantized spin waves, known as magnons, either gaining energy in magnon absorption (Anti-Stokes) or losing energy in the production of one (Stokes). These processes induce a frequency difference in the outgoing light that causes a frequency shift between Stokes and anti-Stokes peaks defined for ferromagnets as [41,151]:

$$\Delta f_{DMI} = \frac{2\gamma}{\pi M_s} Dk \tag{8.1}$$

allowing for the determination of DMI strength through analysis of BLS spin wave spectra as a function of wavevector, k. The observation of magnon peaks by BLS requires in-plane saturated samples, which makes samples with high PMA practically difficult to measure. In the case of the 3 nm GdCo composition series, fields > 20 kOe are required for the highest PMA samples.

Figure 8.1 shows the results of the BLS experiments on 3 nm GdCo. Figure 8.1(a) displays representative spectra for each composition measured. The relevant magnon peak is indicated by the red arrows in Fig. 8.1(a). Figure 8.1(b) shows the frequency difference between Stokes and anti-Stokes peaks in pure Pt/Co(3 nm) used to determine the DMI (Eq. 8.1). Starting at 27 at.% Gd, the magnon peaks qualitatively change, becoming much broader than at lower Gd compositions. In ferromagnets, the peak width is proportional to the Gilbert damping, α. From our domain wall motion experiments, we expect α_{eff}, and consequently the peak width, to diverge at

$x \approx 0.4$. Instead, we see the peak width continuously increase with Gd content, suggesting that the conventional ferromagnetic description may not be sufficient for $x > 0.22$.
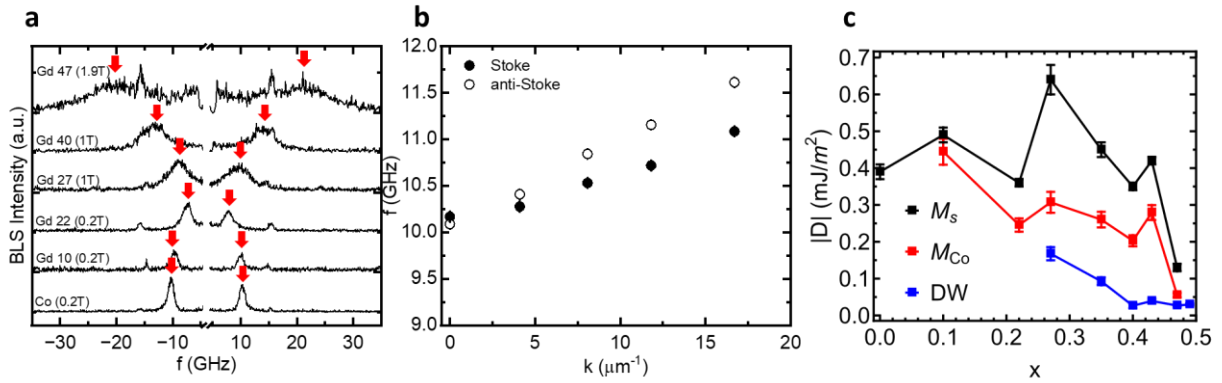

Figure 8.1: (a) BLS spectra of 3 nm GdCo showing broad magnon peaks for Gd concentrations >22 at.% Gd at $k = 0$. Arrows indicate location of magnon peaks. (b) Frequency versus wavevector of Pt/Co(3 nm). The difference in frequencies is used to compute D. (c) Extracted DMI assuming ferromagnetic dispersion relation. Black points use net M_s, red points use M_{Co}, and blue points are derived from domain wall motion experiments.

The extracted DMI values tell a similar story. The black data points in Fig. 8.1(c) use the ferromagnetic dispersion relation to determine D (Eq. 8.1). The extracted D undergoes a large jump at $x = 0.27$, analogous to the peak width. Broad magnon peaks are characteristic of antiferromagnets, suggesting that the RE-TM antiferromagnetic exchange interactions may begin dominating when $x > 0.22$. Ongoing theoretical work in our group has found that ferrimagnetic magnon dispersion is governed by the ratio of antiferromagnetic to ferromagnetic exchange rather than more traditional measures of degree of compensation such as net spin density. Our calculated exchange stiffness (Fig. 7.11) show that this ratio approaches 1 at $x = 0.27$, indicating significant

antiferromagnetic character in samples with $x \geq 0.27$. In these cases, the effect of an applied field on each sublattice must be considered to derive an accurate dispersion relation. Currently, work is ongoing in our group to fully develop accurate ferrimagnetic dispersion relations, however a first approximation to DMI extraction is given by the red points in Fig. 8.1(c). Here, only Co sublattice is assumed to contribute to the DMI and M_s in Eq. 8.1 is replaced with our previously calculated M_{Co}. This naïve correction removes the discontinuity in D at $x = 0.27$ but still significantly overestimates the DMI strength measured by domain wall motion (Fig. 8.1(c), blue points). Further analysis is required to correctly extract D at $x \geq 0.27$.

This method is also currently being used to investigate DMI in TbCo films. Because DMI requires mediation through a high SOC material (generally the heavy metal Pt in our systems), it is conceivable that a RE element with significant orbital angular momentum such as Tb would enhance the DMI, either by increasing its value with increasing RE concentration or by preventing its reduction with increasing thickness as s normally observed in ferromagnetic systems. Early measurements suggest remarkably different dispersion behavior in TbCo compared to GdCo, perhaps stemming from its sperimagnetic ordering.

8.2.2 RKKY-Coupled RE-TM Heterostructures

Pt/RE-TM heterostructures have been shown to exhibit domain wall velocities over 1 km/s near angular momentum compensation, making them a promising candidate for domain wall memory technologies [4–6,152]. However, RE-TM alloys are highly sensitive to changes in temperature (Fig. 8.2(b)), which limits the viability of them in commercial devices. One possible solution to this problem is to antiferromagnetically (AFM) couple two RE-TM layers to each other. If the two layers are on opposite sides of angular momentum compensation, then the gyrotropic

forces in each layer will cancel each other out and changes in temperature will increase the spin density of one layer while decreasing the spin density in the other layer. The extent of temperature stability would be controlled by the distance in angular momentum compensation temperature from room temperature in each layer (Fig. 8.2(b)).
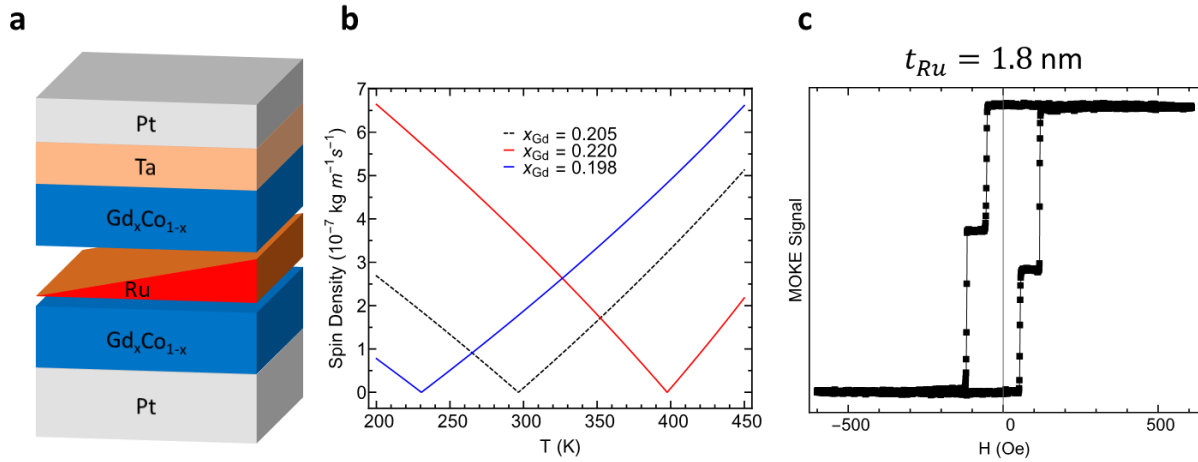
Figure 8.2: (a) RKKY-coupled GdCo stack. (b) Spin density in thick GdCo as a function of temperature at three compositions. (c) MOKE hysteresis loop of AFM RKKY-coupled GdCo.

The AFM coupling is achieved by insertion of a thin Ru interlayer between the RE-TM layers. The Ru couples the Co sublattice in each GdCo layer to each other FM or AFM through the RKKY interaction, depending on the Ru thickness. Figure 8.2(c) shows an AFM coupled Pt/GdCo/Ru/GdCo heterostructure, achieved with a Ru thickness of 1.8 nm. The main challenges in fabricating appropriate structures are achieving PMA in the top GdCo layer and optimizing the Ru thickness for maximum AFM coupling. Future work looks to test domain wall motion in said structures under a wide range of temperatures to ensure persistent high-speed domain wall motion.

9 References

[1]   R. H. Dee, *Magnetic Tape for Data Storage: An Enduring Technology*, Proceedings of the
       IEEE **96**, 1775 (2008).

[2]   K. Goda and M. Kitsuregawa, *The History of Storage Systems*, Proceedings of the IEEE
       100, 1433 (2012).

[3]   S. S. P. Parkin, M. Hayashi, and L. Thomas, *Magnetic Domain-Wall Racetrack Memory*,
       Science (1979) **320**, 190 (2008).

[4]   M. Binder et al., *Magnetization Dynamics of the Ferrimagnet CoGd near the
       Compensation of Magnetization and Angular Momentum*, Phys Rev B **74**, 134404 (2006).

[5]   K.-J. Kim et al., *Fast Domain Wall Motion in the Vicinity of the Angular Momentum
       Compensation Temperature of Ferrimagnets*, Nat Mater **16**, 1187 (2017).

[6]   L. Caretta et al., *Fast Current-Driven Domain Walls and Small Skyrmions in a
       Compensated Ferrimagnet*, Nat Nanotechnology **13**, 1154 (2018).

[7]   Z. R. Yan, Y. Z. Liu, Y. Guang, K. Yue, J. F. Feng, R. K. Lake, G. Q. Yu, and X. F. Han,
       Skyrmion-Based Programmable Logic Device with Complete Boolean Logic Functions,
       Phys Rev Appl **15**, 64004 (2021).

[8]   F. Büttner et al., *Dynamics and Inertia of Skyrmionic Spin Structures*, Nat Phys **11**, 225
       (2015).

[9]   A. Fert, N. Reyren, and V. Cros, *Magnetic Skyrmions: Advances in Physics and Potential
       Applications*, Nature Reviews Materials.

[10]   W. Jiang et al., *Blowing Magnetic Skyrmion Bubbles*, Science (1979) **349**, 283 (2015).

[11]   A. Fert, V. Cros, and J. Sampaio, *Skyrmions on the Track*, Nature Nanotechnology.

[12]   N. Romming, C. Hanneken, M. Menzel, J. E. Bickel, B. Wolter, K. Von Bergmann, A. Kubetzka, and R. Wiesendanger, *Writing and Deleting Single Magnetic Skyrmions*, Science (1979) **341**, 636 (2013).

[13]   I. Dzialoshinskii, *Thermodynamic Theory of "Weak" Ferromagnetism In Antiferromagnetic Substances*, Soviet Physics JETP **5**, 1259 (1957).

[14]   I. Dzyaloshinsky, *A Thermodynamic Theory of "Weak" Ferromagnetism of Antiferromagnetics*, Journal of Physics and Chemistry of Solids **4**, 241 (1958).

[15]   I. E. Dzyaloshinskii, *Theory of Helicoidal Structures in Antiferromagnets. I. Nonmetals*, JETP **19**, 960 (1964).

[16]   T. Moriya, *Anisotropic Superexchange Interaction and Weak Ferromagnetism*, Physical Review **120**, 91 (1960).

[17]   A. Crépieux and C. Lacroix, *Dzyaloshinsky-Moriya Interactions Induced by Symmetry Breaking at a Surface*, J Magn Magn Mater **182**, 341 (1998).

[18]   R. C. O'Handley, *Modern Magnetic Materials: Principles and Applications* (John Wiley and Sons, Inc., New York, NY, 2000).

[19]   F. Hellman et al., *Interface-Induced Phenomena in Magnetism*, Rev Mod Phys **89**, (2017).

[20]   J. M. D. Coey, *Magnetism and Magnetic Materials* (Cambridge University Press, Cambridge, UK, 2009).

[21]   S. Emori, D. C. Bono, and G. S. D. Beach, *Interfacial Current-Induced Torques in Pt/Co/GdOx*, Appl Phys Lett **101**, 042405 (2012).

[22]   S. W. Jung, W. Kim, T. D. Lee, K. J. Lee, and H. W. Lee, *Current-Induced Domain Wall Motion in a Nanowire with Perpendicular Magnetic Anisotropy*, Appl Phys Lett **92**, (2008).

[23] G. S. D. Beach, M. Tsoi, and J. L. Erskine, *Current-Induced Domain Wall Motion*, J Magn Magn Mater **320**, 1272 (2008).

[24] S. Emori, U. Bauer, S. M. Ahn, E. Martinez, and G. S. D. Beach, *Current-Driven Dynamics of Chiral Ferromagnetic Domain Walls*, Nat Mater **12**, 611 (2013).

[25] M. Bode, M. Heide, K. Von Bergmann, P. Ferriani, S. Heinze, G. Bihlmayer, A. Kubetzka, O. Pietzsch, S. Blügel, and R. Wiesendanger, *Chiral Magnetic Order at Surfaces Driven by Inversion Asymmetry*, Nature **447**, 190 (2007).

[26] D.-H. Kim et al., *Bulk Dzyaloshinskii–Moriya Interaction in Amorphous Ferrimagnetic Alloys*, Nat Mater **18**, 685 (2019).

[27] C. Moreau-Luchaire et al., *Additive Interfacial Chiral Interaction in Multilayers for Stabilization of Small Individual Skyrmions at Room Temperature*, Nat Nanotechnol **11**, 444 (2016).

[28] A. Soumyanarayanan, N. Reyren, A. Fert, and C. Panagopoulos, *Emergent Phenomena Induced by Spin–Orbit Coupling at Surfaces and Interfaces*, Nature **539**, 509 (2016).

[29] J. Sampaio, V. Cros, S. Rohart, A. Thiaville, and A. Fert, *Nucleation, Stability and Current-Induced Motion of Isolated Magnetic Skyrmions in Nanostructures*, Nat Nanotechnol **8**, 839 (2013).

[30] S. Heinze, K. Von Bergmann, M. Menzel, J. Brede, A. Kubetzka, R. Wiesendanger, G. Bihlmayer, and S. Blügel, *Spontaneous Atomic-Scale Magnetic Skyrmion Lattice in Two Dimensions*, Nat Phys **7**, 713 (2011).

[31] F. Büttner et al., *Field-Free Deterministic Ultrafast Creation of Magnetic Skyrmions by Spin-Orbit Torques*, Nat Nanotechnol **12**, 1040 (2017).

[32] K. S. Ryu, L. Thomas, S. H. Yang, and S. Parkin, *Chiral Spin Torque at Magnetic Domain Walls*, Nat Nanotechnol **8**, 527 (2013).

[33] E. Martinez, S. Emori, N. Perez, L. Torres, and G. S. D. Beach, *Current-Driven Dynamics of Dzyaloshinskii Domain Walls in the Presence of in-Plane Fields: Full Micromagnetic and One-Dimensional Analysis*, J Appl Phys **115**, (2014).

[34] H. Yang, A. Thiaville, S. Rohart, A. Fert, and M. Chshiev, *Anatomy of Dzyaloshinskii-Moriya Interaction at Co/Pt Interfaces*, Phys Rev Lett **115**, (2015).

[35] S. Tacchi, R. E. Troncoso, M. Ahlberg, G. Gubbiotti, M. Madami, J. Åkerman, and P. Landeros, *Interfacial Dzyaloshinskii-Moriya Interaction in <math Display="inline"> <mrow> <mi>Pt</Mi> <mo>/</Mo> <mi>CoFeB</Mi> </Mrow> </Math> Films: Effect of the Heavy-Metal Thickness*, Phys Rev Lett **118**, 147201 (2017).

[36] G. Chen, T. Ma, A. T. N'Diaye, H. Kwon, C. Won, Y. Wu, and A. K. Schmid, *Tailoring the Chirality of Magnetic Domain Walls by Interface Engineering*, Nat Commun **4**, (2013).

[37] L. Liu, C. F. Pai, Y. Li, H. W. Tseng, D. C. Ralph, and R. A. Buhrman, *Spin-Torque Switching with the Giant Spin Hall Effect of Tantalum*, Science (1979) **336**, 555 (2012).

[38] R. Streubel, C. Lambert, N. Kent, P. Ercius, A. T. N'Diaye, C. Ophus, S. Salahuddin, and P. Fischer, *Experimental Evidence of Chiral Ferrimagnetism in Amorphous GdCo Films*, Advanced Materials **30**, 1800199 (2018).

[39] A. Hrabec, N. A. Porter, A. Wells, M. J. Benitez, G. Burnell, S. McVitie, D. McGrouther, T. A. Moore, and C. H. Marrows, *Measuring and Tailoring the Dzyaloshinskii-Moriya Interaction in Perpendicularly Magnetized Thin Films*, Phys Rev B **90**, 020402 (2014).

[40] J. Cho et al., *Thickness Dependence of the Interfacial Dzyaloshinskii–Moriya Interaction in Inversion Symmetry Broken Systems*, Nat Commun **6**, 7635 (2015).

[41]   H. T. Nembach, J. M. Shaw, M. Weiler, E. Jué, and T. J. Silva, *Linear Relation between Heisenberg Exchange and Interfacial Dzyaloshinskii-Moriya Interaction in Metal Films*, Nat Phys **11**, 825 (2015).

[42]   K. S. Ryu, S. H. Yang, L. Thomas, and S. S. P. Parkin, *Chiral Spin Torque Arising from Proximity-Induced Magnetization*, Nat Commun **5**, (2014).

[43]   T. Tono, T. Taniguchi, K. J. Kim, T. Moriyama, A. Tsukamoto, and T. Ono, *Chiral Magnetic Domain Wall in Ferrimagnetic GdFeCo Wires*, Applied Physics Express **8**, 73001 (2015).

[44]   K. Cai, Z. Zhu, J. Min Lee, R. Mishra, L. Ren, S. D. Pollard, P. He, G. Liang, K. Leong Teo, and H. Yang, *Ultrafast and Energy-Efficient Spin-Orbit Torque Switching in Compensated Ferrimagnets*, Nat Electron (2020).

[45]   P. Hansen and H. Heitmann, *Media for Erasable Magnetooptic Recording*, IEEE Trans Magn **25**, 4390 (1989).

[46]   J. M. D. Coey, *Amorphous Magnetic Order*, J Appl Phys **49**, 1646 (1978).

[47]   J. Zhou and G. A. Fiete, *Rare Earths in a Nutshell*, Phys Today **73**, 66 (2020).

[48]   R. Harris, M. Plischke, and M. J. Zuckermann, *New Model for Amorphous Magnetism*, Phys Rev Lett **31**, 160 (1973).

[49]   R. W. Cochrane, R. Harris, and M. Plischke, *Role of Structure in Amorphous Magnetic Materials: Dense Random Packing of Hard Spheres of Two Sizes*, J Non Cryst Solids **15**, 239 (1974).

[50]   K. J. Kim et al., *Fast Domain Wall Motion in the Vicinity of the Angular Momentum Compensation Temperature of Ferrimagnets*, Nat Mater **16**, (2017).

[51] J. E. Greene, *Review Article: Tracing the Recorded History of Thin-Film Sputter Deposition: From the 1800s to 2017*, Journal of Vacuum Science & Technology A: Vacuum, Surfaces, and Films **35**, 05C204 (2017).

[52] A. H. Simon, *Sputter Processing*, in *Handbook of Thin Film Deposition* (Elsevier, 2012), pp. 55–88.

[53] A. Behera, S. Aich, and T. Theivasanthi, *Magnetron Sputtering for Development of Nanostructured Materials*, in *Design, Fabrication, and Characterization of Multifunctional Nanomaterials* (Elsevier, 2022), pp. 177–199.

[54] R. Messier, A. P. Giri, and R. A. Roy, *Revised Structure Zone Model for Thin Film Physical Structure*, Journal of Vacuum Science & Technology A: Vacuum, Surfaces, and Films **2**, 500 (1984).

[55] J. A. Thornton, *Influence of Apparatus Geometry and Deposition Conditions on the Structure and Topography of Thick Sputtered Coatings*, Journal of Vacuum Science and Technology **11**, 666 (1974).

[56] J. A. Thornton, *Influence of Substrate Temperature and Deposition Rate on Structure of Thick Sputtered Cu Coatings*, Journal of Vacuum Science and Technology **12**, 830 (1975).

[57] J. A. Thornton, *The Microstructure of Sputter-deposited Coatings*, Journal of Vacuum Science & Technology A: Vacuum, Surfaces, and Films **4**, 3059 (1986).

[58] B. Dodrill and J. R. Lindemuth, *Vibrating Sample Magnetometry*, in *Magnetic Measurement Techniques for Materials Characterization* (Springer International Publishing, Cham, 2021), pp. 15–37.

[59] S. Yamamoto and I. Matsuda, *Measurement of the Resonant Magneto-Optical Kerr Effect Using a Free Electron Laser*, Applied Sciences **7**, 662 (2017).

[60] J. L. Erskine and E. A. Stern, *Magneto-Optic Kerr Effects in Gadolinium*, Phys Rev B **8**, 1239 (1973).

[61] G. A. N. Connell, *Magneto-Optics and Amorphous Metals: An Optical Storage Revolution*, J Magn Magn Mater **54–57**, 1561 (1986).

[62] D. A. Allwood, G. Xiong, M. D. Cooke, and R. P. Cowburn, *Magneto-Optical Kerr Effect Analysis of Magnetic Nanostructures*, J Phys D Appl Phys **36**, 2175 (2003).

[63] S. J. J. Lee, K. J. J. Kim, P. C. C. Canfield, and D. W. W. Lynch, *Investigation of Optical and Magneto-Optical Constants and Their Surface-Oxide-Layer Effects of Single-Crystalline GdCo2*, J Magn Magn Mater **213**, 312 (2000).

[64] S. Bhatti, R. Sbiaa, A. Hirohata, H. Ohno, S. Fukami, and S. N. Piramanayagam, *Spintronics Based Random Access Memory: A Review*, Materials Today.

[65] T. Gushi et al., *Large Current Driven Domain Wall Mobility and Gate Tuning of Coercivity in Ferrimagnetic Mn4N Thin Films*, Nano Lett **19**, 8716 (2019).

[66] M. Huang et al., *Voltage Control of Ferrimagnetic Order and Voltage-Assisted Writing of Ferrimagnetic Spin Textures*, Nat Nanotechnol **16**, 981 (2021).

[67] A. E. Kossak, M. Huang, P. Reddy, D. Wolf, and G. S. D. Beach, *Voltage Control of Magnetic Order in RKKY Coupled Multilayers*, Sci Adv **9**, (2023).

[68] S. A. Siddiqui, J. Han, J. T. Finley, C. A. Ross, and L. Liu, *Current-Induced Domain Wall Motion in a Compensated Ferrimagnet*, Phys Rev Lett **121**, 057701 (2018).

[69] S. Ghosh et al., *Current-Driven Domain Wall Dynamics in Ferrimagnetic Nickel-Doped Mn4N Films: Very Large Domain Wall Velocities and Reversal of Motion Direction across the Magnetic Compensation Point*, Nano Lett **21**, 2580 (2021).

[70] M. Buchmeier, H. Dassow, D. E. Bürgler, and C. M. Schneider, *Intensity of Brillouin Light Scattering from Spin Waves in Magnetic Multilayers with Noncollinear Spin Configurations: Theory and Experiment*, Phys Rev B **75**, 184436 (2007).

[71] J. Hamrle, J. Pištora, B. Hillebrands, B. Lenk, and M. Münzenberg, *Analytical Expression of the Magneto-Optical Kerr Effect and Brillouin Light Scattering Intensity Arising from Dynamic Magnetization*, J Phys D Appl Phys **43**, 325004 (2010).

[72] K. Sato, H. Hongu, H. Ikekame, Y. Tosaka, M. Watanabe, K. Takanashi, and H. Fujimori, *Magnetooptical Kerr Spectrometer for 1.2-5.9 EV Region and Its Application to FePt/Pt Multilayers*, Jpn J Appl Phys **32**, 989 (1993).

[73] S. M. Saini, N. Singh, T. Nautiyal, and S. Auluck, *Comparative Study of Optical and Magneto-Optical Properties of GdFe 2 and GdCo 2*, Journal of Physics: Condensed Matter **19**, 176203 (2007).

[74] S. Chao, L. Yeh, T. Lo, and T. Jeng, *Ellipsometric Measurement of Magneto-optical Kerr Rotation at Normal Incidence*, J Appl Phys **67**, 4241 (1990).

[75] P. Q. J. Nederpel and J. W. D. Martens, *Magneto-optical Ellipsometer*, Review of Scientific Instruments **56**, 687 (1985).

[76] E. Collet, *Field Guide to Polarization* (SPIE - The International Society for Optical Engineering, Bellingham, WA, 2005).

[77] E. Hecht, *Optics*, 2nd ed. (Addison-Wesley Publishing Company, Inc., 1987).

[78] M. Mansuripur, G. A. N. Connell, and J. W. Goodman, *Signal and Noise in Magneto-Optical Readout*, J Appl Phys **53**, 4485 (1982).

[79] S. Watanabe, T. Takahashi, and K. Bennett, *Quantitative Evaluation of the Accuracy and Variance of Individual Pixels in a Scientific CMOS (SCMOS) Camera for Computational*

Imaging, Single Molecule Spectroscopy and Superresolution Imaging X **10071**, 100710Z (2017).

[80]   P. C. Logofaˇtu, *Simple Method for Determining the Fast Axis of a Wave Plate*, Optical Engineering **41**, 3316 (2002).

[81]   C. Kim et al., *Distinct Handedness of Spin Wave across the Compensation Temperatures of Ferrimagnets*, Nat Mater **19**, 980 (2020).

[82]   S. Honda and M. Yoshiyama, *Kerr Rotation Angle versus Cobalt Sublattice Magnetic Moment in RE-Co Sputtered Films*, Jpn J Appl Phys **27**, 2073 (1988).

[83]   Y. J. Choe, S. Tsunashima, T. Katayama, and S. Uchiyama, *Magneto-Optic Kerr Spectra of Amorphous RE-Co Thin Films*, Journal of the Magnetics Society of Japan **11**, S1_273 (1987).

[84]   Z. Q. Qiu and S. D. Bader, *Surface Magneto-Optic Kerr Effect (SMOKE)*, J Magn Magn Mater **200**, 664 (1999).

[85]   W. H. Li, Z. Jin, D. L. Wen, X. M. Zhang, M. H. Qin, and J.-M. Liu, *Ultrafast Domain Wall Motion in Ferrimagnets Induced by Magnetic Anisotropy Gradient*, Phys Rev B **101**, 024414 (2020).

[86]   I. Lemesh et al., *Current-Induced Skyrmion Generation through Morphological Thermal Transitions in Chiral Ferromagnetic Heterostructures*, Advanced Materials **30**, 1805461 (2018).

[87]   S. Mangin et al., *Engineered Materials for All-Optical Helicity-Dependent Magnetic Switching*, Nat Mater **13**, 286 (2014).

[88]   B. Hebler, A. Hassdenteufel, P. Reinhardt, H. Karl, and M. Albrecht, *Ferrimagnetic Tb–Fe Alloy Thin Films: Composition and Thickness Dependence of Magnetic Properties and All-Optical Switching*, Front Mater **3**, 8 (2016).

[89]   Z. Zheng et al., *Field-Free Spin-Orbit Torque-Induced Switching of Perpendicular Magnetization in a Ferrimagnetic Layer with a Vertical Composition Gradient*, Nat Commun **12**, 4555 (2021).

[90]   K. Cai, Z. Zhu, J. M. Lee, R. Mishra, L. Ren, S. D. Pollard, P. He, G. Liang, K. L. Teo, and H. Yang, *Ultrafast and Energy-Efficient Spin–Orbit Torque Switching in Compensated Ferrimagnets*, Nat Electron **3**, 37 (2020).

[91]   R. K. Wangsness, *Sublattice Effects in Magnetic Resonance*, Physical Review **91**, 1085 (1953).

[92]   Y. Hirata et al., *Correlation between Compensation Temperatures of Magnetization and Angular Momentum in GdFeCo Ferrimagnets*, Phys Rev B **97**, 220403(R) (2018).

[93]   P. Hansen, C. Clausen, G. Much, M. Rosenkranz, and K. Witter, *Magnetic and Magneto-optical Properties of Rare-earth Transition-metal Alloys Containing Gd, Tb, Fe, Co*, J Appl Phys **66**, 756 (1989).

[94]   M. Suzuki, H. Muraoka, Y. Inaba, H. Miyagawa, N. Kawamura, T. Shimatsu, H. Maruyama, N. Ishimatsu, Y. Isohama, and Y. Sonobe, *Depth Profile of Spin and Orbital Magnetic Moments in a Subnanometer Pt Film on Co*, Phys Rev B **72**, 054430 (2005).

[95]   M.-S. Lin, H.-C. Hou, Y.-C. Wu, P.-H. Huang, C.-H. Lai, H.-H. Lin, H.-J. Lin, and F.-H. Chang, *Effects of Perpendicular Interlayer Coupling Strength on Canting Angles of TbCo-Sublattice Magnetization*, Phys Rev B **79**, 140412(R) (2009).

[96] T. Ueno, N. Inami, R. Sagayama, Z. Wen, M. Hayashi, S. Mitani, R. Kumai, and K. Ono, *Relation between Electronic Structure and Magnetic Anisotropy in Amorphous TbCo Films Probed by X-Ray Magnetic Circular Dichroism*, J Phys D Appl Phys **49**, 205001 (2016).

[97] N. Bergeard, A. Mougin, M. Izquierdo, E. Fonda, and F. Sirotti, *Correlation between Structure, Electronic Properties, and Magnetism in CoxGd1-x Thin Amorphous Films*, Phys Rev B **96**, 064418 (2017).

[98] R. Cid, J. M. Alameda, S. M. Valvidares, J. C. Cezar, P. Bencok, N. B. Brookes, and J. Díaz, *Perpendicular Magnetic Anisotropy in Amorphous NdxCo1-x Thin Films Studied by x-Ray Magnetic Circular Dichroism*, Phys Rev B **95**, 224402 (2017).

[99] T. A. Ostler et al., *Crystallographically Amorphous Ferrimagnetic Alloys: Comparing a Localized Atomistic Spin Model with Experiments*, Phys Rev B **84**, 024407 (2011).

[100] I. Radu et al., *Transient Ferromagnetic-like State Mediating Ultrafast Reversal of Antiferromagnetically Coupled Spins*, Nature **472**, 205 (2011).

[101] H. B. Vasili et al., *Direct Observation of Multivalent States and $4f \rightarrow 3d$ Charge Transfer in Ce-Doped Yttrium Iron Garnet Thin Films*, Phys Rev B **96**, 014433 (2017).

[102] A. Singha, R. Baltic, F. Donati, C. Wäckerlin, J. Dreiser, L. Persichetti, S. Stepanow, P. Gambardella, S. Rusponi, and H. Brune, *4f Occupancy and Magnetism of Rare-Earth Atoms Adsorbed on Metal Substrates*, Phys Rev B **96**, 224418 (2017).

[103] Y. Teramura, A. Tanaka, B. T. Thole, and T. Jo, *Effect of Coulomb Interaction on the X-Ray Magnetic Circular Dichroism Spin Sum Rule in Rare Earths*, J Physical Soc Japan **65**, 3056 (1996).

[104] C. T. Chen, Y. U. Idzerda, H.-J. Lin, N. V Smith, G. Meigs, E. Chaban, G. H. Ho, E. Pellegrin, and F. Sette, *Experimental Confirmation of the X-Ray Magnetic Circular Dichroism Sum Rules for Iron and Cobalt*, Phys Rev Lett **75**, 152 (1995).

[105] K. H. J. Buschow, M. Brouha, J. W. M. Biesterbos, and A. G. Dirks, *Crystalline and Amorphous Rare-Earth Transition Metal Alloys*, Physica B+C **91**, 261 (1977).

[106] N. Sato, K. P. O'Brien, K. Millard, B. Doyle, and K. Oguz, *Investigation of Extrinsic Damping Caused by Magnetic Dead Layer in Ta-CoFeB-MgO Multilayers with Perpendicular Anisotropy*, J Appl Phys **119**, 093902 (2016).

[107] V. Jaccarino and L. R. Walker, *Discontinuous Occurrence of Localized Moments in Metals*, Phys Rev Lett **15**, 258 (1965).

[108] C. T. Ma, Y. Xie, H. Sheng, A. W. Ghosh, and S. J. Poon, *Robust Formation of Ultrasmall Room-Temperature Neél Skyrmions in Amorphous Ferrimagnets from Atomistic Simulations*, Sci Rep **9**, 9964 (2019).

[109] A. V. Svalov, O. A. Adanakova, V. O. Vas'kovskiy, K. G. Balymov, A. Larrañaga, G. V. Kurlyandskaya, R. Domingues Della Pace, and C. C. Plá Cid, *Thickness Dependence of Magnetic Properties of Thin Amorphous Ferrimagnetic Rare Earth–Transition Metal Multilayers*, J Magn Magn Mater **459**, 57 (2018).

[110] M. J. Besnus, A. Herr, and G. Fischer, *On the Magnetic Properties of Gd(Fe 1-x Al x) 2 Compounds*, Journal of Physics F: Metal Physics **9**, 745 (1979).

[111] W. C. Koehler, *Magnetic Properties of Rare-Earth Metals and Alloys*, J Appl Phys **36**, 1078 (1965).

[112] H. W. White, B. J. Beaudry, P. Burgardt, S. Legvold, and B. N. Harmon, *Magnetic Moments of Ferromagnetic Gadolinium Alloys*, in *AIP Conference Proceedings*, Vol. 29 (AIP, 1976), pp. 329–330.

[113] D. E. Hegland, S. Legvold, and F. H. Spedding, *Magnetization and Electrical Resistivity of Terbium Single Crystals*, Physical Review **131**, 158 (1963).

[114] A. V. Svalov, I. A. Makarochkin, E. V. Kudyukov, E. A. Stepanova, V. O. Vas'kovskii, A. Larrañaga, and G. V. Kurlyandskaya, *Changes in the Magnetic Structure upon Varying the Magnetic Layer Thickness in [Tb–Co/Si]n Films*, Physics of Metals and Metallography **122**, 115 (2021).

[115] V. O. Vas'kovskiy, O. A. Adanakova, K. G. Balymov, N. A. Kulesh, A. V. Svalov, and E. A. Stepanova, *Specific Features of the Formation of Atomic Magnetic Moments in Amorphous Films RE-Co (RE = La, Gd, Tb)*, Physics of the Solid State **57**, 1142 (2015).

[116] B. I. Min and Y. R. Jang, *The Effect of the Spin-Orbit Interaction on the Electronic Structure of Magnetic Materials*, Journal of Physics: Condensed Matter **3**, 5131 (1991).

[117] S. Chikazumi, *Physics of Ferromagnetism*, 2nd ed. (Oxford University Press, Oxford, 1997).

[118] G. Sala et al., *Asynchronous Current-Induced Switching of Rare-Earth and Transition-Metal Sublattices in Ferrimagnetic Alloys*, Nat Mater **21**, 640 (2022).

[119] R. Tran, Z. Xu, B. Radhakrishnan, D. Winston, W. Sun, K. A. Persson, and S. P. Ong, *Surface Energies of Elemental Crystals*, Sci Data **3**, 160080 (2016).

[120] J. Sticht and J. Kübler, *Electronic Structure of Ferromagnetic Gd*, Solid State Commun **53**, 529 (1985).

[121] Y. Ogata, H. Chudo, M. Ono, K. Harii, M. Matsuo, S. Maekawa, and E. Saitoh, *Gyroscopic g Factor of Rare Earth Metals*, Appl Phys Lett **110**, 072409 (2017).

[122] D. H. Suzuki, M. Valvidares, P. Gargiani, M. Huang, A. E. Kossak, and G. S. D. Beach, *Thickness and Composition Effects on Atomic Moments and Magnetic Compensation Point in Rare-Earth Transition-Metal Thin Films*, Phys Rev B **107**, 134430 (2023).

[123] C. Tannous and J. Gieraltowski, *The Stoner–Wohlfarth Model of Ferromagnetism*, Eur J Phys **29**, 475 (2008).

[124] D. M. Paige, B. Szpunar, and B. K. Tanner, *The Magnetocrystalline Anisotropy of Cobalt*, J Magn Magn Mater **44**, 239 (1984).

[125] P. F. Carcia, *Perpendicular Magnetic Anisotropy in Pd/Co and Pt/Co Thin-film Layered Structures*, J Appl Phys **63**, 5066 (1988).

[126] I. Benguettat-El Mokhtari et al., *Perpendicular Magnetic Anisotropy and Interfacial Dzyaloshinskii–Moriya Interaction in as Grown and Annealed X /Co/ Y Ultrathin Systems*, Journal of Physics: Condensed Matter **32**, 495802 (2020).

[127] S. Joo, R. S. Alemayehu, J.-G. G. Choi, B.-G. G. Park, and G.-M. M. Choi, *Magnetic Anisotropy and Damping Constant of Ferrimagnetic GdCo Alloy near Compensation Point*, Materials **14**, 2604 (2021).

[128] K. Ueda, A. J. Tan, and G. S. D. Beach, *Effect of Annealing on Magnetic Properties in Ferrimagnetic GdCo Alloy Films with Bulk Perpendicular Magnetic Anisotropy*, AIP Adv **8**, 125204 (2018).

[129] T. Kusuda, S. Honda, and M. Ohkoshi, *Perpendicular Anisotropy of Bias-Sputtered GdCo Film*, J Appl Phys **53**, 2338 (1982).

[130] V. G. Harris, W. T. Elam, N. C. Koon, and F. Hellman, *Deposition-Temperature Dependence of Structural Anisotropy in Amorphous Tb-Fe Films*, Phys Rev B **49**, 3637 (1994).

[131] R. C. Taylor and A. Gangulee, *Magnetization and Magnetic Anisotropy in Evaporated GdCo Amorphous Films*, J Appl Phys **47**, 4666 (1976).

[132] K. Ueda, M. Mann, C.-F. Pai, A.-J. Tan, and G. S. D. Beach, *Spin-Orbit Torques in Ta/Tb x Co 100-x Ferrimagnetic Alloy Films with Bulk Perpendicular Magnetic Anisotropy*, Appl Phys Lett **109**, 232403 (2016).

[133] J. C. S. Lévy and D. Mercier, *Amorphous Structures: A Local Analysis*, J Appl Phys **53**, 7709 (1982).

[134] A. L. Tedstone, C. E. Patrick, S. Kumar, R. S. Edwards, M. R. Lees, G. Balakrishnan, and J. B. Staunton, *Structural and Magnetic Properties of <math> <mrow> <msub> <mi>GdCo</Mi> <mrow> <mn>5</Mn> <mo>−</Mo> <mi>x</Mi> </Mrow> </Msub> <msub> <mi>Ni</Mi> <mi>x</Mi> </Msub> </Mrow> </Math>*, Phys Rev Mater **3**, 034409 (2019).

[135] A. L. Dantas, G. O. G. Rebouças, A. S. W. T. Silva, and A. S. Carriço, *Interface Roughness Effects on Coercivity and Exchange Bias*, J Appl Phys **97**, 10K105 (2005).

[136] M. Li, Y.-P. Zhao, G.-C. Wang, and H.-G. Min, *Effect of Surface Roughness on Magnetization Reversal of Co Films on Plasma-Etched Si(100) Substrates*, J Appl Phys **83**, 6287 (1998).

[137] I. M. Miron, K. Garello, G. Gaudin, P. J. Zermatten, M. V. Costache, S. Auffret, S. Bandiera, B. Rodmacq, A. Schuhl, and P. Gambardella, *Perpendicular Switching of a Single Ferromagnetic Layer Induced by In-Plane Current Injection*, Nature 2011 476:7359 **476**, 189 (2011).

[138] L. Liu, C.-F. Pai, Y. Li, H. W. Tseng, D. C. Ralph, and R. A. Buhrman, *Spin-Torque Switching with the Giant Spin Hall Effect of Tantalum*, Science (1979) **336**, 555 (2012).

[139] X. Xie et al., *Controllable Field-Free Switching of Perpendicular Magnetization through Bulk Spin-Orbit Torque in Symmetry-Broken Ferromagnetic Films*, Nat Commun **12**, 2473 (2021).

[140] A. Thiaville, S. Rohart, É. Jué, V. Cros, and A. Fert, *Dynamics of Dzyaloshinskii Domain Walls in Ultrathin Magnetic Films*, EPL (Europhysics Letters) **100**, 57002 (2012).

[141] W. Seung Ham, S. Kim, D.-H. Kim, K.-J. Kim, T. Okuno, H. Yoshikawa, A. Tsukamoto, T. Moriyama, and T. Ono, *Temperature Dependence of Spin-Orbit Effective Fields in Pt/GdFeCo Bilayers*, Appl Phys Lett **110**, 242405 (2017).

[142] C.-F. Pai, M. Mann, A. J. Tan, and G. S. D. Beach, *Determination of Spin Torque Efficiencies in Heterostructures with Perpendicular Magnetic Anisotropy*, Phys Rev B **93**, 144409 (2016).

[143] K. Ueda, M. Mann, P. W. P. P. de Brouwer, D. Bono, and G. S. D. D. Beach, *Temperature Dependence of Spin-Orbit Torques across the Magnetic Compensation Point in a Ferrimagnetic TbCo Alloy Film*, Phys Rev B **96**, 64410 (2017).

[144] S.-G. Je et al., *Spin-Orbit Torque-Induced Switching in Ferrimagnetic Alloys: Experiments and Modeling*, Appl Phys Lett **112**, 062401 (2018).

[145] N. Reynolds, P. Jadaun, J. T. Heron, C. L. Jermain, J. Gibbons, R. Collette, R. A. Buhrman, D. G. Schlom, and D. C. Ralph, *Spin Hall Torques Generated by Rare-Earth Thin Films*, Phys Rev B **95**, 064412 (2017).

[146] A. Y. Dobin and R. H. Victora, *Surface Roughness Induced Extrinsic Damping in Thin Magnetic Films*, Phys Rev Lett **92**, 257204 (2004).

[147] A. Gangulee and R. J. Kobliska, *Mean Field Analysis of the Magnetic Properties of Amorphous Transition-metal–Rare-earth Alloys*, J Appl Phys **49**, 4896 (1978).

[148] A. Gangulee and R. J. Kobliska, *Magnetic Properties of Amorphous Co-Gd-Mo-Ar Thin Films*, J Appl Phys **49**, 4169 (1978).

[149] T. Kato, K. Nakazawa, R. Komiya, N. Nishizawa, S. Tsunashima, and S. Iwata, *Compositional Dependence of G-Factor and Damping Constant of GdFeCo Amorphous Alloy Films*, in *IEEE Transactions on Magnetics*, Vol. 44 (2008), pp. 3380–3383.

[150] H. Yang, A. Thiaville, S. Rohart, A. Fert, and M. Chshiev, *Anatomy of Dzyaloshinskii-Moriya Interaction at Co/Pt Interfaces*, Phys Rev Lett **115**, 267210 (2015).

[151] K. Di, V. L. Zhang, H. S. Lim, S. C. Ng, M. H. Kuok, J. Yu, J. Yoon, X. Qiu, and H. Yang, *Direct Observation of the Dzyaloshinskii-Moriya Interaction in a Pt/Co/Ni Film*, Phys Rev Lett **114**, (2015).

[152] C. D. Stanciu, A. V. Kimel, F. Hansteen, A. Tsukamoto, A. Itoh, A. Kirilyuk, and Th. Rasing, *Ultrafast Spin Dynamics across Compensation Points in Ferrimagnetic $GdFeCo$: The Role of Angular Momentum Compensation*, Phys Rev B **73**, 220402 (2006).